

Structural Optimization Of A Vertical Axis Wind Turbine With Aeroelastic Analysis

B. Roscher

29th June 2014



Structural Optimization Of A Vertical Axis Wind Turbine With Aeroelastic Analysis

MASTER OF SCIENCE THESIS

For obtaining the degree of Master of Science in Engineering Wind
Energy at Technical University of Denmark and in Aerospace
Engineering at Delft University of Technology.

B. Roscher

29th June 2014

European Wind Energy Master - EWEM
DUWIND - Delft University of Technology
Technical University of Denmark, Department of Wind Energy
Sandia National Laboratories
Fraunhofer Institute - IWES



Copyright © B. Roscher
All rights reserved.

EUROPEAN WIND ENERGY MASTER - EWEM
OF
ROTOR DESIGN TRACK

The undersigned hereby certify that they have read and recommend to the European Wind Energy Master - EWEM for acceptance of the thesis entitled “**Structural Optimization Of A Vertical Axis Wind Turbine With Aeroelastic Analysis**” by **B. Roscher** in partial fulfillment of the requirements for the degree of **Master of Science**.

Dated: 29th June 2014

Supervisor:

Ferreira, Carlos Simão of Delft University of Technology

Supervisor:

Madsen, Helge Aagard of Denmark Technical University

Reader:

Griffith, Daniel Todd of Sandia National Laboratories

Reader:

Stoevesandt, Bernhard of Fraunhofer Institute - IWES

Abstract

Currently, the price per kW of offshore wind energy is 55% larger than onshore [38, 52]. Of this price, the rotor corresponds to 22%. To reduce the price of wind energy, it is necessary to investigate wind turbine concepts with scales above 10 MW. The commonly known Horizontal Axis Wind Turbine (HAWT) requires offshore a large support structure. If the turbine is designed to be floating, a deep floater is needed to limit the tilt angle. A possible concept to meet this challenges is the lift-driven Vertical Axis Wind Turbine (VAWT).

This thesis aims to optimize the structural design of a VAWT rotor blade and to decrease the mass to area ratio by varying blade shape and structural layout. The choice of mass to rotor area ratio as an optimization function follows from the fact that this area is directly proportional to the energy output while mass drives production and installation costs. The VAWT is defined by an axis perpendicular to the unperturbed flow direction. The rotor geometry is described through a Troposkein shape. It is assumed that the blades carry their own weight leading to a reinforced root region. During operation the blades experience aerodynamic and inertia forces, which are deflecting the blades outwards, leading to an alternation of the aerodynamic loads. The interplay of load alternation and blade deflection could lead to a diverging flutter motion. After a fitting design is obtained, the blade motion has to be inspected for a safe use during operation.

The rotor is designed with an adjusted optimizer, originally written by M. Schelbergen [62]. The optimizer uses the Matlab optimization toolbox in combination with Nastran. The modification allows a smooth transition of the thickness of skin, shear web and girder. The airfoil section is varied along the blade. The optimization is based on load cases such as a parked rotor and the maximum up- and downwind forces. These loads are simplified and assumed to vary neither by the motion nor the deflections of the blade. In addition, an aeroelastic model is required to observe the blades' motion. Through out this thesis two aeroelastic codes were used. The *VAWT AeroElastic Multibody Panel Solver* (VÆMPS) was created by coupling Sandia National Laboratories OWENS and the near wake panel solver UMPM. However, its computational performance was not satisfying and it was decided to use HAWC2 coupled with an actuator cylinder model to determine the induction.

Through the modifications of the thickness distribution and the differing blade section height, the mass to area ratio was reduced significantly. For a 5 MW configuration the mass to area ratio was 58% lower than the original work by M. Schelbergen [62]. The lowest mass to area ratio of a Darrieus rotor appeared while using Carbon Fibre Reinforce Polymer with a NACA 0015 profile at the equator and a NACA 0040 at the roots. Additionally, this design had deflections with an amplitude of 0.45 m in flapwise direction and 0.5 m in edgewise direction.

The optimized designs do not show unstable motions. The up-scaled designs indicate a lower increasing gradient than the trend determined through the original work, showing that VAWT should be considered as Multi-Megawatt wind turbine design.

Acknowledgment

During the course of my Bachelor and Master education I met a lot of different people from a variety of countries, who I would like recognize in this thesis. Before I try to name them, I would like to thank my instructors and the PhDs, that made it possible to conduct this research and this thesis. Especially to Carlos, a big thank for developing this European master program.

Along the globe the Netherlands played a major role for me. Friends like Tobi, Bilo, Fred, Kiki and Martijn made me feel welcome and home. In the states I was welcomed through a lot of real Americans, such as Lenoré, Todd, Brian and Aaron & Joeun. It was pleasant to feel a bit of luxury, while being just a simple student.

In my native country, Germany, I am grateful to my parents and grandparents for providing me with the opportunity of this adventure. Also I like to memorize my friends, Phine, Laura and Marcus that have been with me for such a long time.

The final big thank goes to my girlfriend, Ulrike, who helped in the hour of need and gave me hope, whenever I needed it. I hope to return this favor in time.

B. Roscher
Delft, The Netherlands

29th June 2014

Who has seen the wind?
Neither I nor you:
But when the leaves hang trembling,
The wind is passing through.

By Christina Rossetti

Contents

Abstract	i
Acknowledgment	iii
List Of Figures	xi
List Of Tables	xiii
Nomenclature	xv
Thesis Outline	1
1 A Brief Overview On Vertical Axis Wind Turbines	3
1.1 Historical Review On Wind Energy With Emphasis On VAWTs	3
1.2 Motivation Of Thesis	7
2 State Of The Art In Analyzing VAWT	9
2.1 Optimization Types And Procedures	10
2.1.1 Conjugate Gradient Based Optimization	11
2.1.2 Genetic Algorithm Optimization	12
2.1.3 Kriging Optimization	13
2.2 Aerodynamic Models Of VAWT	14
2.2.1 Single Stream Tube (SST)	14
2.2.2 Double Multiple Stream Tube (DMST)	15
2.2.3 Actuator Cylinder	17
2.2.4 Vortex Models	18
2.2.5 CFD Models	20
2.2.6 Comparison Of Models	22

2.3	Structural Modeling	23
2.3.1	Computational Structural Dynamics (CSD)	23
2.3.2	Multi-Body Systems (MBS)	23
2.3.3	Modal Analysis	24
2.3.4	Beam Method	25
2.4	Numerical Aeroelastic Analysis	26
2.4.1	Interpolation Methods	26
2.4.2	Coupling methods	28
2.4.3	Commercially Available Codes	29
3	Components Of VÆMPS	31
3.1	Rotor Optimization	31
3.1.1	Objective Function	31
3.1.2	Design Variables	32
3.1.3	Constraints	33
3.1.4	Optimization Procedure	35
3.1.5	Determining The Interpolation	40
3.1.6	Starting Points Of Optimization	41
3.2	Aerodynamic Modeling Of A VAWT By UMPM	43
3.2.1	Energy Extraction	43
3.2.2	Inflow Behavior	45
3.2.3	Aerodynamic Forces	48
3.2.4	UMPM outline	50
3.3	OWENS - Structural Solver In VÆMPS	55
3.3.1	Structural Methodology	55
3.3.2	Cross-Section Model	57
3.3.3	Campbell Diagram	59
3.3.4	Structural Simulation	60
3.4	Numerical Aeroelastic Analysis	62
3.4.1	Interpolating Between Two Discretizations	62
3.4.2	Coupling Of Two Models	64
3.4.3	Initialization Of VÆMPS	66
3.5	Comparison Of HAWC2 And VÆMPS	67
4	Simulation Results	71
4.1	Overview Of Optimized Results	71
4.2	Stresses And Fatigue	75
4.3	Aeroelastic Analysis Of Optimized Designs	77
4.4	Campbell Diagram	83
4.5	Power Coefficient Curves Of Optimized Rotor Blades	86
4.6	Up-Scaling Of Optimized Rotor Power Output	86

5	Discussion And Critical Review Of The Optimization Results	89
5.1	Discussion	89
5.1.1	Optimization Results	89
5.1.2	Stress And Fatigue	90
5.1.3	Aeroelastic Evaluation	91
5.1.4	Campbell Diagram	92
5.1.5	Power Coefficient Diagramm	93
5.1.6	Up-Scaling Trend Of VAWT Rotor	94
5.2	Critical Review Of Results	94
6	Conclusions And Further Perspective	97
6.1	Conclusions	97
6.2	Further Research	98
6.2.1	Optimization Improvement	98
6.2.2	VÆMPS Improvement and Debugging	99
6.2.3	Additional Research Topics	99
A	Force Transformation	101
B	Parameter Study On A NACA 0018 Airfoil	103
C	Sandia 34m Testbed VAWTGen Input	109
D	Structural Input Of Optimized Blade Into HAWC2	115
E	Polar Data Of Used Airfoils	123
F	Loads On Optimized Blades	125
G	Blade Modes Of Optimized Blades	129
	References	133

List Of Figures

1.1	Early windmill concepts [31]	4
1.2	Windmills Pre-19th century	4
1.3	Darrieus concept [31]	5
1.4	FloWind turbine along the Tehachapi Pass [19]	5
1.5	H-rotor configuration	6
1.6	VESTAS bi-plane Darrieus [19]	6
1.7	3.5 MW Éole in Canada [19]	6
1.8	Graphical impression of floating HAWT and VAWT [46]	7
1.9	Future perspective of VAWT designs [46]	8
2.1	Finding local minimum with gradient base optimization [39]	12
2.2	Examples of reproduction methods	13
2.3	Interpolation of data points [39]	14
2.4	<i>Single Stream Tube</i> visualization	15
2.5	<i>Double Multiple Stream Tube</i> visualization with U_1 as the undisturbed wind speed.	16
2.6	Comparison of tangential forces of a VAWT, between MST and a Vortex code	17
2.7	Representation of Actuator Cylinder model, with normal and tangential force components projected along cylinder surface [22]	18
2.8	Change of circulation will be canceled with a wake circulation.	19
2.9	Horseshoe-vortex discretization of a straight wing [37]	19
2.10	Panel discretization of a straight wing	20
2.11	CFD mesh for 2D VAWT simulation [5]	21
2.12	Discretization of a H-rotor VAWT	24
2.13	Illustrations of a Multibody System	25

2.14	Mode shapes of SNL 34 m VAWT [53]	26
2.15	Graphical interpretation of aeroelasticity	27
2.16	Error in displacement on a log-log plot with different interpolation schemes [70]	28
2.17	Serial time coupling [69]	29
2.18	Staggered time coupling [69]	29
3.1	Discretization of the VAWT rotor [62]	32
3.2	Design vector of discretized rotor	33
3.3	Flow diagram of the optimization process [62]	36
3.4	Weight distribution along a VAWT blade span	37
3.5	Definition of inclination angle, along a Darrieus turbine	38
3.6	Gravitational loads on a VAWT	39
3.7	Power coefficient contour at various TSR and σ , with a NACA 0015	39
3.8	Normal and tangential force on two bladed VAWT	40
3.9	Initial thickness of a Darrieus 5MW	41
3.10	Schematic of shed vortex along streamlines	43
3.11	Force distribution along a VAWT with pure rotation	44
3.12	Time averaged circulation on a VAWT (top view) [17]	44
3.13	Inflow condition in a rotating frame	45
3.14	Time averaged inflow conditions at $\lambda = 7$ and $\sigma = 0.065$	46
3.15	Singularity panel representation with velocity representation	47
3.16	2D forces on VAWT blade during operations	48
3.17	Discretization of an H-rotor in UMPM	51
3.18	Lin-Cos spacing with different amount of points	51
3.19	Coordinate frame definition [15]	51
3.20	2D angle of attack comparison for frozen and free wake of a VAWT ($B=2$, $\lambda=3$, $\sigma=0.3$) [15]	54
3.21	Influence of calculation time with respect to the amount of used panels [65]	55
3.22	Timoshenko beam element	57
3.23	Operating coordinate systems of OWENS [53]	57
3.24	Graphical interpretation of a reinforced airfoil of a NACA 0035	58
3.25	Airfoil geometry points	58
3.26	Airfoil stiffness	59
3.27	Generated mesh of a VAWT by VAWTGen	60
3.28	System of OWENS framework [53]	61
3.29	Interpolation error at displacement of Nearest Neighbor and RBF with a support radius of $r = 10 \cdot \max(\Delta x_{struct}, \Delta x_{flow})$	63
3.30	C^2 Radial Basis Function with support radius of 0.4	63
3.31	Possible network communications in VÆMPS	65

3.32	Schematic interpretation of communication between the models	65
3.33	Definition of network strings	66
3.34	Azimuth angle definition	68
3.35	Displacement in H_1 versus time of the Sandia 34 m Testbed	68
3.36	Displacement in H_2 versus time of the Sandia 34 m Testbed	69
3.37	Averaged displacement versus azimuth angle of the Sandia 34 m Testbed .	69
4.1	Function value of finished optimization	72
4.2	Blade mass of finished optimization	73
4.3	Swept rotor area of finished optimization	73
4.4	Optimized blade shape of a 5 MW Darrieus turbine	74
4.5	Cross-section thickness distribution of inspected optimized rotors	76
4.6	Stress and fatigue of NACA 0015-35 with CFRP	78
4.7	Stress and fatigue of NACA 0015-40 with CFRP	79
4.8	Stress and fatigue of NACA 0030 with GFRP	80
4.9	Displacement versus time of designed blade at the mid-span position . . .	81
4.10	Displacement averaged for one revolution of designed blade at the mid-span position	82
4.11	Fourier analysis of displacement (given in Figure 4.9) of designed blade at the mid-span position	84
4.12	Campbell diagram of the designed blade including the displacement frequencies of the mid-span position	85
4.13	C_P versus TSR curve of designed blade	87
4.14	Scaling trend of VAWT rotor blades and HAWT designs [12, 18, 30, 71] .	87
B.1	Influence of Reynolds number on profile coefficient of a NACA 0018 . . .	104
B.2	Scaling of airfoil	105
B.3	Influence of chord elongation on profile coefficient of a NACA 0018	106
B.4	Visualization of panel buckling with spar at 0.35c	107
B.5	Influence of upper panel buckling with spar at 0.35c on profile coefficient of a NACA 0018	108
E.1	Extrapolated profile coefficient of NACA0015 at $Re = 10^6$ [21]	123
E.2	Profile coefficient of used airfoils at $Re = 10^6$	124
F.1	Force and moments on the NACA 0015-35 CFRP blade	126
F.2	Force and moments on the NACA 0015-40 CFRP blade	127
F.3	Force and moments on the NACA 0030 GFRP blade	128
G.1	Blade modes with profile NACA 0015-35 out of CFRP	130
G.2	Blade modes with profile NACA 0015-40 out of CFRP	131
G.3	Blade modes with profile NACA 0030 out of GFRP	132

List Of Tables

2.1	DeepWind baseline design [23, 24]	10
2.2	Comparison of VAWT aerodynamic models [61]	22
3.1	Material properties [14]	34
3.2	Boundaries of design variables	35
3.3	Aerodynamic loads during optimization	39
3.4	Comparison of the interpolation methods	40
3.5	Optimization starting point of inspected blade profiles	42
3.6	Initial control points of inspected blade profiles	42
3.7	Initial function values of inspected blade profiles	42
3.8	Fluid point overview [37]	47
3.9	Trade-off table for solver approaches during the aeroelastic analysis	62
3.10	Simulation parameter of comparison	67
3.11	Center of gravity points of SNL-blade	67
4.1	Minimum/maximum thickness, blade characteristics and optimization output of selected designs (NACA0015-35 (CFRP), NACA0015-40 (CFRP) and NACA0030 (GFRP))	75
4.2	Simulation environment of HAWC2 simulations	77

Nomenclature

Latin Symbols

b	Semi-chord of airfoil	[m]
c	Chord length	[m]
C_D	Drag coefficient	[–]
C_L	Lift coefficient	[–]
C_P	Power coefficient	[–]
C_Q	Torque coefficient	[–]
C_T	Thrust coefficient	[–]
C_t	Tangential coefficient	[–]
D	Drag force	[N]
D	Fatigue damage	[–]
F_{rot}	Centripetal force	[N]
k	spring constant	[N/m]
L	Lift force	[N]
M_{AC}	Moment around aerodynamic center	[Nm]
N	Normal force	[N]
N	Number of blades	[–]
N_{allow}	Allowable number of cycle of cyclic motion	[–]
q	Dynamic pressure	[kg/s^2]
R	Radius	[m]
R_σ	Stress ratio	[–]
T	Tangential force	[N]

t	Time	[s]
U	Undisturbed wind speed	[m/s]
V_{rel}	Relative velocity	[m/s]
Z	Scaling factor of airfoil thickness	[-]

Greek Symbols

α	Angle of attack	[deg]
β	Inclination angle of the Troposkien design	[°]
η	Flap-wise direction	[-]
Γ	Circulation	[m ² /s]
λ	Tip Speed Ratio (TSR) ($\lambda = \frac{\omega R}{U}$)	[-]
μ	Doublet strength	[m ² /s]
Ψ	Azimuth angle	[deg]
σ	Solidity	[-]
σ	Source strength	[m ² /s]
θ	Pitch angle	[deg]
ζ	Edge-wise direction	[-]

Abbreviations

AC	Actuator Cylinder
BEM	Blade Element Method
BM	Blade Mode
CFD	Computational Fluid Dynamics
CFRP	Carbon Fiber Reinforced Polymer
CGB	Conjugate Gradient Based
CSD	Computational Structural Dynamics
DMST	Double Multiple Stream Tube
DNA	DeoxyriboNucleic Acid
DNS	Direct Numerical Solution
DoF	Degree of Freedom
DTU	Denmark Technical University
EoM	Equation of Motion
FAST	Fatigue, Aerodynamics, Structures, and Turbulence
FEM	Finite Element Method
FSI	Fluid-Structure Interaction

GFRP	Glass Fiber Reinforced Polymer
HAWC2	Horizontal Axis Wind turbine simulation Code 2nd generation
HAWT	Horizontal Axis Wind Turbine
LES	Large Eddy Simulation
MBS	Multi-Body Systems
MST	Multiple Stream Tube
NREL	National Renewable Energy Laboratory
OWENS	Offshore Wind Energy Numerical Simulation tool
RANS	Reynolds Averaged Navier Stokes
RBF	Radial Basis Function
SNL	Sandia National Laboratories
SST	Single Stream Tube
TSR	Tip Speed Ratio
TU Delft	Delft University of Technology
U2DiV	2D potential-flow panel code
UMPM	Unsteady Multi-body Panel Method
VÆMPS	Vertical axis wind turbine AeroElast Multibody Panel Solver
VAWT	Vertical Axis Wind Turbine

Other Symbols

<i>AC</i>	Aerodynamic Center
<i>CG</i>	Center of Gravity
<i>EA</i>	Elastic Axis
<i>H</i> -frame	Hub frame
<i>n</i> -frame	Initial frame
<i>P</i> -frame	Platform frame
<i>SF</i>	Safety factor
NACA0015-35	Blade with NACA 0035 profile at root and NACA 0015 at equator
NACA0015-40	Blade with NACA 0040 profile at root and NACA 0015 at equator
NACA0018-35	Blade with NACA 0035 profile at root and NACA 0018 at equator

Thesis Outline

Offshore wind energy is a growing industry branch. Through the concept of placing turbines in deep water, a floating support structure becomes economic attractive. A possible rotor concept will be a VAWT, as it combines advantages that reduce the overall cost. An introduction to the problem is split into a historical retrospective, stated in chapter 1, and current state of the art (chapter 2).

The rotor blades have to sustain the operation and the parked condition. A low mass, a high area as well as aeroelastic stability are key requirements in the design phase. The rotor mass is driving manufacture and installation costs, while the area is directly proportional to the power output. The aeroelastic stability is ensuring a safe operation without any diverging flutter motion. In order to design such a blade it is necessary to know about the physical properties and behavior. An overview of the current state of the art can be found in chapter 2.

The blade design process is approached via two different simulation tools to keep the computational costs low, as mentioned in chapter 3. The design is determined through a modified version of the optimizer of M. Schelbergen [62]. The initial code returned a rough design which was improved significantly by smoothing the thickness distribution of the cross-section member. Thereupon, the determined design is evaluated by an aeroelastic simulation. Two tools have been available in this thesis. The first one is the Vertical axis wind turbine AeroElast Multibody Panel Solver (VÆMPS), a coupling of the Unsteady Multibody Panel Method (UMPM) from TU Delft (TUD) and the Offshore Wind Energy Numerical Simulation tool (OWENS) from Sandia National Laboratories (SNL). Nevertheless, its computational time was in no relation to the results. Therefore it was decided to use HAWC2 with the Actuator Cylinder model to determine induction.

Through out this thesis multiple blade cross-section of a 5 MW Troposkein VAWT were inspected on their mass to area ratio. The outcomes are displayed in chapter 4. Based on these results a discussion is done in chapter 5. In the end, a design was achieved that can be used to scale above 10 MW, at which it has a lower mass to area than commonly known HAWTs.

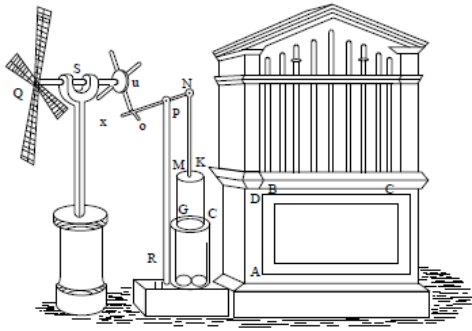
A Brief Overview On Vertical Axis Wind Turbines

Vertical Axis Wind Turbines could be seen as an alternative form of wind energy production. The usage of this technology is not really common, mainly due to a lack in research. Section 1.1 presents an historical review of VAWTs while section 1.2 presents the reasoning for their application as floating wind turbines.

1.1 Historical Review On Wind Energy With Emphasis On VAWTs

Harvesting wind energy began years ago. In the beginnings sailors used the power of wind to transport heavy goods. The first known windmill illustration was made in the 1st century BC by Hero of Alexandria under the name *Pneumatics* [31]. An image of this invention can be found in Figure 1.1a. It is not clear whether this machinery actually existed, but from the schematic the purpose of grinding corn becomes clear. Another early concept was developed in 900 AD by Persians [68]. This windmill was drag driven and the first to rotate around its vertical axis. An image of the windmill is displayed in Figure 1.1b. Nowadays, such a configuration is known as Savonius rotor.

In Europe, the windmills appeared in the 12th century [31]. While the purpose of grinding corn and pumping water remained, the design had changed a lot. The windmill was mounted on a house and faced the wind direction. The rotor design consisted of 4 sails rotating around a horizontal axis, thereby transmitting the motion to the grind stones. Before the industrial revolution, windmills were one of the major energy sources [33]. Up to the 18th century the European windmills were developed further by having sails as blades and being slightly twisted; an impression can be found in Figure 1.2a. Meanwhile, a different configuration established in the United States, a multi-bladed windmill, referred to as *fan mills* [31]. This wind mill was used mainly for pumping water, which is the



(a) Hero's windmill (1000 BC)



(b) Persian windmill (900 AD)

Figure 1.1: Early windmill concepts [31]

(a) Dutch Windmill



(b) American fan mills

Figure 1.2: Windmills Pre-19th century

origin of its nickname *Pumping Jack*. An example is given in Figure 1.2b. Until the 19th century over 6 million fan mills were built in the US [33].

In 1887 began the era of electricity in wind energy in Great Britain and the United States, where the first wind turbines, capable of producing electricity, were presented [51]. The baseline of all modern HAWT configurations is the Danish Design by LeCour, who conducted his research in 1890 [68]. The development of a more efficient generator boosted the wind energy sector too. In 1931, G. Darrieus [13] proposed a design that uses lift to generate torque around a vertical axis. Lift reaches greater values than drag when experiencing the same velocity and will have a greater efficiency [68]. Darrieus patented his rotor shape also known under the name Troposkien (Figure 1.3) and became the starting point of VAWTs. Colloquially this shape is referred to as eggbeater.

Around the 1980s intensive research projects were started in Sandia National Laboratory (SNL) with a 17 m high Darrieus shaped turbine [63]. FloWind bought the design and made it popular through placing thousands of turbines in the United States (Figure 1.4). As a result FloWind became the most successful VAWT manufacturer.



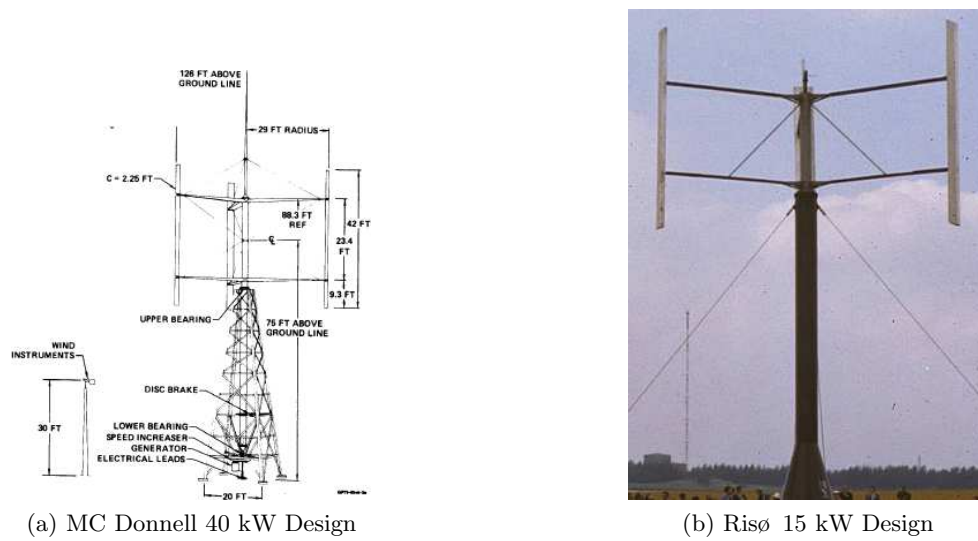
Figure 1.3:
Darrieus concept [31]



Figure 1.4: FloWind turbine along the Tehachapi Pass [19]

Next to the Darrieus shape, another shape started to appear. Dr. Peter Musgrove suggested a VAWT with straight blades, also known as *H-type rotor* [19], which Mc Donnell used to develop a 40 kW H-rotor (Figure 1.5a) [2]. This kind of rotor had the advantage of not being protected by Darrieus patent, through the difference in rotor shapes. At the same time the concept of VAWTs started to spread in Europe. Risø engineered their own H-rotor which was capable of producing 15 kW (Figure 1.5b [19]). VESTAS also tried their own concept of a VAWT which had an increased stiffness resulting out of the bi-plane Darrieus (Figure 1.6).

Already at that time the idea of Multi-Megawatt turbine arose as seen on the *Éole* (Figure 1.7) which had a rated power of 3.5 MW. It only operated from 1987 to 1993, due to the fact that bearings and maintenance were too costly [25]. Not only is *Éole* the biggest VAWT, it can also be seen as the last milestone of the early generation. When the oil-prizes returned to a normal level, the interest in renewable energy declined and as



(a) MC Donnell 40 kW Design

(b) Risø 15 kW Design

Figure 1.5: H-rotor configuration*Figure 1.6: VESTAS bi-plane Darrieus [19]**Figure 1.7: 3.5 MW Éole in Canada [19]*

a consequence the VAWT research stopped, while the development of HAWTs continued. At the beginning of the 21st century renewable energies came more into focus to counter the rapid climate change. In 1991 in Vindeby (Denmark) the first turbine was placed offshore [51], initializing a new technology sector.

With the new operational environment it needs to be evaluated if VAWTs could be a more suitable option for the offshore energy production than HAWTs. The rising energy demand is pushing the current designs to their limit. In order to evaluate the performance of a design, it is important to obtain results fast. Constructing a prototype is only an option during later design stages as it will be a costly evaluation. Therefore developing a simulation tool, that is capable of running different rotor shapes and airfoil selections, has become a high priority.

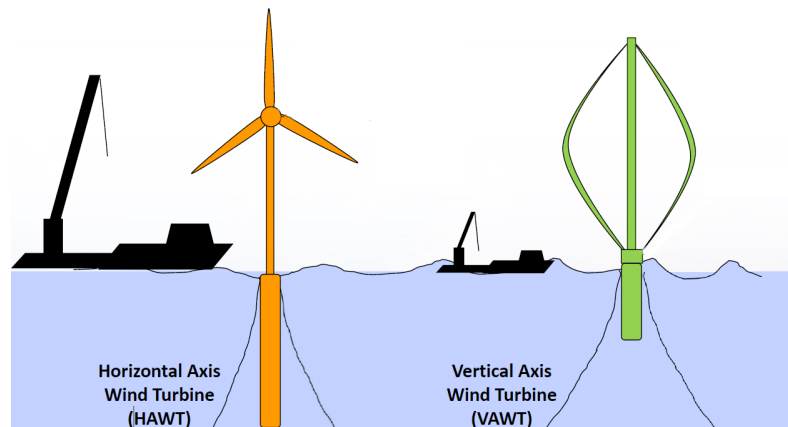


Figure 1.8: Graphical impression of floating HAWT and VAWT [46]

1.2 Motivation Of Thesis

As the electricity consumption increases, the energy generation has to keep up. Fossil resources are limited and might be depleted in the future. An alternative is *Sustainable Energy*, which embraces terms such as photovoltaics, water energy and bio gas. Next to those is wind energy, which is associated with a HAWT. Another possible option is a VAWT. The research on that topic was stopped because of reasons, such as:

- High rotor weight with respect to generated kW
- Low fatigue life
- No active control mechanism
- Lack of funding

But the research on VAWTs came back with the idea to placing them offshore, especially in combination with a floating support structure. Figure 1.8 gives an impression of some advantages. The support rig of a VAWT is shallower, resulting in a lower weight and therefore lower costs [46]. Other advantages are:

- Independence of inflow direction, meaning that no yaw mechanism is needed
- Generator is located in the base of the structure, making it more accessible, which can lead to a reduction of the maintenance cost
- The center of gravity is closer to the ground, because the rotor is mounted on the base and the generator is moved down, which leads to a smaller floating support structure, as seen in Figure 1.8

These advantages give the opportunity to start an investigation. Four parties began to develop a new design that can be used offshore; SNL, DTU, Nenuphar and Wind Power Ltd. An overview of their concepts is displayed in Figure 1.9. The DeepWind turbine is the only one which is similar to the original Darrieus Design. The design proposed by Nenuphar is a twisted H-rotor. The most abstract design is the Aerogenerator by Wind Power Ltd, where the blades are mounted on a long beam, such that they have a longer arm to create torque.

Still the rotor design is a big issue, especially the relation between swept area and rotor mass. As a motivation the thesis aims to solve the following research question:

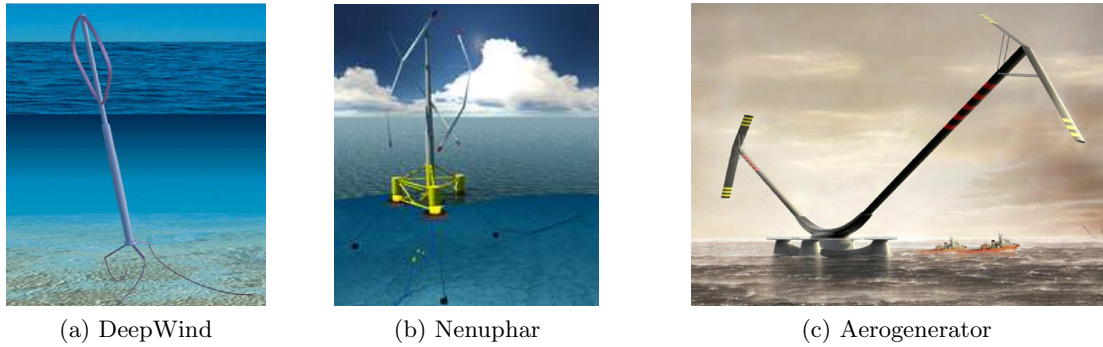


Figure 1.9: Future perspective of VAWT designs [46]

What is an optimal rotor design for a vertical axis wind turbine with a low mass to area ratio while the turbine is aeroelastically stable?

An optimizer in combination with a structural solver is used to determine the topology and the internal structure of the blade at a given load condition. After a design is found an aeroelastic solver can be used to check for flutter, which is a self-starting oscillation caused by the interaction of unsteady aerodynamics and structural dynamics. In the end a design will be found that is capable of a 20 year lifetime and a low mass.

State Of The Art In Analyzing VAWT

Currently, institutes focus on downwind-turbines, high-altitude turbines and VAWT as alternative wind energy technologies. The major research institutions in this field are 'Sandia National Laboratories' (SNL), 'Denmark Technical University' (DTU), 'Delft University of Technology' (TU Delft) and 'Fraunhofer Institute for Wind Energy and Energy System Technology' (IWES). SNL and DTU obtained a research grant to investigate the capability of floating VAWTs in 2011 [25]. TU Delft is cooperating with both for developing simulation tools to design a Multi-Megawatt Darrieus on a floating support structure.

In Table 2.1 the baseline design of the DeepWind concept of DTU can be found. Despite being still in the design phase, the data already gives an impression of the dimensions required to achieve 5 MW. In order to be competitive the research groups investigate the capability to scale the design to greater power outputs. DTU recently plans to go for a 15 MW turbine in cooperation with TU Delft. Meanwhile at SNL discussions are held about their desired size and rotor configuration.

Constructing prototypes of such size is costly and ineffective. This approach is not an option for finding an optimal design. An optimization tool receives high significance, to find the best fitting rotor geometry which has a low mass and still converts the maximum possible energy. An advantage would be that such a tool could be validated with an already existing smaller VAWT. Also it could be possible to have multiple simulation tools and compare them to each other, which is planned between DTU and SNL. DTU created an aeroelastic tool, known as HAWC2, which is described in section 2.4.3. SNL has a solver known as OWENS, which consists of separate solvers that focus on hydrodynamic, aerodynamic and structure, which are coupled with each other, either loosely or closely. Through out this thesis only the structural solver of OWENS will be used. It will be combined with the vortex-wake model of TU Delft (UMPM), to create a new aeroelastic solver, called VÆMPS (Vertical axis wind turbine AeroElast Multibody Panel Solver), which will be outlined in chapter 3. In the following sections an overview will be given

of the current state of knowledge focusing on all components that are required to cover the topic of this thesis, a structural optimization of VAWT followed by an aeroelastic analysis.

Table 2.1: *DeepWind baseline design [23, 24]*

Geometry		
Rotor radius	[m]	63.74
Rotor height	[m]	129.56
Chord	[m]	7.45
Solidity	[-]	0.23
Swept area	[m ²]	10743
Amount of blades	[-]	2
Airfoil		NACA 0018
Performance		
Rated power	[kW]	5 103
Rated rotational speed	[rpm]	5.26
Rated wind speed	[m/s]	14
Cut-in wind speed	[m/s]	5
Cut-out wind speed	[m/s]	25

2.1 Optimization Types And Procedures

Currently, there are publicly no rotor optimizer available focusing on a VAWT. Papalambros [54] defines optimization as:

The determination of values for design variables which minimize (maximize) the objective, while satisfying all constraints.

The definition introduces three terms, which need to be described to declare a solvable problem. A good optimization requires design variables (i.e. rotor height and width), an objective (i.e. lowest mass, lowest cost) and constraints (i.e. lifetime of 20 years). These three terms will vary depending on the problematic. The definitions in this thesis can be found in section 3.1. One of the major challenges in optimization is the applied algorithm. A short list of common optimizers can be found below [54].

- *Brute-Force optimization*
Tries out every possibility, which will lead to high computational cost and a lot of iterations.
- *Steepest Descend*
Executes a line search in the direction of the steepest descend and at the minimum of that line the new steepest descend will be determined. This algorithm will be repeated until a minimum inside the design domain is found. The disadvantage of *Steepest Descend* is that the algorithm might follow a zig-zag line until it reaches a minimum (see Figure 2.1a), meaning a lot of iterations and therefore a longer computational time.

- *Nelder-Mead Simplex*
Determines three design points and then moves into the opposite direction of the worst point. This method has the risk of ending in a cycling solution, if no relaxation terms are included.
- *Particle Swarm method*
Starts with a population of multiple points, each moving individually along the design space. At each evaluation the swarm determines the single fitness values. The new search direction is then determined out of steepest descend and the highest fitness value of the entire swarm.
- *Quasi-Newton method*
Is a second order optimization, which produces fast satisfying results, but its advantage of being second order has the drawback, that the gradient of the gradient needs to be determined, which becomes costly for complex functions.

In preparation of this thesis, three different procedures have been discussed in more detail: the Conjugate Gradient Base (CGB), Genetic Algorithm and Kriging optimization.

2.1.1 Conjugate Gradient Based Optimization

The method is based on the *Steepest Descend*. It also consists out of the determination of the search direction and simple line search. But in the CGB optimization the search direction is a summation out of the gradient at the actual point and the previous search direction, which is relaxed by the squared fraction of the actual and the previous gradient (see step 3). The abstract of the algorithm can be found below [39].

1. Start with arbitrarily starting point X_1
2. Set first search direction $d_1 = -\nabla f_1$
3. Next search direction $d_i = -\nabla f_i + \frac{\|\nabla f_i\|^2}{\|\nabla f_{i-1}\|^2} d_{i-1}$
4. Line search to lowest point along the line $X_{i+1} = X_i + \alpha d_i$
5. Repeat step 3 until convergence otherwise use step 6
6. Restart every $(N + 1)$ steps, using step 2

In the procedure the direction d is a gradient of a function f and will be multiplied with the constant α until the next lowest point X_{i+1} . In step 2 and 3 it is required to determine the Jacobian of the objective function, which can be done by either a finite scheme or an analytic solution. The more complex the Jacobian is, the more difficult it will be to determine an analytic solution, so a finite scheme such as the central difference scheme is of great help. In theory the optimizer will find a solution in less than N steps, where N describes the amount of design variables [39]. If this is not happening at step $N + 1$ the optimizer has use the gradient of the current point, as in step 2 and follow the normal scheme afterwards. In Figure 2.1b the solving algorithm of gradient

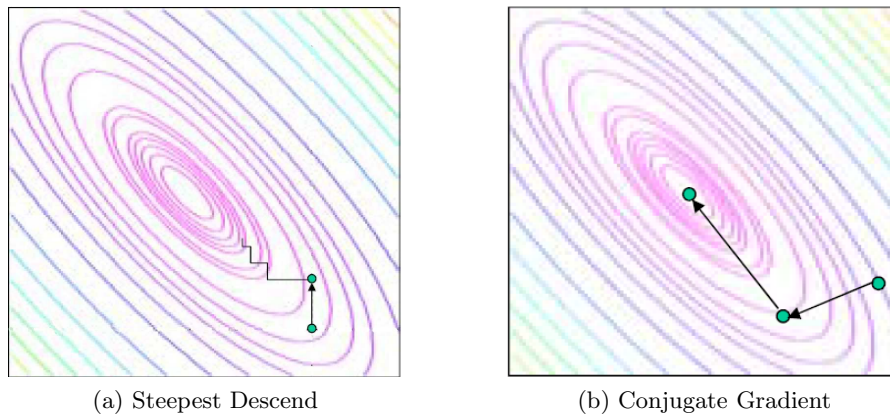


Figure 2.1: Finding local minimum with gradient base optimization [39]

optimization can be observed, the first step is perpendicular to the isolines. When the minimum is reached along this line, a new search direction is determined as described in step 3. While comparing the *Steepest Descent* in Figure 2.1, it becomes clear that if the search direction remains perpendicular to isolines, more iterations are needed than with the CGB algorithm.

If the domain is bounded by constraints and the line search ends at a restriction, the new search direction will be along the descending boundary. A disadvantage of the model is that it leads to an optimum, which might not be the global one. Therefore it is recommended to rerun the method multiple times, with different initial points X_1 to ensure that the method finds a global optimum [58].

2.1.2 Genetic Algorithm Optimization

The genetic algorithm is close to nature and represents a zero order optimizer, meaning only the variables and their function value need to be known. Every creature on earth has a DNA-string, also every objective can be modeled as a DNA-string, as a combination of design variables. With each iteration step, a population is generated, modified and evaluated on their fitness. According to Darwins law only the fittest will survive [59]. The algorithm initializes by defining an amount of n different starting points, called a population. The fitness of each point is determined and the toughest designs are selected as parents. These parents will generate the new population for the following evolution. A new generation can be achieved in multiple ways as presented in [59]. A short summary is given below:

- *Cross-over*

A specific amount information bits of parent A is coupled with the ones of parent B in order to form a new child. In the example given in Figure 2.2a it can be seen that parent A passes on the first and the last part of the DNA, while parent B supplies the other digits. The cross over can be done in a variety of ways, by either splitting the DNA and using sequences or by choosing randomly the segment which will be handed down.

- *Mutation*

Instead of having a perfect replica, some single parts will be created randomly without any relation to the parents which is than called Mutation. In Figure 2.2b it can be seen that the child will obtain information from its parents, but its third DNA segment is mutated. This method ensures that in every iteration step there is a bit of variety.

- *Swap*

Swapping, describes the process of interchanging parts of the DNA out of a different position of the same member of the population, as shown in Figure 2.2c.

- *Reproduction*

Reproduction can also be seen as creating a copy of a parent, no new variety is introduced by this method. This approach is always connected to an elitism, where the fittest member of the current generation, will be reused in the new population.

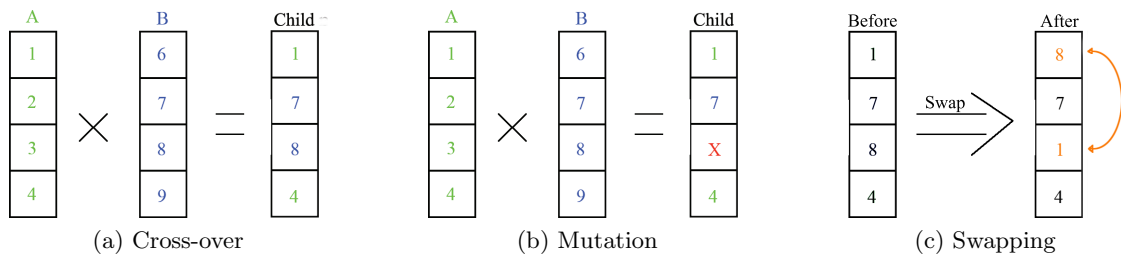


Figure 2.2: Examples of reproduction methods

The entire procedure of generating a population, evaluating a function value and creating children, will be done either a certain amount of generations or till the difference of the fitness values remain constant.

2.1.3 Kriging Optimization

The last method was developed by D.G. Krige, a mining engineer. The algorithm is a correlation between neighboring points with a surface interpolation that is most likely [50]. In order to do so multiple simulation results of different configurations, such as tip speed ratio, solidity and airfoil profiles, are required to create a representative database. SNL implemented this optimization approach in DAKOTA, a general multidisciplinary optimization tool [1]. Instead of multiple iterations and executions of the objective functions the optimum can be found by inspecting the interpolated domain. The visualization of a multidimensional domain is complicated and therefore limited to three dimensions in Figure 2.3. Depending on the correlation between the points the domain becomes either more spiky ore more flat. An advantage of the algorithm is that once the database is handed down to DAKOTA, the optimization only depends on the wanted objective and the weighting between the variables. This reduces the computational time and effort, such that no additional runs are required after the database is created.

Kriging also has disadvantages, which make its usage less favorable. The Kriging is an interpolation method, which smooths the surface of the domain. Such smooth behavior

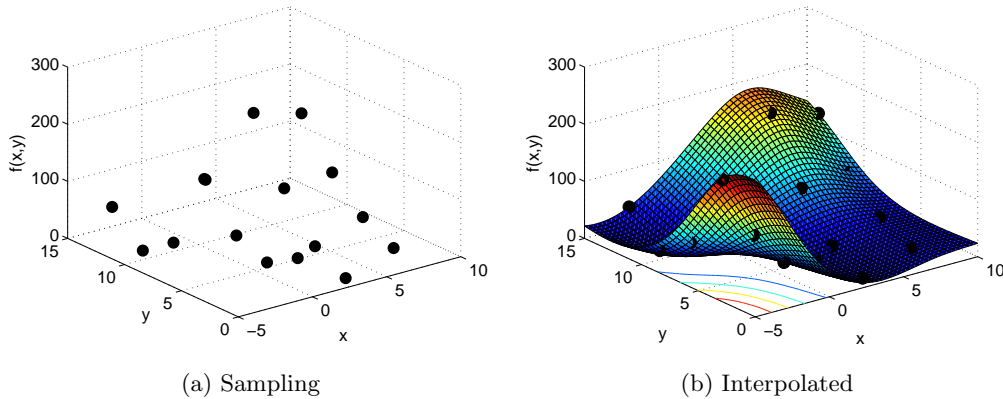


Figure 2.3: Interpolation of data points [39]

is not valid if the objective are discontinuous or non-differentiable, the results might be therefore not physical feasible. In order to get a good approximation of the function value surface, a lot of data points are required.

2.2 Aerodynamic Models Of VAWT

The engineering model that was used mostly in the early stage was the stream tube model. The idea of having a permeable actuator disc is obtained from HAWTs. However, it can be modified for the use with VAWT. The base concept of the models is the conservation of mass and momentum, independent of the rotational axis. The concept describes that the mass flow in has to be equal to the mass flow out, simultaneously the stream velocity is reduced as the actuator disc extracts energy. According to Bernoulli's law the cross-section has to increase in order to keep the mass flow constant at lower velocity [32]. The first model based on this principle is the single stream tube (subsection 2.2.1), which was redefined with multiple stream tubes (subsection 2.2.2). With respect to HAWT the method is known as Blade Element Method (BEM), in the VAWT section the method is known as Double Multiple Stream Tube (DMST). Unfortunately, the accuracy of these models was lagging on the differentiation between up- and downwind position. With the increasing computational power new models are in development to increase the accuracy. This thesis will layout briefly some of these models briefly and compare them. In addition models such as the Actuator Cylinder model (subsection 2.2.3), a CFD approach (subsection 2.2.5) and a Vortex method (subsection 2.2.4) are included as well.

2.2.1 Single Stream Tube (SST)

In HAWT configuration the rotational plane is described by a disc, as it is defined by the Single Stream Tube. Obviously VAWT blades project a cylinder that is parallel to the stream tube, which results that the blades cross the normal actuator disc twice along their upwind and downwind path, as seen in Figure 2.4. Instead of having a single line, the rotor will be displayed as a zone in which the induction has to be determined.

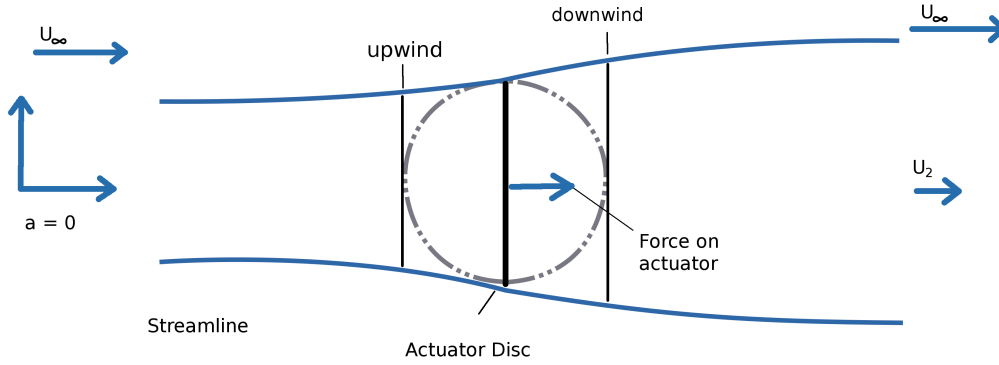


Figure 2.4: Single Stream Tube visualization

Templin [64] suggested this method in 1974 for the use in VAWT. The induction factor a in the zone can be determined with help of the momentum continuity, displayed in Equation (2.3) [6], where it depends on the solidity σ and the tip speed ratio (TSR) λ and the azimuth angle Ψ . These non-dimensional values can be used to describe wind turbines configurations, independently of their actual dimensions. The solidity indicates the portion of occupied space in the swept area (Equation (2.1)). The tip speed ratio traces how fast the wind turbine is spinning with respect to the undisturbed wind speed (Equation (2.2)).

$$\sigma = \frac{Nc}{2R} \quad (2.1)$$

$$\lambda = \frac{R\omega}{U} \quad (2.2)$$

$$a = \frac{\sigma}{\pi} \lambda \sin \Psi \quad (2.3)$$

The SST is a simple tool, which does not include the blade-wake interaction and along the downwind path the blade is assumed to receive a reduced, undisturbed flow velocity. This is only partially valid as the flow was disturbed earlier. These assumption and simplification are leading to a large reduction in accuracy.

2.2.2 Double Multiple Stream Tube (DMST)

In BEM multiple stream tubes are used, the same is done in DMST. Initially SST was extended with another stream tube, dividing the zone into a up- and downwind, which was followed by a model that discretized the swept area into independent multiple slices [63]. Finally the projected surface was sliced along its length and its cross-section, constructing the DMST, defined by Strickland [63]. In Figure 2.5 one of multiple sections is displayed, while passing through up- and downwind the airfoil is crossing the section twice. On the downwind site, the wind speed is defined to have a lower free stream as the upwind path, as there was a reduction of energy in upwind path. DMST also assumes the flow to be undisturbed, independently of its location, which neglects the fact that a wake was shed earlier. Such an assumption is considered to have a low accuracy.

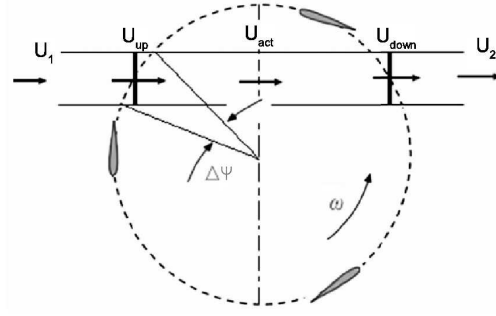


Figure 2.5: Double Multiple Stream Tube visualization with U_1 as the undisturbed wind speed.

An indication of the efficiency is the power coefficient C_P , which is equal to the ratio of extracted and available power in the swept area. Equation (2.4) is the commonly known definition of the power coefficient, in which P_{elec} represents the converted power, ρ the air density, U the undisturbed wind speed and A the swept rotor area.

$$C_P = \frac{P_{elec}}{0.5\rho AU^3} \quad (2.4)$$

For every actuator disc piece it is possible to determine the power output, when the location of the blade is known. This can be done with the help of the rotational speed ω , solidity σ and the amount of used stream tube pieces m . The C_P was defined by Paraschivoiu [55] to be the product of the torque coefficient C_Q and the tip speed ratio λ (Equation (2.5)). Supplementary the following equations are needed. The torque coefficient is the sum of all products of tangential force coefficient C_t and squared, normalized, relative velocity (Equation (2.6)). The velocity is determined by a simple geometric relation (Equation (2.8)) that is dependent on the azimuth angle Ψ . The tangential force coefficient is the summation of the projection of lift and drag coefficients (C_L and C_D) with the angle of attack α on the reference frame (Equation (2.6)). The angle of attack can also be estimated with a geometric relation (Equation (2.9)). V_{Rel} and α are dependent on induction factor a , which is used to indicate the reduced wind speed approaching the blade. The induction factor is the reduction without any disturbance in the flow [5], which is only valid along upwind path.

$$C_P = C_Q \lambda \quad (2.5)$$

$$C_Q = \sigma \sum_{i=1}^{2m} \frac{\left(\frac{V_{Rel,i}}{U}\right)^2 C_{t,i}}{2m} \quad (2.6)$$

$$C_t = C_L \sin \alpha - C_D \cos \alpha \quad (2.7)$$

$$\frac{V_{Rel}}{U} = \sqrt{((1-a) \sin \Psi)^2 + ((1-a) \cos \Psi + \lambda)^2} \quad (2.8)$$

$$\alpha = \arctan \left(\frac{(1-a) \sin \Psi}{(1-a) \cos \Psi + \lambda} \right) \quad (2.9)$$

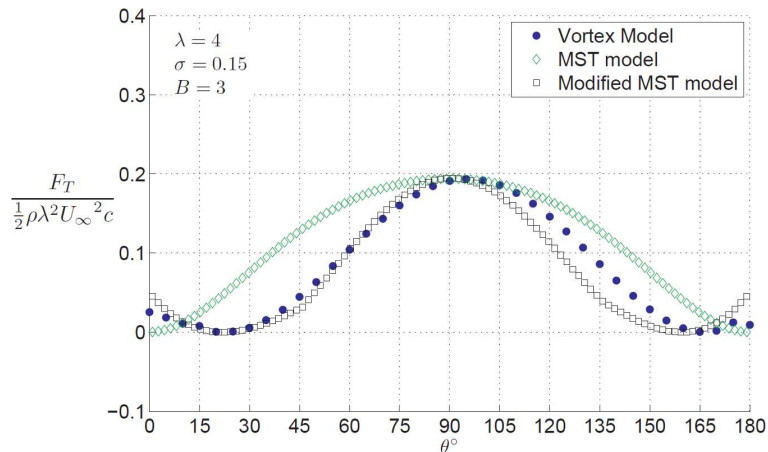


Figure 2.6: Comparison of tangential forces of a VAWT, between MST and a Vortex code

DMST was considered as a major design tool such as the BEM, due to its simplicity and fast response. Only high fidelity models proved the inaccuracy of the model [17]. In the original DMST it is assumed that the flow only experiences an induction factor parallel to the flow, but there is also an induction factor perpendicular to the flow, which is due to the rotational motion. C.S. Ferreira [17] proposed that the lateral induction factor should be included to improve the DMST. This can be achieved by treating the induction zone as a circulation problem. In the circulation problem a small vortex is released along the path, while the major vortex contribution appears in the transition between up- and downwind. The influence of these suggestion can be seen in Figure 2.6. The modified version approaches the curve, determined with a vortex model. The offset between both is still existent but less and thereby showing an improvement.

2.2.3 Actuator Cylinder

The last model based on the conservation of mass and momentum is the Actuator Cylinder model (AC) [22]. As the name indicates, the model uses a cylinder instead of a disc, which is more equivalent to the swept surface, especially when the rotor has a H -configuration. The forces can be projected along the surface in tangential and normal direction, as seen in Figure 2.7. The AC is developed as a 2D solver, which means that forces in z -directions will be projected onto the cylinder surface.

The forces on the blade can be determined when the relative velocity, consisting out of wind speed and rotational speed, is known. Helge A. Madsen [22] uses the Euler and the continuity equation to determine the velocities in x and y direction (Equation (2.10) and (2.11)). If the representing azimuth angle Ψ is known, it is possible to determine the normal and tangential forces, which then lead to the power coefficient (Equation (2.12)) [43]. In addition the airfoil can pitch θ , which is a combination of a predefined blade twist, a setting of the blade orientation and an angle from the elastic deformation obtained through the forces acting on the structure. The Actuator Cylinder is a rather complex model, which still produces fast responses. Nevertheless it needs to be kept in mind that the AC uses the following simplifications:

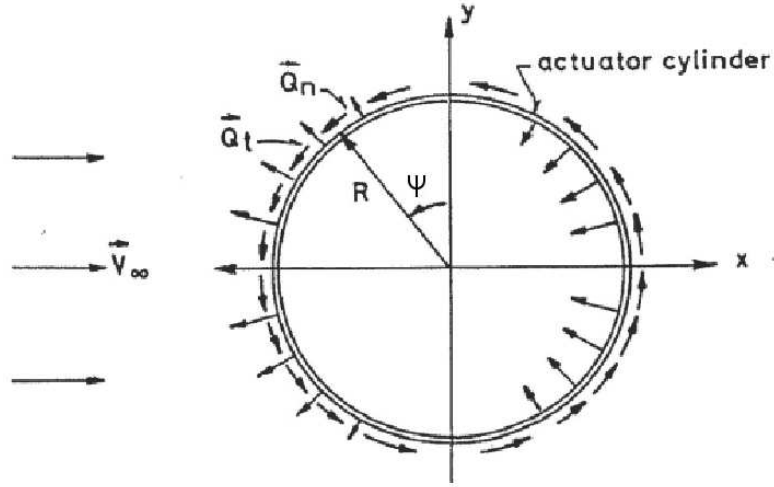


Figure 2.7: Representation of Actuator Cylinder model, with normal and tangential force components projected along cylinder surface [22]

- 2D-model
- no wake-blade interaction
- Darrieus will be discretized as a cylinder

$$U_x = -\frac{1}{2\pi} \int_0^{2\pi} \frac{-x(x + \sin(\Psi)) \sin(\Psi) + (y - \cos(\Psi)) \cos(\Psi)}{(x + \sin(\Psi))^2 + (y - \cos(\Psi))^2} d\Psi - Q_n(\cos^{-1}(y))^* + Q_n(-\cos^{-1}(y))^{**} \quad (2.10)$$

$$U_x = -\frac{1}{2\pi} \int_0^{2\pi} \frac{-x(x + \sin(\Psi)) \cos(\Psi) - (y - \cos(\Psi)) \sin(\Psi)}{(x + \sin(\Psi))^2 + (y - \cos(\Psi))^2} d\Psi \quad (2.11)$$

$$C_P = \frac{\frac{1}{2\pi} \int_0^{2\pi} B (F_t(\Psi) \cos(\theta) + F_n(\Psi) \sin(\theta)) \omega d\Psi}{\rho U_1^3} \quad (2.12)$$

2.2.4 Vortex Models

Vortex models are a different kind of aerodynamic models with respect to the ones named earlier. Instead of being based on momentum and mass conservation, the vortex models use the principle of the Kelvin theorem, where the change of circulation in time has to be equal to zero (Equation (2.13)). Kutta-Joukowski [37] stated that an airfoils lift L' can be described with the product of velocity U , density ρ and circulation Γ (Equation (2.14)). Normally a change of the angle of attack will lead to a different lift force, which will mean that the circulation has to change as well. In order to compensate this change, another circulation has to be released in the form of a wake. Figure 2.8 displays the counter acting circulation after a change of lift. This circulation will be transported downwind, where its effect vanish with the distance. In general the vortex method can be differentiated into two groups, defined by their discretization as either a single line or as mesh consisting of multiple panels.

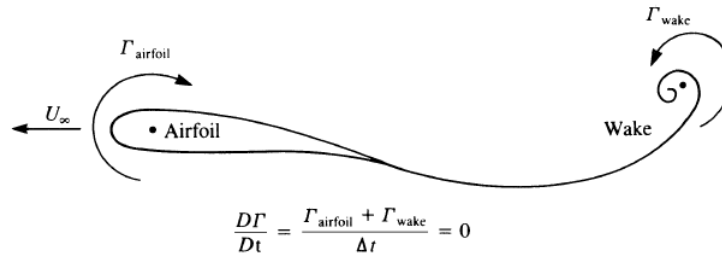


Figure 2.8: Change of circulation will be canceled with a wake circulation.

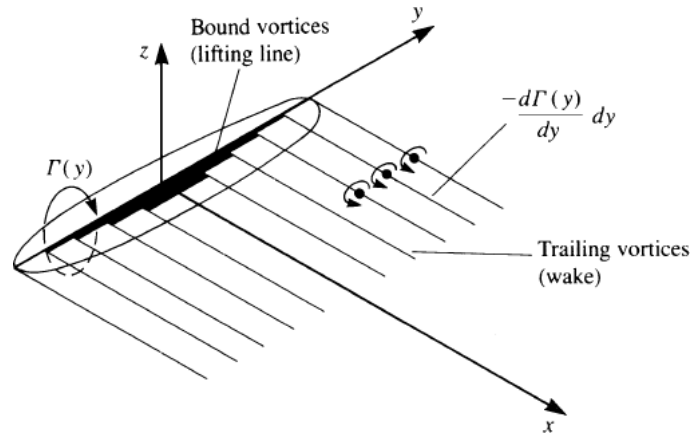


Figure 2.9: Horseshoe-vortex discretization of a straight wing [37]

$$\frac{D\Gamma}{Dt} = 0 \quad (2.13)$$

$$L' = \rho U \Gamma \quad (2.14)$$

Lifting Line

The lift of an airfoil can be represented as a single circulation. Following from that an entire blade can be projected as a single line of circulations. Kelvins theorem requires to have a closed vortex filament, leading to a circulation distribution extended on the sides and far downstream. Such a filament is shown in Figure 2.9, it can be noted that not just one filament is displayed. This is due to the fact that one single circulation would be a too rough estimation of the elliptic lift distribution, therefore multiple filaments are added on top of each other, creating a step function of the circulation distribution. Sandia National Laboratories implemented the lifting line concept as an aerodynamic model for VAWTs, known as CACTUS. The problem in the implementation is that the lifting line has to operate on a rotating frame, where it passes its own wake. At that instant the model has complications to capture the blade wake interaction, because the entire blade is only seen as a single line.

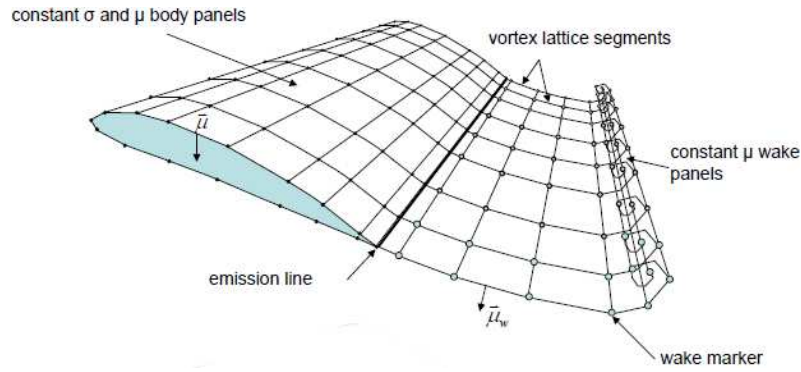


Figure 2.10: Panel discretization of a straight wing

Vortex Panel Method

As mentioned this method discretizes the entire blade as connected panels, while creating an enclosed surface, which is helpful during blade wake interaction. Every panel edge has its own circulation in order to satisfy the impermeability of the surface. Next to the wing also the wake is discretized as panels, as seen in Figure 2.10. The connection between wake and blade always has to remain there, such that every time step another row of panels has to be added. It becomes clear that with every time step the computational cost is increasing, which will require an approach to speed the code up. TU Delft implemented a vortex panel method, known as Unsteady Multibody Panel Method (UMPM). They also included possibilities to reduce the computational time, which are named later in the section 3.2, due to the fact that the UMPM is used in this thesis to develop VÆMPS.

2.2.5 CFD Models

Another option of inspecting the aerodynamics is through the usage of Computational Fluid Dynamics (CFD). The solver fills the domain with finite control volumes, which are permeable and obey to the conservation of mass. Next to filling the domain with control volumes, it is required to define the boundaries of the domain, by either knowing the values at the edge of the domain (Dirichlet boundary conditions) or its flux (Neumann boundary conditions). After the model is defined, it is possible to solve the Navier-Stokes equation (Equation (2.15)) and the continuity equation (Equation (2.16)) for every control volume and time step. In the equations \vec{v} is representing the flow velocity, ρ the fluid density, p the pressure, \vec{T} the stress tensor on the fluid and \vec{f} the external forces. A valid assumption on this setup is that the fluid is incompressible, due to the fact that the Mach number is below 0.3 [32], which will simplify the continuity equation to Equation (2.16).

$$\rho \left(\frac{\delta \vec{v}}{t} + \vec{v} \cdot \nabla \right) = -\nabla p + \nabla \cdot \vec{T} + \vec{f} \quad (2.15)$$

$$\nabla \cdot \vec{v} = 0 \quad (2.16)$$

As it can be recognized in Figure 2.11, the domain of such a problem has to have a fine grid in order to be sufficient. A drawback is that a fine grid will increase the computational

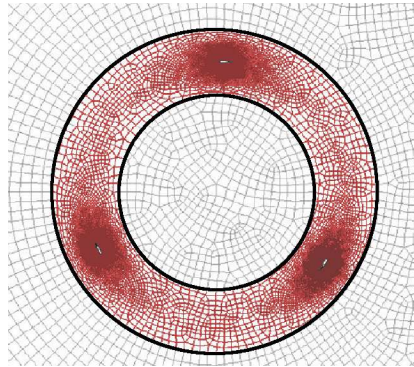


Figure 2.11: CFD mesh for 2D VAWT simulation [5]

cost. In a 2D case every increase of columns and rows of rectangular control volumes will raise the computational cost by the power of 2 [7], therefore Martin O.L. Hansen [45] divided his domain into a moving (red lines) and static grid (grey lines). This split of domains is known as Multigrid [7] and reveals the opportunity to save computational cost. Other options to reduce computational time and cost are listed below [7].

- *DNS*
Direct Numerical Solution, is the direct solving approach of the Navier-Stokes equation. DNS is capable of solving the domain up to the smallest detail at which the change of momentum is equal to zero inside a single control volume. Because of the high accuracy and no simplifications, DNS can be seen as a costly brute-force solver. If the domain is large it will be more wisely to use another approach to solve the CFD model.
- *RANS*
Reynolds Averaged Navier Stokes solver, uses a slight modification of the Navier Stokes. RANS inspects the problem as a superposition problem, the problem is decomposed in a time-averaged value and its fluctuation. This will require less iterations and thereby decrease computational costs. A drawback of RANS is that it is not capable of simulating an unsteady aerodynamic, which is needed for Dynamic Stall. URANS is trying to include unsteady terms, but its validation is still open.
- *LES*
Large Eddy Simulation is a solver that only determines the conservation of momentum up to a certain size of turbulence. Values lower than this size will be neglected or determined with another turbulence model. By neglecting smaller turbulence, the computational cost can be kept low and allows a self defined fidelity.

These methods decrease the cost, while maintaining a certain amount of accuracy. CFD is a fidelity model that should be used in the sense of analyzing specific areas of interest. But there is one major advantage of a CFD simulation, it is the only simulation tool, which includes the dynamic stall of an airfoil. All methods mentioned earlier require additional implementations of dynamic stall, which will increase their computational cost as well.

2.2.6 Comparison Of Models

In the previous subsections a lot of different aerodynamic models are discussed. In order to use one of them in VÆMPS it is required to evaluate them on their suitability as an aerodynamic solver or rotor optimizer. An aeroelastic solver requires a coupling between structural and aerodynamic components, logically a fast response between the models is desired. A time based simulation will require every iteration an execution of both components, which means that if one of the models requires more time, the simulation time increases as a whole. In order to prevent numerical instabilities, it might be necessary to repeat the time step.

A rotor optimizer also requires to execute the aerodynamic solver multiple times. These runs are done with different configurations, such as different airfoils, chord length, thickness or blade length. The amount of iterations increases with the amount of design variables [54], such that a fast response of the objective function is preferred.

In the Table 2.2 an overview can be found of the earlier mentioned methods. The colors indicate, whether this point is attractive (filled in green) or not (filled in red).

Table 2.2: Comparison of VAWT aerodynamic models [61]

	SST	DMST	AC	CFD	CACTUS	UMPM
Complexity	Very Simple	Simple	Moderate	Moderate	Moderate	Complex
Accuracy	Low	Low	High	Very High (DNS)	High	High
Computation Cost	Low	Low	Low	High	Moderate	High
Suitability Optimization	Less Favorable	Less Favorable	Very Favorable	Not	Favorable	With low resolution and enabled GPU
Suitability Aeroelastic	Less Favorable	Less Favorable	Favorable	Not	Favorable	With enabled GPU

The simplest model is evaluated to be the SST, based on the fact that discretization is minimized to a single tube. On the other side UMPM is seen as the most complex model, because the discretization has to be done such that the surface is impermeable. Relatively to the other models SST and DMST populates the last places in accuracy, while SST is placed a bit lower than DMST. The highest rank is occupied by the DNS variant of CFD, because it is solving the domain up to the smallest turbulence. The computational time has a shared top position, by SST, DMST and AC. The Actuator Cylinder model is capable to run 30 simulation, that have a simulated time of 150 seconds with a time step of 0.05 seconds, in about 3 hours on a 6 Core machine with 3.5 GHz and 16 GB RAM.

This aspect makes the AC very favorable as an optimization tool. It is not advised to use CFD as an optimizer or aeroelastic solver in the early design stages based, on the grounds that the computational cost will be too high and too slow. In an aeroelastic simulation it will be more wisely to use one of the modern models, which are capable of including dynamic behavior and are fast responding as well.

2.3 Structural Modeling

In the early beginnings the turbines were designed to be rigid and stiff. When the designs started to increase in size, the structural aspect becomes problematic. The gravitational loads induce a bending moment which scales with the power of four [20], which is especially important for long and heavy blades. A slender and flexible HAWT blade has the advantage that the weight and material costs are kept low. VAWTs have to catch up on the topic of structural dynamics. Based on the orientation of the blade and their rotational direction, VAWT has a probability of flutter [41], when the blades are bend outwards centrifugal forces and the relative velocity are increased leading to a change of the loads on the structure. Depending on the design, structural dynamics could be used as a passive control mechanism. DTU is focusing on a fixed blade shape [24], meanwhile SNL considers the opportunity that the blades deform such that they pitch out of the wind when the loads are too high. In order to inspect such a design it is required to have a reliable model. As in aerodynamics, the structure can also be simulated with different approaches. This section will cover the most common ones such as the Finite Element Method, Multibody Method, Modal Analysis and beam models.

2.3.1 Computational Structural Dynamics (CSD)

In CSD the structure is discretized into multiple elements, with their individual physical properties, a visualization can be found in Figure 2.12. After the structure and its elements are defined, the setup only requires a definition of the boundary conditions, such as the external loads and the fixed points of the structure. In an abstract way CSD could be seen as the CFD of the structural solvers, especially due to its high accuracy. CSD with a Finite Element method (FEM) returns the most accurate solver, but is also computational expensive and therefore not the best choice [42].

The computational power is rising, which makes CSD more favorable. For example ANSYS [3] is based on FEM and could be used as preliminary design checker with respect to static loading. But in an aeroelastic analysis, the code is operating on a time base, in which both models have to be executed each time step, meaning a CSD code might not be the best choice with respect to other engineering models.

2.3.2 Multi-Body Systems (MBS)

MBS uses multiple bodies, that are connected with each other by hinges or joints. It can be differentiated between rigid and flexible bodies. If these bodies are set to be rigid, they are not allowed to deform, such an assumption reduces the computational cost, but

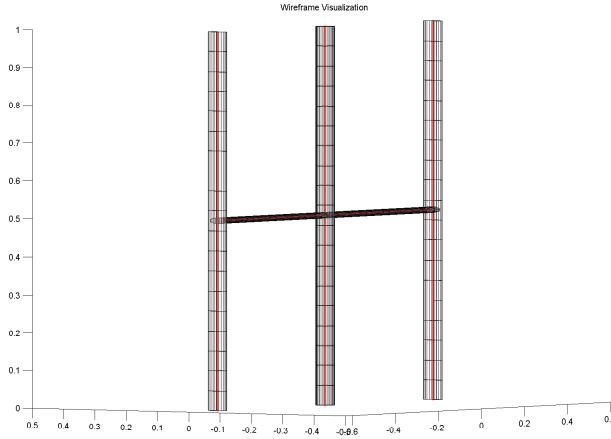


Figure 2.12: Discretization of a H-rotor VAWT

also the accuracy [48]. Figure 2.13 illustrates a MBS, where all bodies are connected via Joints and the body B_1 is defined to be the base. The degree of freedom (DoF) can be defined per body depending on the connection between the bodies. A revolute joint sets the DoF down to 1 in a three dimensional domain, and a ball joint leaves 3 DoF [56]. When every connection is defined the equation of motion can be solved. If the bodies are set to be flexible, additionally the deformations of the bodies have to be included. Due to its simplicity and adjustable degree of freedom, the computational costs can be kept low.

In this thesis *Offshore Wind Energy Numerical Simulation tool* (OWENS) is used, developed by SNL, which works with a flexible MBS and Timoschenko beams. OWENS operates on a rotating frame, having the rotational axis aligned with the tower.

2.3.3 Modal Analysis

In a modal analysis the structure is firstly analyzed on its eigenmodes, which is usually done with FEM. To capture an accurate solution, the modal analysis will require a higher order of eigenvalues. The eigenmodes are the eigenvectors of the system given in Equation (2.17), where K represents the stiffness matrix, M the mass matrix and w the reduced frequency.

$$K - w^2 M = 0 \quad (2.17)$$

The first eigenmode of a blade is usually in the flapwise direction, because this is mostly the more flexible direction. Mainly it depends on the mass and stiffness distribution of the blade design. In Figure 2.14, the eigenmodes of the Sandia 34 m Testbed can be found, which were determined by OWENS. It can be noticed that most of the modes are aligned with the rotor plane.

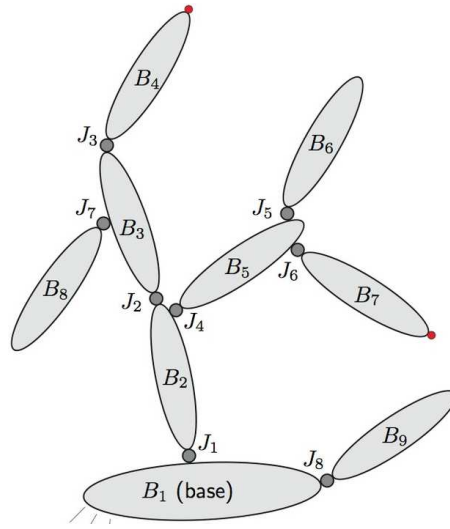


Figure 2.13: Illustrations of a Multibody System

The mentioned advantage of a modal analysis is, that after the eigenmodes are determined, every deflection of the blade can be described as a sum of those modes. Such a method requires accurate preprocessing, leading to a quick structural solver. An implementation of the modal analysis can be found in commercial codes like FAST and Bladed. Nevertheless these codes have a low accuracy as a result of the modal analysis being carried out through coarse cross-sectional property distribution along the blade [35].

2.3.4 Beam Method

In a beam analysis the structure is seen as a connection of beams, where the elastic deformation behavior is defined by the equations (2.18) till (2.21), where V is the shear force, p the distributed load, θ the slope of the beam, M the moment and ϑ the displacement of the beam. A costly integration can be avoided with the help of the conjugate beam method, simple statics calculations and the theorems, that are listed below.

$$V = \int p \, dx \quad (2.18)$$

$$\theta = \int \left(\frac{M}{EI} \right) dx \quad (2.19)$$

$$M = \int \left[\int p \, dx \right] dx \quad (2.20)$$

$$\vartheta = \int \left[\int \left(\frac{M}{EI} \right) dx \right] dx \quad (2.21)$$

Conjugate Beam Theorems [34]:

1. The slope of the given beam at any cross-section is given by the shear force at that cross-section of the conjugate beam

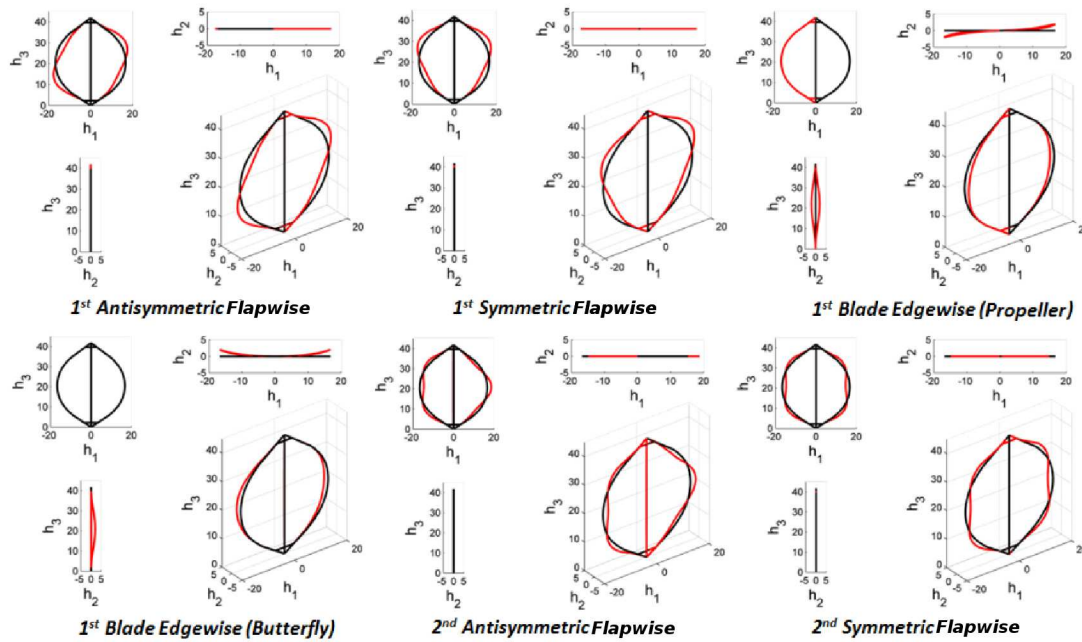


Figure 2.14: Mode shapes of SNL 34 m VAWT [53]

2. The deflection of the given beam at any point is given by the bending moment at that point of the conjugate beam

These theorems are applicable, if some constraints on the beam are changed, such that a free end has to be seen as fixed and a unsupported hinge becomes a simple support. Such an approach speeds up the calculation, resulting in less required calculations.

2.4 Numerical Aeroelastic Analysis

Aeroelasticity consists of the coupling between aerodynamic and structure. The computational aspect in combination with CFD is also known as Fluid-Structure Interaction (FSI). Figure 2.15 displays the interaction between the different fields of aeroelasticity, which are the aerodynamic, elastic and inertia forces. Two intersections are related to the topic of aeroelasticity, the static and dynamic aeroelasticity. In steady aeroelasticity only aerodynamic and elastic deformations are considered. A VAWT is operating in a rotating frame which includes inertia forces, such as gravitation and centripetal forces, additionally the turbine is vibrating and experiencing a turbulent inflow. Such influences are leading to unsteady aerodynamic and structural dynamics and therefore to dynamic aeroelasticity [28].

2.4.1 Interpolation Methods

A numerical calculation always requires a discretization of the structure, which is directly proportional to the computational time. Aerodynamics and structure are two different

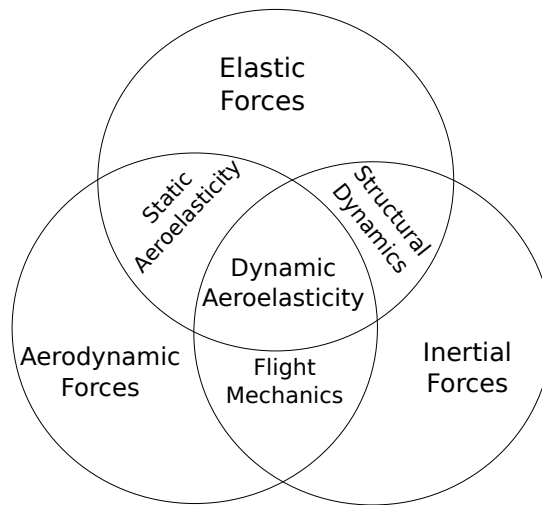


Figure 2.15: Graphical interpretation of aeroelasticity

solvers that require individual spacing to operate at an optimal level. An aerodynamic solver requires a finer grid such that it can filter up to the lowest turbulence, while the structural grid is typically more rough along the blade and becomes finer towards the root section.

Either both grids are equal down to the finest mesh or an interpolation has to be defined between both models, such that a coupling is possible. The first option includes the problems, that one solver will work with a too fine mesh and therefore requiring higher computational cost than needed. But it could also be configured such that the finer grid operates a bit more rougher mesh, resulting in truncation errors. The second option has the disadvantage that an additional calculation step is needed during the simulation. On the other hand it also allows both codes to operate on their ideal grid spacing. A short summary of interpolation methods is present below, additionally a good overview of interpolation methods can be found in [10, 49, 73].

- *Nearest Neighbor* (1st order accuracy)
The interpolation method only considers the closest points on the other grid and neglects the surrounding.
- *Gauss Interpolation* (depending on discretization)
Gauss Interpolation uses a perpendicular projection onto the other grid, which is similar to a least-squared solution were the interpolation error is minimized.
- *Radial Basis Functions (RBF)*
Takes not only the closest point into account, but also the points laying inside the radial functions. The most common ones are:
 - *Thin Plate Spline* (2nd order accuracy)
A global function that considers all points inside the radius as equal weighted. All points outside this plate are neglected.

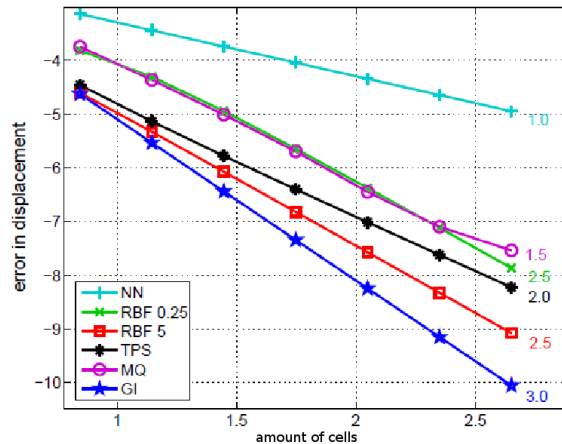


Figure 2.16: Error in displacement on a log-log plot with different interpolation schemes [70]

- *Compact Support Radius function* (depending on choice of radius, approximately 2nd order accuracy)
All points inside the radius are considered for the interpolations. The closer the points are to the coordinate, the higher the weight of the coordinates.

In Figure 2.16 the error of the interpolated displacement can be found. It becomes clear that the Gauss Interpolation (GI) has the highest order and requires less cells in order to be accurate. Most of the time FSI connections use radial basis functions (RBF) with a compact support radius [70], which keeps the computational cost low, while returning a second order interpolation and therefore a high accuracy. A one dimensional RBF will be used in this thesis, a more detailed elaboration can be found in section 3.4.

2.4.2 Coupling methods

It is also necessary to define the time advancing, with the same step size. If both models run parallel and no additional coupling-iterations are required, the coupling is known as *loose coupling* or *parallel approach* [49]. It might be still required to have sub-iterations inside the models itself. The *loose coupling* will be most effective with respect to the computational time, but this can also give probability of numerical instability. Therefore the models might need to have a stronger coupling, which can be achieved by a *partitioned solver*, known as an iteration solver [16, 57]. In the list below a small overview of different partition approaches can be found [69]. When the iterations will be executed till there is no more variation, this approach is known as quasi-monolithic [8]. This can be seen as the most accurate and expensive computational solution.

- *Serial scheme*

In the serial scheme one of the simulations is the driving factor. The leading simulation (Master) sends its data from time point n to the inferior one (Slave). Afterwards the data will be used to derive the output of time n and $n + 1$ of the subordinated simulation, will be communicated back to the superior model and integrated into the time step $n + 1$. An graphical interpretation can be found in Figure 2.17.

- *Sub-cycling scheme*

The sub-cycling scheme is in principle a modification of the serial scheme. The major difference is that it allows bigger time steps. This can be achieved by having one simulation with a larger time step, while the other uses multiple smaller steps. In this way both methods can operate with their effective time step.

- *Staggered integration*

In a staggered integration the use of the information of the structure and aerodynamic models are shifted. In other words, one of the simulations is operating in between the time steps of the other one. A schematic is given in Figure 2.18.

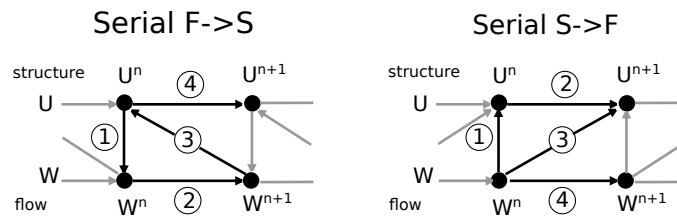


Figure 2.17: Serial time coupling [69]

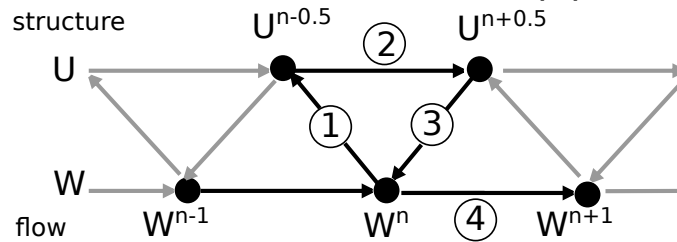


Figure 2.18: Staggered time coupling [69]

2.4.3 Commercially Available Codes

There are already aeroelastic simulation tools for HAWTs, such as FAST (Fatigue, Aerodynamics, Structure and Turbulence) and HAWC2. FAST discretizes the turbine into its components and determines their eigenmodes, which are used in the modal analysis. Currently FAST is available just for HAWTs. HAWC2 is also able to simulate the aeroelasticity of a VAWT [40] and is at the moment the only commercially available tool capable with this feature, a good example of its usage is DTUs DeepWind project.

Components Of VÆMPS

This chapter will outline the applied knowledge of each component, beginning with the structural optimization code (section 3.1). Sections 3.2 till 3.4 include all components of the aeroelastic solver VÆMPS. The chapter ends with a comparison between the commercially available HAWC2 and the self-developed VÆMPS (section 3.5).

3.1 Rotor Optimization

In order to find a fitting geometry and cross-section definition, the optimizer should fulfill the definition of Papalambros [54] and include the terms, which are described in detail in the following subsections:

3.1.1 Objective Function

The objective function determines how the design points perform. During the procedure the output of this function is wanted to be minimized/maximized. If the function can be differentiated, the optimum is just the root of the first derivative. But when the objective function is influenced by multiple factors, it is more beneficial to simplify the equation such that the objective can be computed fast.

In wind energy there are many optimization goals, most of them are aiming at the same objective: to reduce costs. In wind energy an additional objective is to raise the power output (Equation (3.3)). Cost and power output are influenced by multiple effects, such as the tower and generator. Before any torque can be transmitted to the generator, a device is needed that captures the wind energy and transforms it into aerodynamic torque. The rotor is therefore the point to focus on. An optimizer that defines structure and aerodynamic simultaneously requires a lot of computational power, time and design variables. In order to reduce computational cost and time it is decided to use a simpler approach to find a draft design, that can be improved during an iterative process. The power output can be determined with Equation (3.1), where the power coefficient is

the only variable that is directly dependent on the aerodynamic properties. In order to reduce the aerodynamic solver, the C_P and rated wind speed U can be fixed, leaving the power output only depending on one variable: the area A . The other focus of *cost* is a combination of multiple components, such as manufacturing, operation, maintenance and material. Operation and maintenance are independent of the rotor shape and will be therefore neglected. Manufacturing depends on the material and the manufacturer. The material cost appear multiple times in the cost Equation (3.2), which can be narrowed down to the mass of the rotor, leaving it as the only variable of the cost. Logically the objective function simplifies to the ratio of area and mass (Equation (3.3)).

$$P = \frac{1}{2}\rho U^3 C_P A \quad (3.1)$$

$$\text{Cost} = \text{Price} [\text{€/kg}] \cdot m + \text{Manufacture}(m) + \text{Operation} + \text{Maintenance} \quad (3.2)$$

$$\min_{\vec{x}} f(\vec{x}) = \min_{\vec{x}} \frac{\text{Cost}}{\text{Energy Output}} \equiv \min_{\vec{x}} \frac{m}{A} \quad (3.3)$$

M. Schelbergen [62] already developed a VAWT optimizer that defines a blade, which is analyzed with Nastran and evaluated on its mass. It is also used in this thesis. His code was modified such that the transition of the design elements is smoothed. The problematic will be explained in subsection 3.1.4.

3.1.2 Design Variables

During the optimization process the design variables are the parameters that can be differed. More evaluations have to be made, if the amount of variables is increased [39]. A numerical optimization requires the VAWT to be discretized as seen in Figure 3.1. In order to reduce the amount of variables the blade will be divided into multiple sections and the airfoil is built-up from three components: skin, girder and shear web (shown in Figure 3.1b).

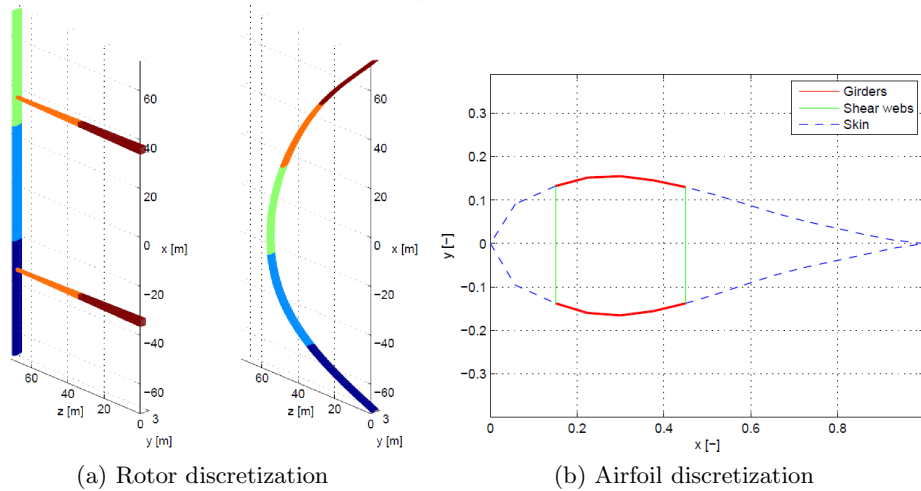


Figure 3.1: Discretization of the VAWT rotor [62]

With this discretization it is possible to define the design vector. Figure 3.2 displays the decoded vector, where every element of the vector represents either a thickness or a control point. The later part of the design vector is occupied by the thickness of the strut elements, which is only existent in an *H-rotor*. The end of the design vector is assigned to the sampling points, that describe the topology of the rotor. However, this setup is limited to one airfoil and a constant chord length.

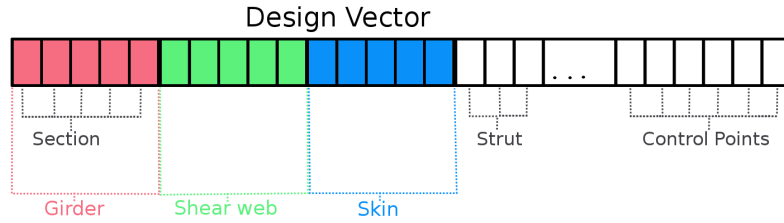


Figure 3.2: Design vector of discretized rotor

3.1.3 Constraints

The definition of Papalambros [54] mentioned that an optimization has to have constraints, such that the optimization is physically feasible. Such constraints can focus on the structure or to reduce the design domain. This thesis uses two major constraints, which will be explained in the following lines.

Safety Constraint

It is not wanted that the turbine breaks. Therefore it is necessary to determine whether the stress of each element is below the ultimate one. A safety factor of 1.5 is included at ultimate loading and 1.2 at buckling. The Kassapoglou Maximum Stress Failure theory is used [36] in order to evaluate the condition of the element. He defines the maximum stress failure factor (*MSFT*) as the fraction of the actual stress $\sigma_{1,2}$, the safety factor *SF* of the structure and the maximum allowable stress (Equation (3.4)), which is given in Table 3.1. The stress itself was determined by Nastran and is returned in its output file.

$$MSFT = \left| \frac{\sigma_{1,2} \cdot SF}{\sigma_{ult}} \right| \quad (3.4)$$

$$\sigma = \frac{F}{A} \quad (3.5)$$

Determining the stress failure factor is not sufficient for the use as a constraint. In the function `fmincon` in Matlab the constraints need to be defined such that the values are smaller or equal to zero. The *MSFT* will be subtracted by minus one, which will result in the fact that when the stress failure indicates a broken element the constrain value becomes greater than zero.

$$C_{neq} \leq \max(MSFT) - 1 \leq 0 \quad (3.6)$$

Table 3.1: Material properties [14]

Material	Unit	CFRP UD	GFRP UD
Density	[kg/m ³]	1.57e3	1.7e3
Young's Modulus	[GPa]	139.5	47.7
Ult. tension stress (0°)	[MPa]	1.95e3	1.71e3
Ult. compression stress (0°)	[MPa]	1.55e3	1.14e3
Ult. tension stress (90°)	[MPa]	46.4	62.05
Ult. compression stress (90°)	[MPa]	250	155

In addition to the actual stress constrain, another failure possibility is considered: fatigue. The fatigue damage D is determined through Miner's rule [47], the product of the safety factor SF and the sum of the appearing cycles n and the allowable cycles of the material N_{allow} (Equation (3.7)). A D greater of equal to 1.0 represents a failure.

$$D = SF \cdot \sum_i \frac{n_i}{N_{allow,i}} \quad (3.7)$$

The allowable number of cycles is determined with the relation of Poursartip et al. [60], presented in Equation (3.8). The maximum allowable load is denoted by σ_{ult} , $\Delta\sigma$ is the difference between maximum and minimum stress. R_σ is the stress ratio between minimum and maximum stress which are obtained at the different loading conditions (parked, up- and downwind) and collected with a Rainflow counting. The exponent p is assumed to be 1.6 for high stress ratios as recommended by M. Schelbergen [62].

$$N_{allow} = 3.108 \cdot 10^4 \left(\frac{\Delta\sigma}{\sigma_{ult}} \right)^{-6.393} \left(1.222 \frac{1 - R_\sigma}{1 + R_\sigma} \right)^p \left(1 - \frac{\Delta\sigma}{(1 - R_\sigma) \sigma_{ult}} \right) \quad (3.8)$$

with

$$R_\sigma = \frac{\sigma_{min}}{\sigma_{max}} \quad (3.9)$$

The number of cycles n is the product of the rotational speed ω and the operational time T (Equation (3.10)). The operational time is described through the product of the life time and the percentage at which the turbine is at the rated speed Ξ , assumed to be 35% [68].

$$n = \omega \cdot T \quad (3.10)$$

$$T = \text{Life time} \cdot \Xi \quad (3.11)$$

Area Constrain

If the swept area would be unlimited it might be that the output of the optimization will not be physical feasible. Therefore it was decided to limited the area which was predetermined by the factor of 1.0 and 1.3 as lower and upper constraint. Following from that the rotor area is only allowed to enlarge.

Boundaries

The design space can be limited by bounding the design variables, such that restrictions of manufacturers are represented. It has to be differentiated between constraints and boundaries. A constraint is with respect to the objective function values, while a boundary is limiting the design variables. Table 3.2 shows the boundaries of the panel thickness.

Table 3.2: Boundaries of design variables

Variable	Lower Bound	Upper Bound
R [m]	3.5	350.0
Thickness [mm]	5	150

3.1.4 Optimization Procedure

In section 2.1 different optimizations were discussed. The optimizer of M. Schelbergen [62] is based on `fmincon`, which can be configured to use the CGB method. Aside from the optimization algorithm itself, it is also important to define the procedure of the optimization displayed in Figure 3.3. Some slight modifications have been made to the original codes, in order to create a function evaluation which is more physical representative. The modifications are stated below and marked in grey in Figure 3.3.

Mass Determination

Originally the mass was determined by a summation of each section. This assumption implies that the thickness of the shell of the blade is constant along a section. In HAWTs the shell is decreasing continuously towards the tip [67]. Therefore the mass and thickness will be interpolated along the VAWT blade span. Three options of interpolation have been investigated, which are listed below.

- *Linear interpolation*

A straight line between the thicknesses at the beginning of the sections. It is not known, whether the thicknesses at the end of the blade are equal to the earlier determined trend, therefore it was decided that the thickness is kept constant along the last section.

$$y = y_i + (y_{i+1} - y_i) \frac{x - x_i}{x_{i+1} - x_i} \quad (3.12)$$

- *Cubic spline interpolation*

This interpolation requires a set of predefined points, where the curve has to pass through. In the thesis it is decided that the points are the beginning/end of the blade and the middle of the enclosed sections. The interpolation is determining a piece wise third order polynomial, which crosses those points, while the curvature is kept continuous [4]:

$$f'_i(x_i) = f'_{i+1}(x_i) \quad (3.13)$$

$$f''_i(x_i) = f''_{i+1}(x_i) \quad (3.14)$$

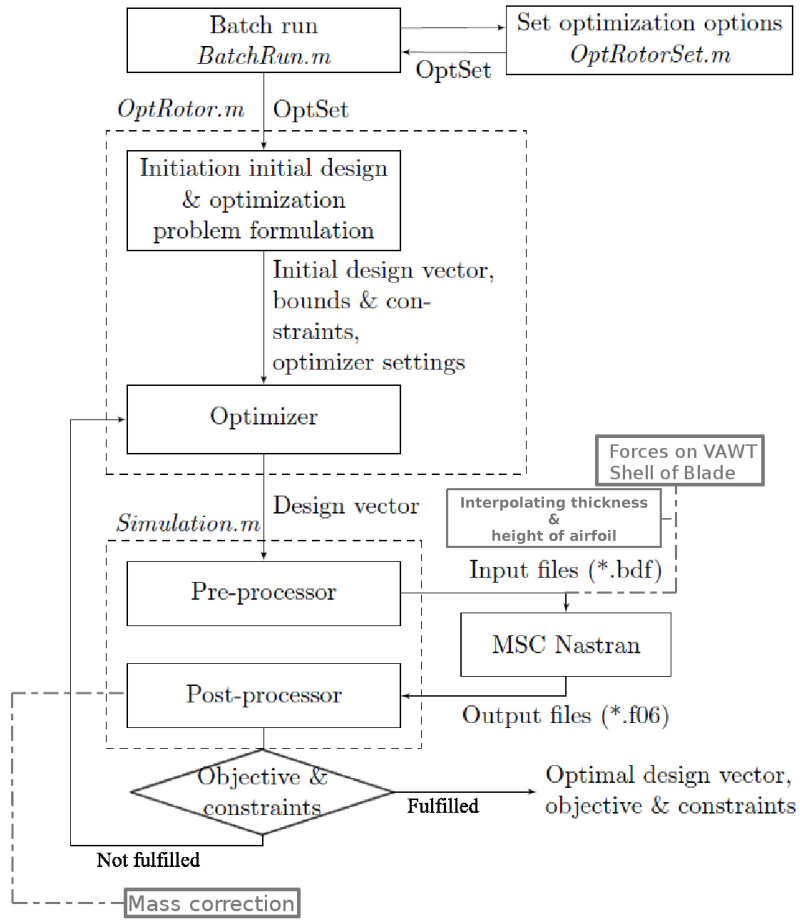


Figure 3.3: Flow diagram of the optimization process [62]

- *Weighted polynomial interpolation*

A simple polynomial interpolation uses a least-squared approach to find the coefficients of the polynomial. The only difference in this case is that the function values y will be multiplied with a weighted matrix W and the coefficient matrix M . A weighted fitting can ensure that certain points will be definitely crossed [7]:

$$p = (M'(W M))^{-1} M' (W y) \quad (3.15)$$

$$\text{with} \quad (3.16)$$

$$M_{ij} = x_i^j \quad (3.17)$$

Figure 3.4 shows the mass distribution along the blade with respect to a test case of stairs and actual distribution of the shear web mass. It becomes clear that depending on the distribution the three interpolation schemes, perform differently. In the case of a descending stair, such as in Figure 3.4a, the spline and weighted polynomial are almost similar. Only a small difference around the end points can be found, where both interpolation schemes are laying next to each other. The linear interpolation is always beneath the real

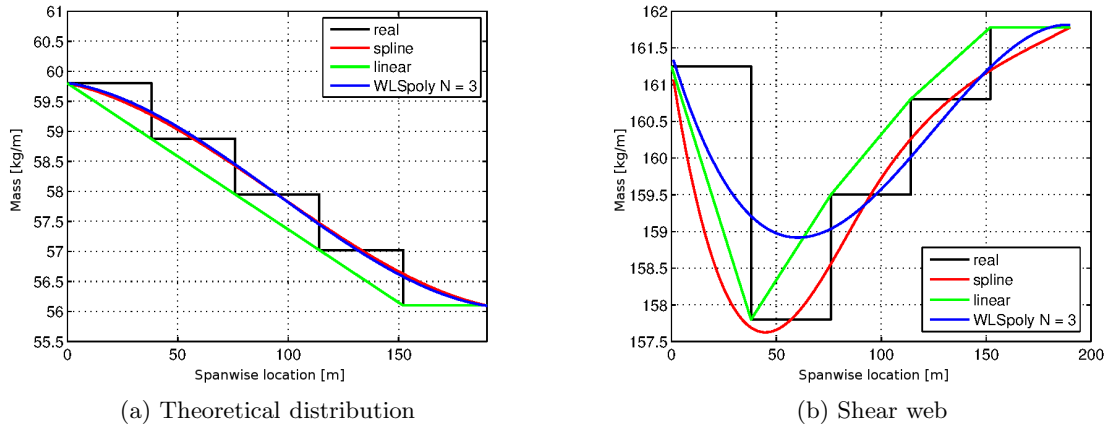


Figure 3.4: Weight distribution along a VAWT blade span

curve, which will result in a lower weight and in the greatest offset.

While inspecting Figure 3.4b, the differences and advantages of the schemes become more obvious. The weighted polynomial does not meet all values of the mass distribution and therefore introduces an offset. If this method is used to interpolate the thickness along the blade, the Nastran input file will contain not representative thicknesses, which were determined during the optimization, but instead a smooth approximation is considered. The linear interpolation approaches the values directly, while having a non-differentiable curve, introducing stress concentrations at these points. The spline interpolation crosses through the defined middle points and the blade end points. However, it also overshoots the determined values around the first step. Such an overshoot could introduce weakness in the structure, especially if the spline determines lower thicknesses than wanted, which could lead to higher stresses on the structure and therefore to failure indications. In subsection 3.1.5, a comparison of the different interpolation schemes is done with respect to their optimization output.

Changing Airfoil Thickness

The optimizer of M. Schelbergen [62] was based on a constant blade section. Either the chord was equal to a predefined value or was determined as a factor of the equatorial blade radius. Through a fixed chord and a single airfoil, leads to a constant thickness. Such a fixed thickness might be less efficient in a Troposkein design, as the root requires more reinforcement than the equatorial region. Thick airfoils have the benefit of including a high structural integrity. However, at high angles of attack the drag is a major drawback. Therefore it was decided to vary the airfoil along the blade depending on its inclination angle. If the airfoil is aligned with the rotational plane, the vertical velocity component is almost zero. This leads to low angle of attack and to low amount of drag. Nonetheless, in the region where the local TSR is below 1.0 the drag of the thick airfoils is an advantage as it can be used in a drag-driven configuration. The function, displayed in Equation (3.18), scales the cross-section from a thick one at the root towards a thin one at the equator.

Through this a thin airfoil with low mass and less drag can be included into the design.

$$Z(\beta) = 1 + (Z_{max} - 1)(1 - \sin \beta) \quad (3.18)$$

The scaling factor is denoted by Z . Z_{max} is the maximum scaling factor that is desired at the root. This equation only depends on the location of the airfoil, measured through the inclination angle β . Figure 3.5 shows how β is determined, 0° is aligned with the top of the blade and 90° with equatorial region. With this relation it is possible to have an alternating blade without introducing any new design variables, that will raise the computational time.

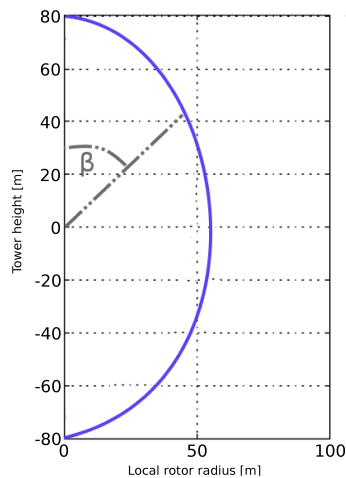


Figure 3.5: Definition of inclination angle, along a Darrieus turbine

Loads On A VAWT

A VAWT blade experiences multiple loading conditions, which are mentioned below. The first two are obtained through the mass of the blade. The other two forces are based purely on the aerodynamics.

- Parked condition
- Centrifugal force
- Maximum load on upwind position
- Minimum load on downwind position

During operation all of these forces act on the blade. But if the turbine is parked, the only force acting on the turbine is the gravitational load. Especially in a Darrieus configuration parking is a critical issue, because at that point the entire weight of the rotor is applied to the root section, as seen in Figure 3.6. During the optimization all four cases will be applied on the evaluation point, such that a design can be found, which sustains operation and parking.

The centrifugal force and also the aerodynamic forces are dependent on conditions obtained while being in operation. From Figure 3.7a it can be observed that the turbine would have its optimum at a TSR of 7 and a solidity of 0.065. This will only be true if

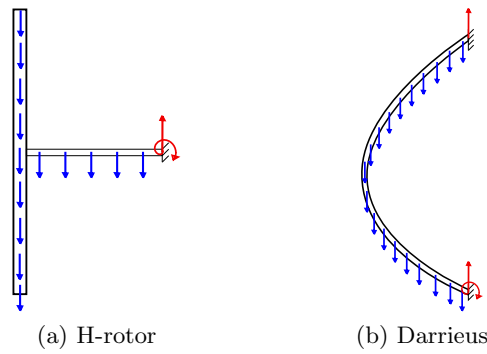


Figure 3.6: Gravitational loads on a VAWT

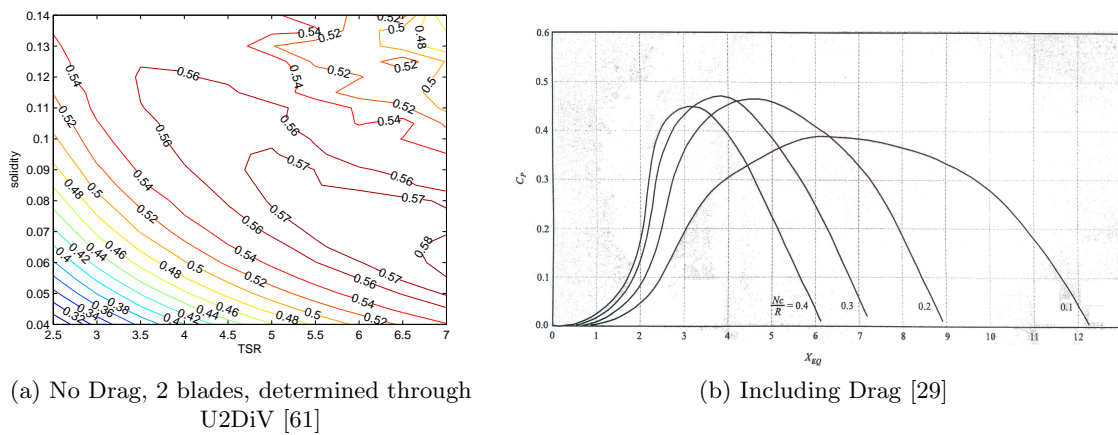


Figure 3.7: Power coefficient contour at various TSR and σ , with a NACA 0015

the airfoil does not produce drag. So it was decided to use Figure 3.7b instead, than a two bladed machine will have a C_P of 0.45 at a TSR of 4.5 and a solidity of 0.2, leading to a chord to radius ratio of 0.1.

The aerodynamic loads have been simulated through stiff blades and are displayed in Figure 3.8. The maximum loads out of the plots can also be found in Table 3.3. It can be noticed that both curve agree quite nicely especially in the upwind region ($0-180^\circ$). A significant difference is a phase shift of almost 10° . Nonetheless the optimization code only considers the load and not its position, which makes the phase shift insignificant.

Table 3.3: Aerodynamic loads during optimization

Case	Unit	HAWC2	U2DiV
Max. upwind force coefficient	[-]	46.873	46.409
Min. downwind force coefficient	[-]	-11.202	-9.560

In addition to the aerodynamic force pointing out of the rotational plane, the loading will be increased by the reaction force of the centrifugal force. Equation (3.19) indicates that a higher mass will lead to a higher centrifugal force. An elastic deformation of the blade will also lead to a change of this loading, in order to account for this behavior a dynamic

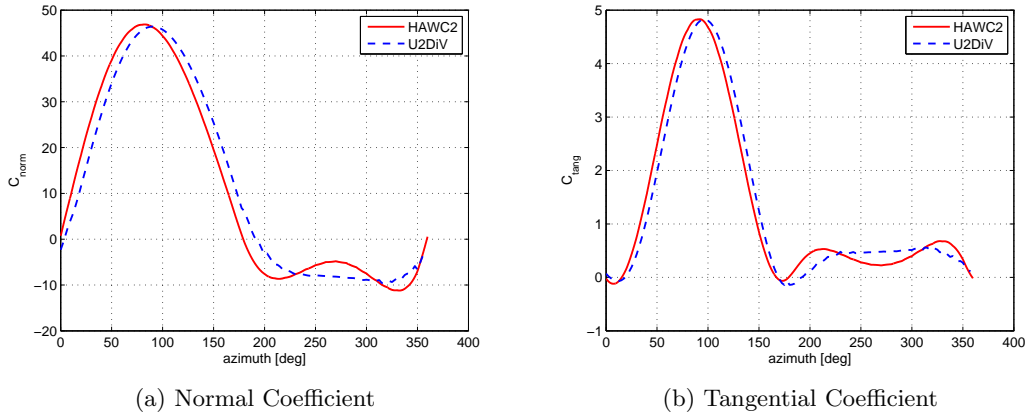


Figure 3.8: Normal and tangential force on two bladed VAWT

structural solver would be required. But it is wanted to keep the optimization simple, which means that the centrifugal loading is assumed to be constant at a given rotational speed.

$$F = mR\omega^2 = mR \left(\frac{\lambda U}{R} \right)^2 = m \frac{(\lambda U)^2}{R} \quad (3.19)$$

3.1.5 Determining The Interpolation

As mentioned above, the optimization code includes 4 methods on how the weight and thickness is determined along the blade span. This is achieved by either the original step function, a linear fitting, a weighted polynomial or a cubic spline, with the sampling points at the middle of the section. Before the main optimization has been executed, it was inspected which of these methods, returns the best result. The evaluation was done on a 5 MW Darrieus shaped VAWT, similar to the one mentioned in section 3.1.6. The airfoil profile was capped to a NACA0015 and the initial thicknesses, proposed by M. Schelbergen [62] were used (Figure 3.9). All optimizations started from the same point and their output can be found in Table 3.4.

Table 3.4: Comparison of the interpolation methods

Method	Step function	Linear trend	Weighted polynomial	Cubic spline
Function value (m/A)	5.87	6.15	5.85	5.14
Mass [kg]	34.16e+3	35.82e+3	34.04e+3	29.96e+3
Constraint violation [-]	1.06e-1	6.55e-3	5.22e-3	1.05e-1
Computational time [h] ¹	17.65	29.12	25.64	27.01

¹Measured on a 6 core 3.5 GHz machine with 64 bit-Windows 7 and 16 GB RAM and a Msc Nastran student license limited to 5000 Nodes.

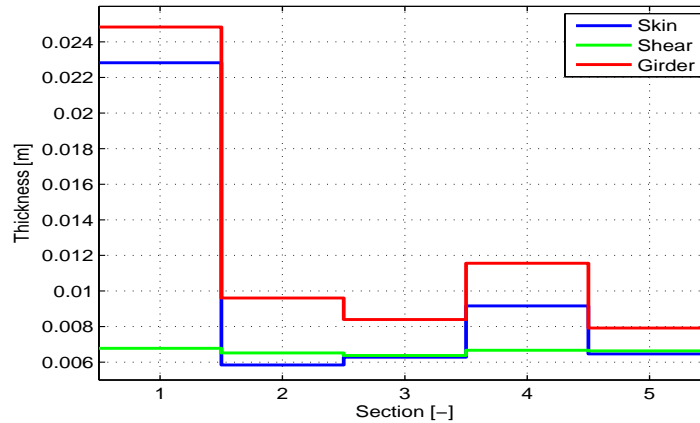


Figure 3.9: Initial thickness of a Darrieus 5MW

It can be noticed that all four methods violate the constraints. It was determined that the buckling constraints are violated, which means that the buckling safety factor of 1.2 was exceeded. This is not preferred but was already pointed out in M. Schelbergen [62] thesis. Nevertheless the violation do appear less while using another initial thickness. The weighted polynomial seems to be the best choice with respect to these violation. But the reduction in weight is not as sufficient as with the cubic spline. With the help of this interpolation method, the mass can be reduced up to 12.2% with respect to the initial case of the step function. The constrain violation is about 0.1 which is still acceptable and only has to be kept in mind. Additionally, it can be seen that with an interpolation of the wall thickness, the computational time is increased independently of the chosen method. Based on this results it was decided to the cubic spline in the further procedure.

3.1.6 Starting Points Of Optimization

It was decided to use the power coefficient proposed by I. Paraschivoiu [29], shown in Figure 3.7b. In the graph it can be extracted that with a two bladed machine and a chord to radius ratio of 0.1, the power coefficient is going to be 0.45. The C_P at the solidity of 0.3 is a bit higher, but would also mean a bigger chord to radius ratio, leading to bigger blades and therefore to more material. The difference between power outcome is not significantly enough to justify the increasing cost and was for this reason neglected.

Through out this thesis the effect of different airfoil shapes and their influence on the structural perspective is inspected. So the used profiles are standard NACA 4-digit ones located on a 5 MW, two bladed Troposkein shaped turbine at rated speed of 12 m/s, a tip speed ratio of 4.5, a chord to radius ratio of 0.1 and an assumed power coefficient of 0.45. These values will lead an area of $1.633 \cdot 10^4 \text{ m}^2$. A summation of this data can also be found in Table 3.5.

As mentioned earlier the design vector contains two parts. The first part represents the thickness of the different elements at the sections. In order to start from a save point, it was decided to a thickness of 25 mm along the entire blade. With this point it was

Table 3.5: Optimization starting point of inspected blade profiles

Variable	Unit	Value
Density	[kg/m ³]	1.225
Rated wind speed	[m/s]	12
Power coefficient C_P	[-]	0.45
Chord to Radius	[-]	0.1
Tip Speed Ratio	[-]	4.5
Power output	[MW]	5
Area	[m ²]	1.633e+04
Height	[m]	180
# of sections	[-]	5

Table 3.6: Initial control points of inspected blade profiles

#	X-position	Z-position
1	0.00	-90.00
2	19.34	-81.00
3	29.27	-66.67
4	40.29	-39.60
5	51.62	0.00
6	39.39	39.60
7	19.04	66.67
8	5.65	81.00
9	0.00	90.00

ensured that the optimizer will find a suitable point, by just reducing the amount of material. The second part of the design vector is occupied by the control points, that determine the optimal shape of the Darrieus. During the procedure the optimizer will move those points and thereby increasing/decreasing the area. The initial coordinates can be found in Table 3.6.

After the starting point and interpolation method are set, it is possible to decided which cases are executed. In order to inspect the influence of different airfoil designs, the optimization was done with the NACA 0015, 0018, 0020, 0025, 0030, 0035, 0015-35, 0018-35 and 0015-40. The usual notation of the NACA 4-digits symbolizes that the airfoil has been used constantly along the entire span. The additional numbers in the 4-digit code can be seen as an abbreviation of a design, where the airfoil varies from a thick NACA at the root section to a thin NACA at the equator. The 0015-35 represents the change from a NACA 0035 to a 0015, the 0018-35 from a 0035 to a 0018 and 0015-40 from 0040 to 0015. Additionally, the cases were done with two different materials: GFRP and CFRP. The optimization points and their initial function value (m/A) can be found in Table 3.7.

Table 3.7: Initial function values of inspected blade profiles

	CFRP	GFRP
NACA 0015	6.27	6.78
NACA 0018	6.41	6.93
NACA 0020	6.51	7.03
NACA 0025	6.76	7.30
NACA 0030	7.02	7.58
NACA 0035	7.29	7.87
NACA 0015-35	6.69	7.23
NACA 0018-35	6.78	7.32
NACA 0015-40	6.80	7.35

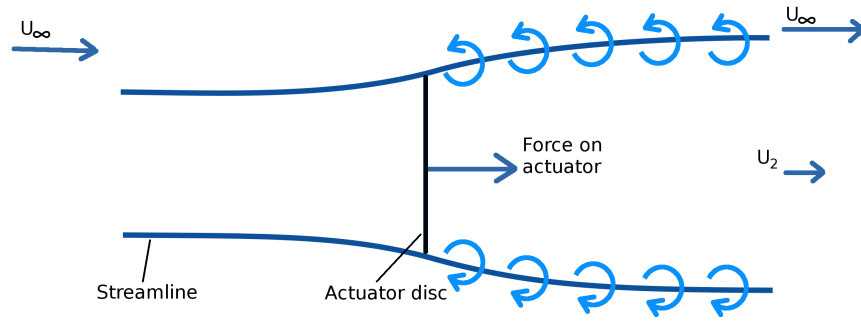


Figure 3.10: Schematic of shed vortex along streamlines

3.2 Aerodynamic Modeling Of A VAWT By UMPM

As mentioned VÆMPS uses a vortex panel code, to simulate the aerodynamics of a VAWT. The following section will elaborate on the underlying methodology and its implementation.

3.2.1 Energy Extraction

From HAWT, the stream tube theory is already known, based on the conservation of mass (Equation (3.21)) and momentum (Equation (3.22)). So the mass flow (Equation (3.20)) in has to be equal to the mass flow out (Figure 3.10). The fluid is assumed to be incompressible. This results in the fact that if energy is extracted, the velocity is reduced and leading the variation of the stream tube cross-section. The inside of the stream tube is changed, while the outer surrounding is unchanged. The transition between those layers is a change of enthalpy, which is aligned with the streamline [37]. This change is obtained through the shed vortex wake. In Equation (3.23) it can be seen that a vortex is shed if there is change in forces. Along a HAWT blade the forces are continuous. At the tip the forces drop sudden and shed the strongest vortex.

$$\dot{m} = \rho \mathbf{v} A \quad (3.20)$$

$$\frac{\delta \rho}{\delta t} + \nabla \cdot (\rho \mathbf{v}) = 0 \quad (3.21)$$

$$\frac{\delta}{\delta t}(\rho \mathbf{v}) + \nabla \cdot (\rho \mathbf{v} \mathbf{v}) + \mathbf{Q} = 0 \quad (3.22)$$

$$\frac{D\omega}{Dt} = \frac{\delta \omega}{\delta t} + \vec{v} \cdot \nabla \omega = \omega \cdot \nabla \vec{v} + \nu \nabla^2 \omega + \nabla \times \vec{f} \quad (3.23)$$

VAWTs also sheds a vortex in the tip region. Another principle can be applied too. The loads on the blade is also changing during each revolution because of the rotation of the turbine. In Figure 3.11 it can be seen that on the upwind part the forces point out of the rotational plane, while on the downwind side the forces point inwards. As it can be noticed at the upper and lower part, there is a change in the force direction, which will shed a wake. This jump in force can be explained through the fact that at this point the gradient

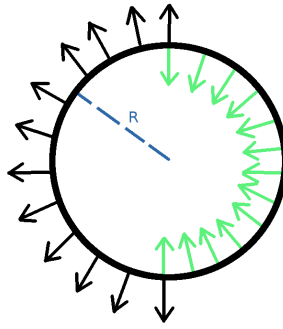


Figure 3.11: Force distribution along a VAWT with pure rotation

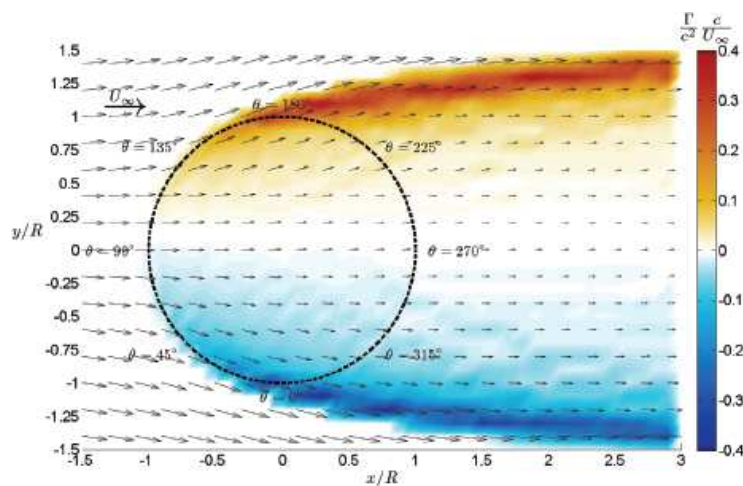


Figure 3.12: Time averaged circulation on a VAWT (top view) [17]

of the angle of attack is the highest as seen in Figure 3.14a. According to Kelvin's theorem the change of circulation in time has to be zero inside the domain (Equation (3.24) [37]). Following from that it can be stated that when the angle of attack is varied, the vortex strength is changing and shedding a counter vortex behind the trailing edge as seen in Figure 2.8. During operations the angle of attack has the highest gradient at an azimuth angle of 0° and 180° . Therefore it can be stated that a VAWT is shedding a vortex in space and in time [17]. The shed vortex, created in time, also creates a stream tube similar to the one of a HAWT.

$$\frac{D\Gamma}{Dt} = 0 \quad (3.24)$$

This could give the impression that the normal stream tube theory might be a valid approach for a VAWT, but as discussed earlier, the DMST has multiple factors which make the theory only applicable as a poor estimation, especially due to the fact that pitching of the blade is not considered as well as no differentiation between up- and downwind.

3.2.2 Inflow Behavior

Aerodynamic forces can be determined when knowing the angle of attack and the perceived velocity V_{rel} . The VAWT is operating on a rotating frame, resulting in a changing inflow condition. In Figure 3.13a it can be seen that the undisturbed wind speed U will be divided into a radial and a tangential component, which is dependent of the azimuth angle Ψ . Also the rotational velocity ω times the radius R will be added to the tangential component. These velocity components will be summed together with the induced velocity of the wake, resulting in the perceived velocity (Equation (3.27)). Together with the orientation of the chord line, it is possible to determine the angle of attack (Equation (3.25)). Due to the curved flow, every location along the airfoil will experience another angle of attack, which can be determine with Equation (3.25).

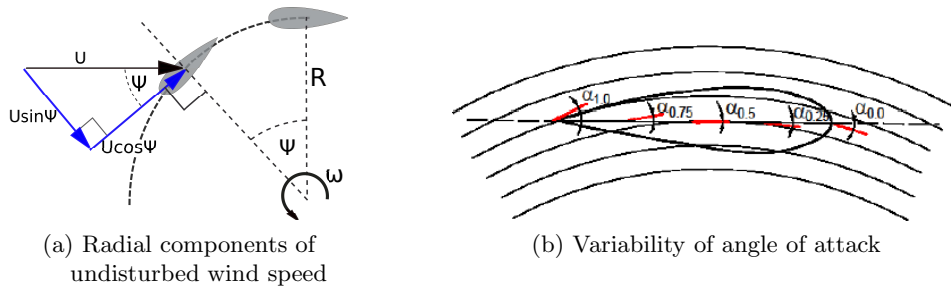


Figure 3.13: Inflow condition in a rotating frame

$$\alpha = \arctan \frac{V_{ind,norm} + U \sin \Psi}{V_{ind,tang} + \omega R + U \cos \Psi} \quad (3.25)$$

$$\alpha = \arctan \frac{\frac{V_{ind,norm}}{U} + \sin \Psi}{\frac{V_{ind,tang}}{U} + \lambda + \cos \Psi} \quad (3.26)$$

$$V_{rel} = \sqrt{(V_{ind,norm} + U \sin \Psi)^2 + (V_{ind,tang} + \omega R + U \cos \Psi)^2} \quad (3.27)$$

$$V_{rel,noinduction} = U \sqrt{\lambda^2 + 2\lambda \cos \Psi + 1} \quad (3.28)$$

To make the equation independent of the rotational speed, the TSR λ is introduced. The TSR is defined as a ratio of rotational velocity times the radius and the undisturbed speed. It can be noticed that if the induced velocities are neglected, the equations simplify to (3.26) and (3.28). A difference can be observed in Figure 3.14. The relative velocity is mainly effected at the downwind site. But the angle attack is effected along the entire rotation. During the upwind phase the geometric approach is overshooting the results, while underestimating the angle downwind. It can be concluded that such a simple approach should be avoided at all cost.

These difference are an indication of the shed wake. As mentioned earlier, every time the angle of attack is varied a counter vortex is created to satisfy Kelvins theorem. Along the entire revolution a small amount of vorticity is created and the strongest ones at 0° and 180° . This shed vortex is going to intersect with the blades on the downwind side,

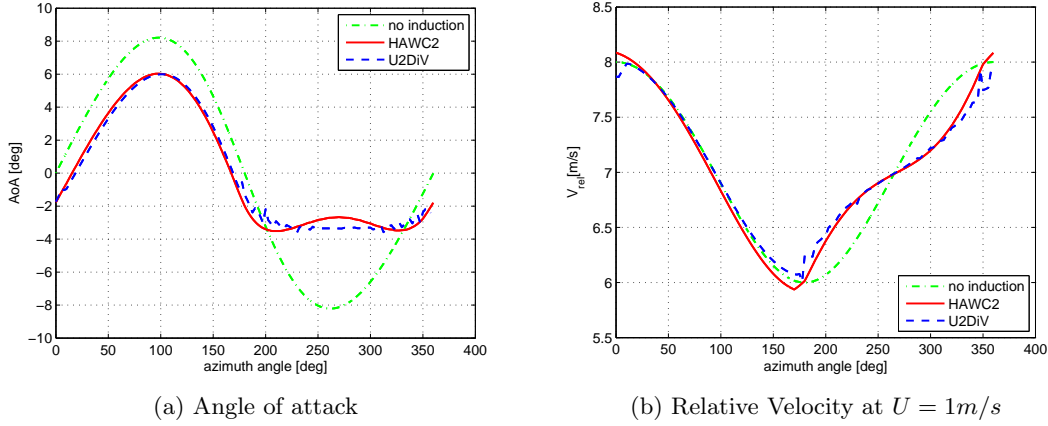


Figure 3.14: Time averaged inflow conditions at $\lambda = 7$ and $\sigma = 0.065$

which will be increasing the angle of attack. Instead of receiving high negative angle of attack the blades will have a plateau of a small negative angle. In Figure 3.14b it can be recognized that at 0° and 180° there is jump in the relative velocity, exactly where the wake is going to be shed. Also the downwind side experiences a relative wind speed that is opposite to the predicted one, because of the earlier shed wake and the alternation of the induced velocity. Between 180° and 270° the induced velocity is acting against the wind speed and therefore increasing the velocity on the airfoil. Along the last quadrant the induced velocity acts against the moving direction and slowing perceived wind speed down. Additionally, the wake-wake interaction will change the inflow along the azimuth angles. During the initialization of the problem the effect of the wake will not be noticeable, because it requires time to develop.

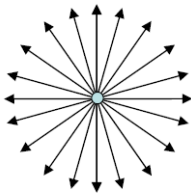
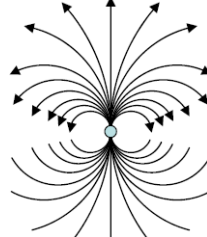
These induced velocities can be determined through the potential and velocities with help of the Laplace equation (Equation (3.29) and (3.30)). It is possible to superimpose any arbitrary geometry into multiple fundamental solutions. The flow should not be assumed as inviscid. This would produce a frictionless flow, leading to an irrotational flow. Such an assumption is not capable of producing physical results for VAWTs [15].

$$q = \nabla\Phi \quad (3.29)$$

$$\nabla^2\Phi = 0 \quad (3.30)$$

A method to model a rotational flow is to use vorticity, which is defined as the curl of the velocity (Equation (3.31)). The vorticity allows to obtain an ideal fluid, while it still influences the velocity field inside the domain. This quantity can be correlated with the circulation Γ through *Stokes' theorem*, where the vorticity is related by the flux normal to the surface of the domain (Equation (3.32)). This circulation can be used to determine the lift that is described through the Kutta-Joukowski (Equation (2.14)).

Table 3.8: Fluid point overview [37]

	Source	Doublet
Strength sign	σ	μ
Velocity potential Ψ	$-\frac{\sigma}{4\pi r}$	$-\frac{\mu \cdot r}{4\pi r^3}$
Velocity $q(r, \theta, \phi)$	$(\frac{\sigma}{4\pi r^2}, 0, 0)$	$(\frac{\mu \cos \theta}{2\pi r^3}, \frac{\mu \sin \theta}{4\pi r^3})$
Graphical interpretation		

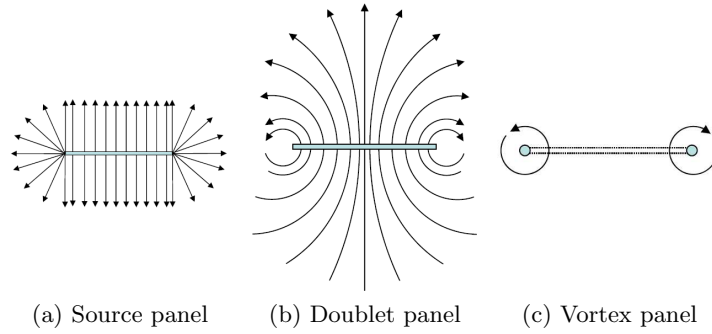


Figure 3.15: Singularity panel representation with velocity representation

$$\zeta = \nabla \times \vec{V} \tag{3.31}$$

$$\Gamma = \int_S \zeta \cdot n \, dS \tag{3.32}$$

As mentioned, it is possible to divide any given geometry as a combination of multiple fundamental relations. Such fundamentals can be expressed as a source or doublet point, which will effect the flow around its environment. An overview about those singularities can be found in the Table 3.8.

Another singularity option is a vortex, where the flow is rotating around an origin. Its local vorticity can be used to define a *vortex line*, where the cross-product of vorticity and its path is equal to zero (Equation (3.33)). The *vortex line* forms a *vortex sheet*, if it passes through an open curve in space. If the curve is closed it will form a *vortex tube*. A reduction of this curve into a simple point, will also lead to a reduction of the tube into a *vortex filament* [15].

$$\zeta \times ds = 0 \tag{3.33}$$

A singularity panel can be represented with all three point singularities, as seen in Figure 3.15. Only the vortex allows a rotational flow. The vortex ring panel is similar to the

Doublet panel. This equivalence is a great advantage with respect to the implementation, because it allows to discretize the geometry by constant doublet panels and therefore reducing the computational cost [15]. Hess [26] states that in order to have a complete equivalence it is necessary that the derivative of the doublet strength distribution μ is equal to the vortex strength.

3.2.3 Aerodynamic Forces

The aerodynamic model is used to determine the forces along the blade inside the aeroelastic tool. The basic equations (3.36)-(3.38) can be used to determine lift, drag and aerodynamic moment. While determining the perceived velocity, all components shown in Figure 3.16 have to be included in order to be accurate. Most of these components are determined in the aerodynamic solver. Only the heaving in flapwise direction $\dot{\zeta}$ and the translation motion in edgewise direction $\dot{\eta}$ are obtained by the structural solver. Additionally, it can be noticed that a motion in normal direction will result in a change of the tangential velocity, due to the fact that the rotational velocity is a product of the angular velocity and radius, which gives opportunities to unsteady aerodynamics.

$$V_{per}^2 = (\omega R + U \cos \Phi + V_{ind,tang} + \dot{\zeta})^2 + (U \sin \Phi + V_{ind,norm} + \dot{\eta})^2 \quad (3.34)$$

$$q = \frac{1}{2} \rho V_{per}^2 \quad (3.35)$$

$$L = q S C_l(\alpha) c \quad (3.36)$$

$$D = q S C_d(\alpha) c \quad (3.37)$$

$$M_{AC} = q S C_{mAC}(\alpha) c \quad (3.38)$$

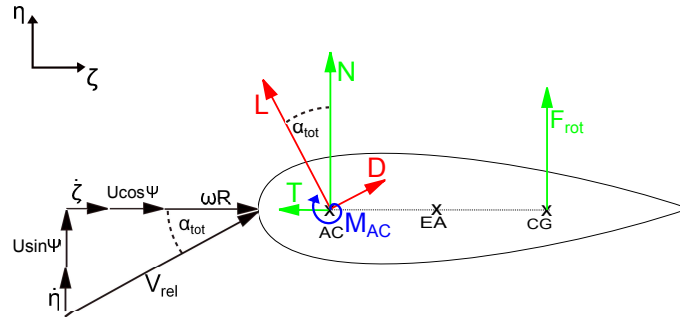


Figure 3.16: 2D forces on VAWT blade during operations

Lift always acts perpendicular to the velocity and drag parallel. Therefore it is necessary to transform the forces into the cylindrical coordinates such that the deflections in radial and tangential directions can be determined. This is done through the angle of attack and the pitch angle. These angles are also related to the motion of the structure, leading to the fact that during the evaluations of the angle of attack, these motions have to be included. Therefore the overall angle is determined out of the sum of all influences

(Equation (3.39)).

$$\alpha_{tot} = \alpha + \theta + \Delta\alpha_{\dot{\eta}} + \alpha_{\dot{\zeta}} \quad (3.39)$$

$$\alpha_{\dot{\eta}} = \arctan \frac{U \sin \Psi + \dot{\eta}}{\omega R + U \cos \Psi} - \alpha \quad (3.40)$$

$$\alpha_{\dot{\zeta}} = \arctan \frac{U \sin \Psi}{\omega R + U \cos \Psi + \dot{\zeta}} - \alpha \quad (3.41)$$

After the transformation angle is determined, it is possible to determine the normal and tangential force. In the derivation a small angle assumption was used to simplify the angle variation obtained through structural dynamics, which resulted in the equations (3.44) and (3.45). A full derivation can be found in appendix A.

$$N = L \cos(\alpha_{tot}) + D \sin(\alpha_{tot}) \quad (3.42)$$

$$N = L \cos(\alpha + \theta + \Delta\alpha_{\dot{\eta}} + \alpha_{\dot{\zeta}}) + D \sin(\alpha + \theta + \Delta\alpha_{\dot{\eta}} + \alpha_{\dot{\zeta}}) \quad (3.43)$$

$$T = L \sin(\alpha_{tot}) - D \cos(\alpha_{tot}) \quad (3.43)$$

$$T = L \sin(\alpha + \theta + \Delta\alpha_{\dot{\eta}} + \alpha_{\dot{\zeta}}) - D \cos(\alpha + \theta + \Delta\alpha_{\dot{\eta}} + \alpha_{\dot{\zeta}})$$

$$\begin{aligned} N = L & \left[\theta \left(s(\alpha_0)(-1 + \Delta\alpha_{\dot{\zeta}}\Delta\alpha_{\dot{\eta}}) - \Delta\alpha_{\dot{\eta}}c(\alpha_0) \right) \right. \\ & + c(\alpha_0)(1 - \Delta\alpha_{\dot{\zeta}}\Delta\alpha_{\dot{\eta}} - \Delta\alpha_{\dot{\eta}}) \\ & \left. - s(\alpha_0)(\Delta\alpha_{\dot{\zeta}}\Delta\alpha_{\dot{\eta}} + \Delta\alpha_{\dot{\eta}}) \right] \\ & + D \left[\theta \left(c(\alpha_0)(1 - \Delta\alpha_{\dot{\zeta}}\Delta\alpha_{\dot{\eta}}) - c(\alpha_0)(\Delta\alpha_{\dot{\zeta}} + \Delta\alpha_{\dot{\eta}}) \right) \right. \\ & + s(\alpha_0)(1 - \Delta\alpha_{\dot{\zeta}}\Delta\alpha_{\dot{\eta}}) \\ & \left. - c(\alpha_0)(\Delta\alpha_{\dot{\zeta}} + \Delta\alpha_{\dot{\eta}}) \right] \end{aligned} \quad (3.44)$$

$$\begin{aligned} T = L & \left[\theta \left(s(\alpha_0)(\Delta\alpha_{\dot{\zeta}} - \alpha_{\dot{\eta}}) - c(\alpha_0)(1 + \Delta\alpha_{\dot{\zeta}}\Delta\alpha_{\dot{\eta}} - \Delta\alpha_{\dot{\zeta}}) \right) \right. \\ & + s(\alpha_0)(1 - \Delta\alpha_{\dot{\zeta}}\Delta\alpha_{\dot{\eta}}) \\ & \left. - c(\alpha_0)\Delta\alpha_{\dot{\eta}} \right] \\ & - D \left[\theta \left(s(\alpha_0)(\Delta\alpha_{\dot{\zeta}}\Delta\alpha_{\dot{\eta}} - 1) - c(\alpha_0)(\Delta\alpha_{\dot{\zeta}} - \Delta\alpha_{\dot{\eta}}) \right) \right. \\ & + c(\alpha_0)(1 - \Delta\alpha_{\dot{\zeta}}\Delta\alpha_{\dot{\eta}}) \\ & \left. - s(\alpha_0)(\Delta\alpha_{\dot{\zeta}} + \Delta\alpha_{\dot{\eta}}) \right] \end{aligned} \quad (3.45)$$

At the early stage of VÆMPS, it was decided to use a look-up table to determine the lift, drag and moment coefficient. But during the operation it might happen that the airfoil is deformed such that it might gets slender, elongates or buckles. All these deformations have influences on the aerodynamic profile coefficients. A small investigation, presented

in Appendix B, was conducted to inspect the change and if another method should be used. It was spotted that only a large variation of the Reynolds number would lead to an impractical use of the look-up table.

Next to the forces introduced by the aerodynamics, there are two more forces which have to be considered, the gravitational and centripetal forces. During the operation of a HAWT the gravitational component either works in the direction of the rotation or against it, depending on the azimuth position of the blade. Meanwhile the centrifugal force is acting towards the tip and thereby stiffing it in the flapwise direction [9]. In the case of VAWT the centrifugal forces will be pushing the blades in to an outwards movement while the gravity is acting downwards. Leading to the fact that in operation the centrifugal force will be of more importance and in parked condition the gravity. Figure 3.6 shows that the gravitational load will be different depending on the blade shape. On a H-rotor the forces will act along the blade and on the support structure. Due to the curved blade the Darrieus will have a gravitational load that acts on the blade itself. Therefore the root section of the Darrieus has to hold the weight of the entire part. So either the root part will be reinforced or other support structure has to be added in order to withstand the parked loads.

3.2.4 UMPM outline

After the aerodynamic basics are laid out the simulation tool will be explained. The Unsteady Multibody Panel Method (UMPM) will be used to capture the near wake influence. The tool was developed as a part of the master thesis of Dixon [15]. It is based on a discretization, where every panel edge has its own Doublet strength, as described in subsection 3.2.2. Depending on the location on the blade this strength will change. One of the main advantage of the panel method is that the Kutta condition is already enforced during the implementation, therefore it can be assured that the flow leaves the trailing edge smoothly [37]. Additionally, the orientation of the panels is formed by the cross-section and therefore its blade-wake interaction is directly related to the airfoil. In Figure 3.17 it can be seen how a H-rotor is discretized by UMPM. At the tip of the blade and leading and trailing edge the density of panels is higher since the variation in double strength is bigger. This panel distribution is achieved through a combination out of a cosine and linear spacing.

In the mid-section a simple cosine spacing would lead to long stretched panels that could introduce numerical instability. It was decided to have a moving transition between the linear and cosine spacing, which tends to space linear if the amount of points is increased. The spacing between a sampling of -0.5 and 0.5 can be stated as below, where N notes the vector of sampling point and n the amount of points. In Figure 3.18 it can be noticed that it is possible to sample a lot of points at the edges while having no slender panels in the the mid section with a low number of points.

$$N = \begin{cases} \text{Cosine sampling} & \text{between } -0.5 \text{ and } -0.5 + 0.5 \frac{n-3}{n} \\ \text{Linear sampling} & \text{between } -0.5 + 0.5 \frac{n-3}{n} \text{ and } 0.5 - 0.5 \frac{n-3}{n} \\ \text{Cosine sampling} & \text{between } 0.5 - 0.5 \frac{n-3}{n} \text{ and } 0.5 \end{cases}$$

Following from the discretization of every single element, it is necessary to define the entire simulation environment. UMPM encloses three levels of details [15]. The first level is the

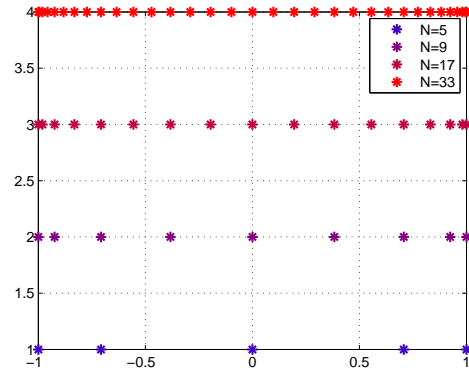
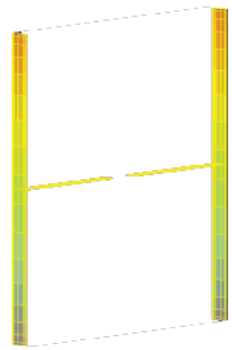


Figure 3.17: Discretization of an H-rotor in UMPM **Figure 3.18:** Lin-Cos spacing with different amount of points

global environment in which all simulation parameters are defined, such as run time, wind speed, density, turbulence, a variation of possible flag options, etc. The turbine itself is defined in the ensemble part, consisting out of its own coordinate system, motion function and the connection between all elements. These elements are parts like the blade and struts. Every single element will be shedding a wake unless it is defined otherwise. An element is a component of the turbine such as blade and struts, depending on its definition every single element can shed a wake. In Figure 3.19 a graphical interpretation of the setup can be found. It can be noted that every element has its own coordinate system which will be transformed into the one from the ensemble.

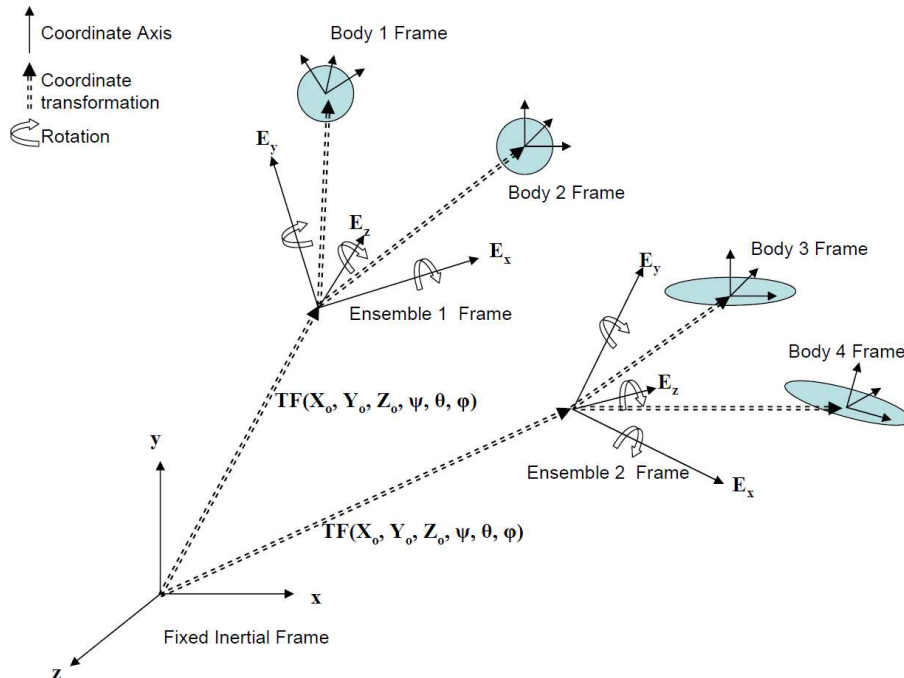


Figure 3.19: Coordinate frame definition [15]

After the simulation is set up, the problem is ready to be solved. The algorithm consists

out of three stages, which will be evaluated every iteration.

1. Updating the geometry and adding new panels
2. Solving the potential flow
3. Post-processing and updating the wake

The first step is mainly affected through the rotation of the entire structure around the vertical axis. This is done by an angle, determined through the product of time and rotational speed. Next to moving the structure, an additional row of panels has to be added, such that the connection between wake and blade is not lost. Normally the wake will experience a down wash effect while being released in the direction of the freestream. Dixon [15] suggests different ways of modeling this effect. The ones he implemented are "parallel to the free stream" and "parallel to the top and bottom surface". The "parallel to the free stream" approach will be less accurate but is more stable during operation which is the reason, why this model is chosen during the coupling. Especially as there are many other factors increasing the risk of numerical instability, it is desired to reduce every possible risk.

The next step is to solve the potential flow, where wake strength are calculated using the derivation of Hess and Smith [26]. This calculation is based on all influences by the wake on a consistent body geometry. The potential flow equation can be found in Equation (3.46).

$$\Phi(x) = \frac{1}{4\pi} \int_{S_B} \left[\sigma \frac{1}{r} - \mu \frac{\delta}{\delta n} \left(\frac{1}{r} \right) \right] dS + \frac{1}{4\pi} \int_{S_W} \left[\mu \frac{\delta}{\delta n} \left(\frac{1}{r} \right) \right] dS(x) \quad (3.46)$$

with

$$\sigma = \frac{\delta \Phi}{\delta n} - \frac{\delta \Phi_i}{\delta n} \quad (3.47)$$

$$\mu = \Phi - \Phi_i \quad (3.48)$$

Equation (3.49) is representing the system which needs to be solved for the Doublet strength μ_j . The index notation i and j are the column and row of the body panels. The subscript k indicates the appropriate wake panel. The matrices are determined through the geometry and are updated every time step. Solving the equation results in a new Doublet strength. Due to the fact that every time step a row of wake panels is added, matrix C will increase as well. This increase of the matrix will raise the computational cost. Dixon [15] implemented a time saving approach where he is adding and subtracting the influences of the near wake out of the appropriate columns of A_{ij} , to reduce some minor costs.

$$A_{ij}\mu_j + B_{ij}\sigma_j + C_{ik}\mu_k = 0 \quad (3.49)$$

$$\begin{aligned} A_{ij} &= -\frac{1}{4\pi} \int_{S_j} \frac{\delta}{\delta n_j} \left(\frac{1}{r_{ij}} \right) dS_j \\ B_{ij} &= \int_{S_j} \frac{1}{r_{ij}} dS_j \\ C_{ij} &= \frac{1}{4\pi} \int_{S_k} \frac{\delta}{\delta n_k} \left(\frac{1}{r_{ik}} \right) dS_k \end{aligned} \quad (3.50)$$

The last stage "Post-processing and updating the wake" will determine the pressure and load distributions, which are needed in further calculations such as forces that lead to deformation and therefore to a change of the inflow conditions. Additionally, it is required to update the wake, especially if it is set to be free. In this configuration the wake is allowed to roll up after its release and thereby starting to overlap and vanish. The influence of the panel strength decreases with the factor of $\frac{1}{r}$. This would imply that the strength tends to go to infinity in the core, resulting in a non-solvable problem. A more appropriate model, that covers the physic close to the core, was developed by Rankine. Equation (3.51) predicts the ideal vortex behavior, approaching zero after the radius of the vortex filament is crossed.

$$V_{\theta}(\vec{r}) = \begin{cases} \frac{\Gamma}{2\pi r_c} \vec{r} & , 0 \geq \vec{r} \geq 1 \\ \frac{\Gamma}{2\pi r_c} \frac{1}{\vec{r}} & , \vec{r} > 1 \end{cases} \quad (3.51)$$

The wake is updated each iteration, so with every iteration the simulation has to advance in time. Currently this stepping is either done with an explicit Eulerian time step (Equation (3.52)) or the Adam-Bashforth time advancing. Adam-Bashforth is an explicit linear multistep method, which takes into account all previous time steps, which showed to be more time consuming.

$$\vec{x}_{n+1} = \vec{x}_n + f(\vec{x}_n, t)\Delta t + O(\Delta t^2) \quad (3.52)$$

In an aeroelastic simulation both models should be quick together, therefore it is decided to use the Eulerian Method. It only has to be kept in mind that the Eulerian has an error of the order of two, which will increase in time. So another time stepping method will be more wisely, but as the simulation is already time consuming, the cost should be kept low as well.

Ferreira [17] implemented in his Unsteady Multibody Panel Method (UMPM) different aspects to speed up the calculation, such that it is feasible for aeroelasticity and optimization. A list of add-ons that increases the performance of UMPM can be found below:

- *Frozen wake assumption*

The wake is not allowed to deform after release and is only transported downstream. In Figure 3.20 it can be seen that the frozen wake assumption will have a slight over prediction. Still it returns satisfying results. There is no data available, proving an acceleration of the simulation but it can be said that the problem will be reduced from an N^2 -problem down to a N -problem, since deformation and wake-wake influences are kept constant. This could speed up the simulation by a factor of 100, depending on the discretization [65].

- *Number of panels till far wake assumption*

After a defined amount of panels a far wake assumption will be used. This means that the amount of panels is reduced which influence each other. The output will be pushed closer to a frozen wake assumption. Due to the fact that the far wake assumption does not update the wake and neglects the wake deformation, the amount

of iterations will be reduced. The accuracy will be reduced to as seen Figure 3.20 but also the computational time.

- *GPU parallelization*

The Graphic Processor Unit (GPU) is the only real accelerator for this simulation tool and does not influence the accuracy. It parallelizes the calculation of the wake interactions and splits the process on to different GPU cores. By this parallel process it is possible to speed up the simulation with a factor up to 20. In Figure 3.21, a test case of an H-rotor with different amount of panels was used to show the effect when the GPU is enabled. A GPU only has simple cores, which can only execute linear operations, which leads to the fact that parallelization only uses a linear relation to determine the wake interaction, as it can be seen in the figure [65].

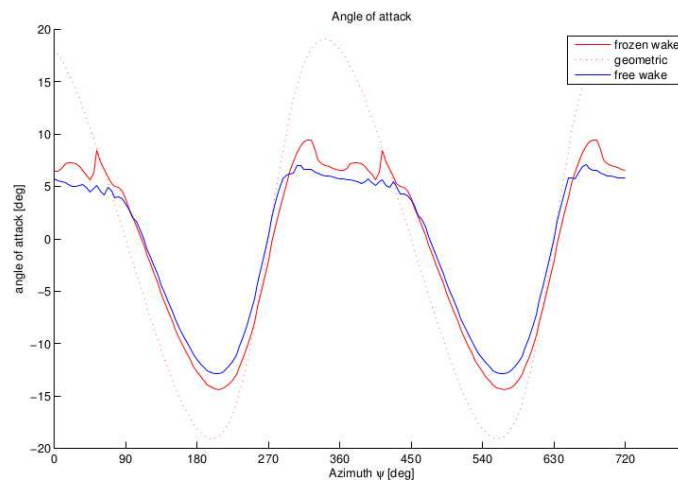


Figure 3.20: 2D angle of attack comparison for frozen and free wake of a VAWT ($B=2$, $\lambda=3$, $\sigma=0.3$) [15]

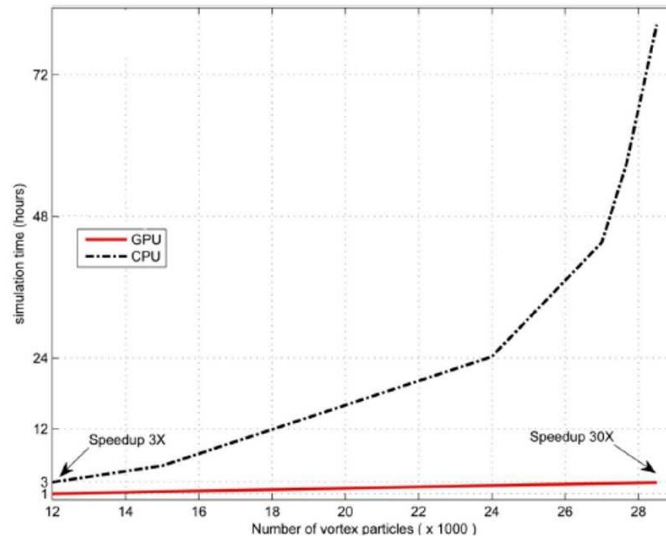


Figure 3.21: Influence of calculation time with respect to the amount of used panels [65]

3.3 OWENS - Structural Solver In VÆMPS

In an aeroelastic model the structural solver is needed too. In the following section the methodology of the structural approach will be covered as well as the interior design.

3.3.1 Structural Methodology

During every iteration the structural solver is required to solve the equation of motion (EoM), which represents the entire body, the external forces and the forces introduced by the motion. The Equation (3.53) [48] consists of multiple parts. The displacement vector X symbols the position and orientation in the reference frame, and first and second derivative (\dot{X} and \ddot{X}) the velocity and acceleration of the state vector.

$$M\ddot{X}(t) + (C + G(\Omega))\dot{X}(t) + \left(K(X) - S(\Omega) + H(\dot{\Omega})\right)X(t) = F(t) \quad (3.53)$$

The EoM also includes information about the structural properties. The mass matrix M is a diagonal matrix containing the distributed mass along a blade and tower. The stiffness matrix K is obtained from the geometry and wall thickness of the bodies and have to be determined during preprocessing, explained in subsection 3.3.2. The damping matrix C can be assumed of being modal or established experimentally. The stiffness matrix is also dependent on the state vector in order to account for geometrical non-linearities. The skew symmetric *Coriolis matrix* G is linear in the rotational velocity vector Ω , which is populated with the angular velocity around the vertical axis. The symmetric *spin softening* matrix S is quadratic in Ω , representing the softening due to the rotation and centrifugal influences. The last matrix is determined by the circularity and centrifugal forces in the skew symmetric *circularity matrix* H . The right hand site of the equation is equipped with the applied forces F such as the aerodynamic forces. These forces are also dependent on the location of the blade as well as on the rotational velocity. But the

two codes are coupled, such that the structural solver only extracts the forces at a certain time step from the aerodynamic solution and making it independent of X .

As mentioned the equation of motion covers multiple components, which have to be defined initially. These components are bodies like the tower, blades and struts. For each of these bodies it is required to know the mass, inertia and stiffness. During this thesis only the blades will be calculated exactly, all other parts are defined such that they do not influence the simulation, meaning a low mass and high stiffness.

The gravitational loads act on the entire structure as seen in Figure 3.6. This loading condition becomes of great essence, especially if the turbine is parked and the blades of Darrieus have to carry their own weight. It could be possible to reinforce the structure with struts, similar to the ones in an H-shaped rotor or to use a thicker airfoil closer to the root section. Struts would be simple to add, but the disadvantage of such an approach would be that the struts will increase drag and therefore reduce the power output. Logically it the amount of reinforcement should be limited, such that the power output will not be influenced. In this thesis they have been completely neglected

Multibody System

The discretization of such a structure can be done with multiple bodies, linked via joints such as revolute joints, which allow rotation around that joint. Another possibility is to connect the bodies with a spring-damper system, allowing thereby tension and compression. Instead of having a fine mesh, which requires a lot of computational power, the multibody system can be evaluated with an equation of motion for every single body.

In order to reduce computational cost even further the single elements can be modeled with simple structures such as beams, where the properties of stiffness and inertia are known. In OWENS these beams are modeled such that they are not capable to include panel buckling, which will mean that the airfoil cannot change in shape and therefore does not vary its lift drag polar values. The possible deformations are torsion, bending and deflection. Usually these beams are model by Eulerian Beams, where the cross-section remains perpendicular to the neutral plane. A better representation can be achieved with Timoshenko beams.

A Timoshenko beam introduces more flexibility by an additional variable which states the angle between the perpendicular cross-section of the Eulerian beam and deformed beam, therefore it will take into account shear and rotation of the inertia. A graphical interpretation can be found in Figure 3.22. Timoshenko introduced a correction factor κ to model shear correctly, given in Equation (3.54) [66]. Commonly the Timoshenko beams are used for short thick beams, because there the difference between Timoshenko and Euler-Bernoulli becomes significantly, nonetheless Timoshenko will also be used in this thesis, as it was shown by B. Owens [53] to be more accurate.

$$\kappa = \frac{\text{Average shear strain on a section}}{\text{shear strain at the centroid}} \quad (3.54)$$

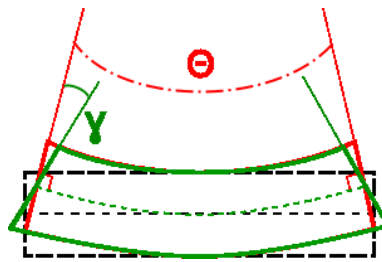


Figure 3.22: Timoshenko beam element

Another aspect that reduces the computational cost is the use of a fixed reference frame that is rotating together with the structure. OWENS has multiple frames, which are used during the simulation as it can be seen in Figure 3.23. The initial frame is the n -frame, which is not allowed to vary in time. The platform frame p can change in time, due to the hydrodynamic motion, if the platform is set to be floating. The last reference frame is the hub frame H , which remains aligned with the rotor and moves with respect to the rotational velocity. It can be noticed that the p_3 and H_3 are aligned, following from the fact that this will be the rotational axis. The H -frame is also the frame in which the EoM is solved.

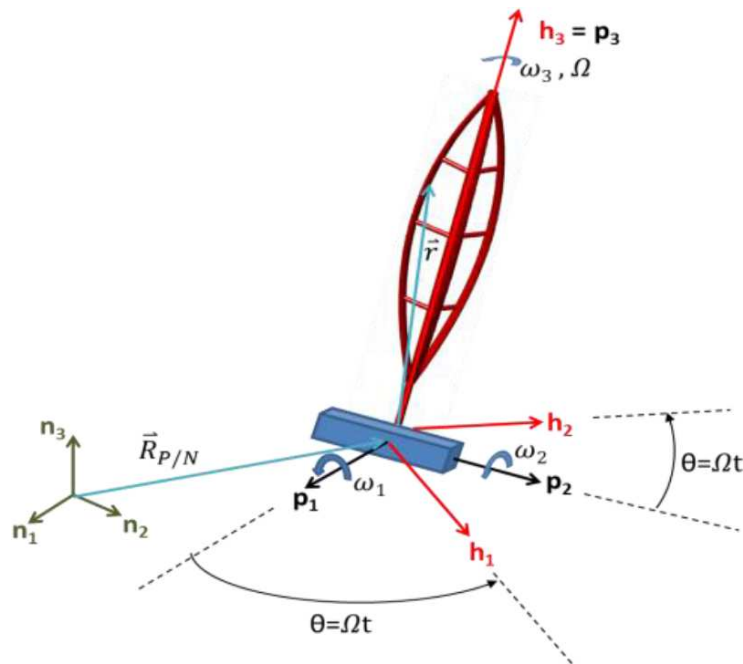


Figure 3.23: Operating coordinate systems of OWENS [53]

3.3.2 Cross-Section Model

Figure 3.24 displays the graphical interpretation of the internal airfoil design including the wall thicknesses. It is possible to determine all necessary properties with the help of the airfoil geometry and the known wall thickness.

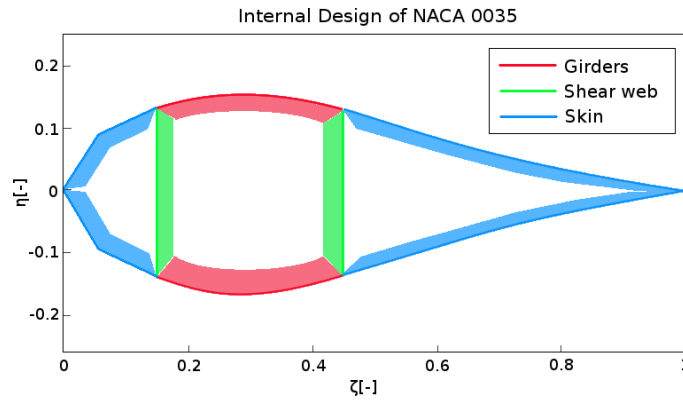


Figure 3.24: Graphical interpretation of a reinforced airfoil of a NACA 0035

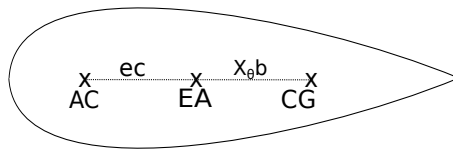


Figure 3.25: Airfoil geometry points

Firstly the enclosed cross-section area can be found by integrating the geometry points. This contour also includes three points of interest: the aerodynamic center (AC), the center of gravity (CG) and the elastic axis (EA), shown in Figure 3.25. The aerodynamic center is the only point that is independent of the structural design and is defined as the point at which all aerodynamic forces act on. The change of the moment coefficient with respect to the angle of attack is at this point equal to zero (Equation (3.55) [32]). As the point is moving with the angle of attack, following from the change of forces, it is decided to use the quarter chord point as the concentration point of the aerodynamic forces. The center of gravity can be found at the point where the mass of the airfoil does not result in a moment (Equation (3.56) [27]). Lastly the elastic axis (EA) is the line at which the applied load only produces pure bending and no torsion (Equation (3.57) [72]). In the graph the axis is displayed as a single point, due to the fact that blade is three dimensional and the point is representing the EA along the z -axis.

Usually the AC is in front of the EA and the CG is behind both points [11]. M. Schelbergen [62] addressed in his thesis that panel buckling is big issue of a Multi-Megawatt VAWTs, an approach would be to add another shear web at the trailing edge. This addition moves the CG backwards and increases the weight, which will mean that the elastic axis might move forward to counteract the moment. Such a forward motion would be not beneficial to the aeroelastic stability [72].

$$\frac{dC_{m_{AC}}}{d\alpha} = 0 \quad (3.55)$$

$$M_{CG} = \int_A m (r - CG) dA = 0 \quad (3.56)$$

$$M_{EA} = 0 \quad (3.57)$$

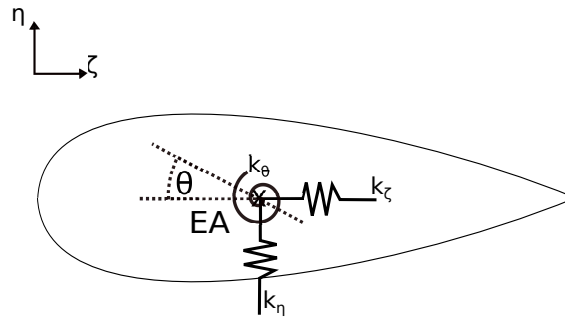


Figure 3.26: Airfoil stiffness

Next to these points it is also necessary to determine the moment of inertia of the airfoil by integrating the occupied space over the area (Equation (3.58) till (3.60) [47]). Numerically this can be done by superimposing the structure into multiple simple geometries and summing their moment of inertia to the total centroid.

$$I_{\zeta} = \int_A \eta^2 dA \quad (3.58)$$

$$I_{\eta} = \int_A \zeta^2 dA \quad (3.59)$$

$$J_z = \int_A (\zeta^2 + \eta^2) dA \quad (3.60)$$

The last missing property of the airfoil is the overall stiffness, which determines how much the cross-section will move due to a certain load. An abstract representation would be to use springs that are connected to the elastic axis (see Figure 3.26). This overall stiffness in flap and edge direction is equal to the sum of the stiffness of each element in the blade, which is the product of the moment of inertia and the Young's Modulus, defined through the material.

$$k_{\zeta} = EI_{\zeta_{tot}} = \sum_{i=1}^n EI_{\zeta_i} \quad (3.61)$$

$$k_{\eta} = EI_{\eta_{tot}} = \sum_{i=1}^n EI_{\eta_i} \quad (3.62)$$

$$k_{\theta} = GJ_{z_{tot}} = \sum_{i=1}^n GJ_{z_i} \quad (3.63)$$

3.3.3 Campbell Diagram

The Campbell diagram represents the eigenfrequencies at different operational speeds. These eigenfrequencies are determined through Nastran at a variation of TSRs between 0.5 and 8. During this analysis it is assumed that the blades are pre-stiffened such that effects

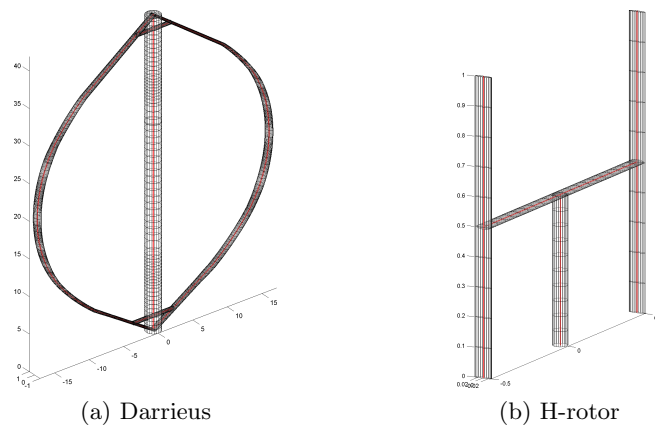


Figure 3.27: *Generated mesh of a VAWT by VAWTGen*

like centrifugal stiffening are included. This is also the reasons, why the eigenfrequency is increasing with the rotational speed. Additionally, the Campbell diagram includes the rotational speeds of a single blade as well as the multiples of the curve, which are displayed with a dotted line and the notation of $1P$. An elaborate explanation can be found in [31].

3.3.4 Structural Simulation

The simulation tool solving the structural problem is the Offshore Wind Energy Numerical Simulation tool, OWENS, developed at Sandia National Laboratories. OWENS is a dynamic multibody solver. As discussed previously these bodies are located on different reference frames, depending on their motion. Another tool developed at SNL is VAWTGen, which creates the necessary input-format required from OWENS, such as the structural properties and the geometry. VAWTGen is capable of variable rotor shape configuration, such as Darrieus, V- or H-rotor. An example can be found in Figure 3.27.

The name OWENS indicates that it is not only capable of solving structural dynamic problems, but also to simulate an entire floating offshore turbine. A schematic of its possibilities can be found in Figure 3.28. It can be noticed that OWENS also contains a hydrodynamic module and an aerodynamic module, which is the lifting line model, Cactus. This model was exchanged through UMPM, such that the near wake behavior can be included. The new coupling between both models will be explained in the following section.

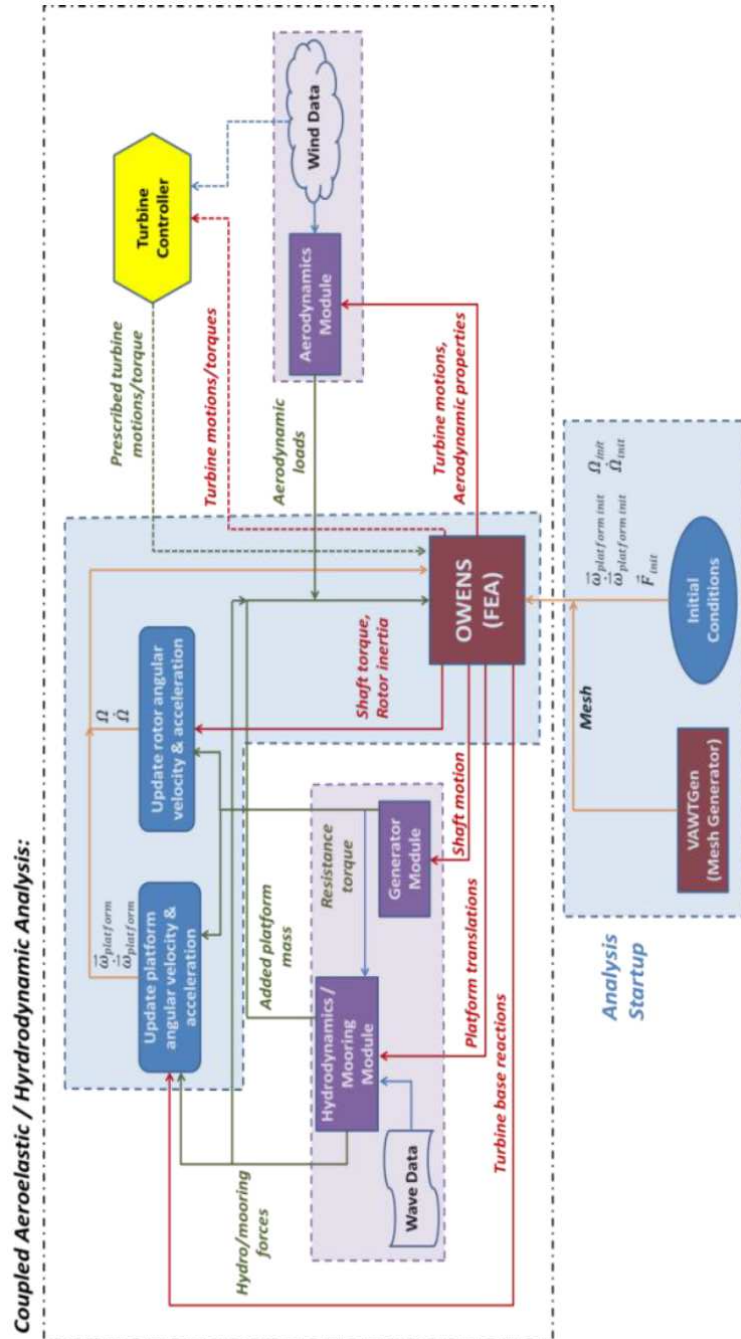


Figure 3.28: System of OWENS framework [53]

3.4 Numerical Aeroelastic Analysis

In this thesis the aerodynamics and structure are worked out in separate simulations to keep the problem simple. Therefore a coupling and an interpolation scheme are needed to be defined. This section will give an overview on how the simulation is defined in between the two solvers.

3.4.1 Interpolating Between Two Discretizations

As mentioned earlier, it is possible that an aeroelastic simulation has two different discretizations. The aerodynamic mesh should be fine enough such that the simulation is stable and responds accurately. The meshing of a structural solver can be done more rough, to keep computational cost low. This introduces an offset between the meshes, which will lead to numerical discretization errors. Two possible approaches could reduce this issue, either with identical meshes or with an interpolation method in between. Table 3.9 contains the most significant ad- and disadvantages.

An identical mesh would mean that no interpolation is needed. A finer structural mesh has a higher computational cost and does not result in a much more accurate result than with a rougher sampling. Additionally, this requires that the user has to ensure that the sampling in the two models is the same. But if both models could use the same input files, a user mistake is avoidable. During the process of this thesis a translator was developed that operates as an add-on of VAWTGen, where the OWENS is formulated such that UMPM is capable creating its own discretization.

Regardless of this translator, the issue of two codes not operating at their optimal point remains. Therefore the second solution might be more attractive. Depending on the interpolation method the truncation error can be minimized. In Figure 3.29 the error trend with respect to various discretization and interpolation schemes can be found, such as the nearest neighbor method (NN) and the radial-basis function (RBF). The error analysis was done on a simple 2D problem, where the displacement was evaluated as a sinusoidal curve, which was handed to the aerodynamic sampling points. It can be observed that the NN has a first order accuracy and RBF a 2nd order. Additionally, it needs to be stated that the RBF tends to become constant after a certain amount of mesh points. This follows from chosen support radius, which was set to be ten times of the maximum spacing. The used RBF is given in Equation (3.64), this version is known as a C^2 radial basis function, where the points are determined through a support radius r . Figure 3.30 displays the weighting of the influencing points, where the point of interest is in the origin. Close to the origin the weight is about 1.0, while every point out of this support radius

Table 3.9: Trade-off table for solver approaches during the aeroelastic analysis

Option	Advantage	Disadvantage
Same discretization	No interpolation required	Simulations can be inefficient
Different meshing	Simulation can work on efficient meshing	Numerical errors by interpolations

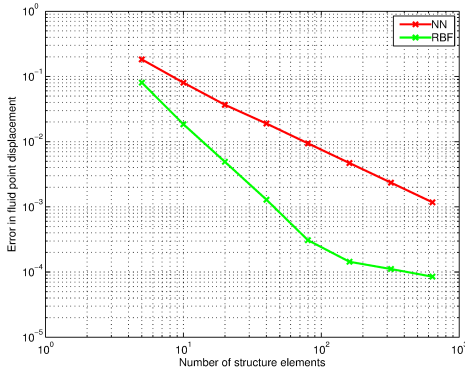


Figure 3.29: Interpolation error at displacement of Nearest Neighbor and RBF with a support radius of $r = 10 \cdot \max(\Delta x_{struct}, \Delta x_{flow})$

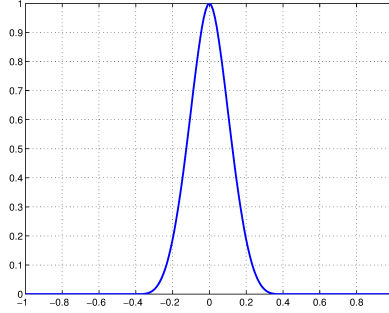


Figure 3.30: C^2 Radial Basis Function with support radius of 0.4

is equal to zero. It becomes clear that the choice of the support radius has to be done wisely. All the points inside the radius will be included in a sparse matrix which means that if more points are include, the more non-zero entries are inside the matrix, the higher the computational cost and run time [7]. In this thesis it was decided to use the RBF with a support radius of two times the maximum spacing of the OWENS discretization.

$$\phi(\|\mathbf{x}\|) = \begin{cases} \left(1 - \frac{\|\mathbf{x}\|}{r}\right)^4 \left(4\frac{\|\mathbf{x}\|}{r} + 1\right) & \|\mathbf{x}\| \leq r \\ 0 & \|\mathbf{x}\| > r \end{cases} \quad (3.64)$$

The approach of mapping the information from the structural mesh \mathbf{X}_s to the aerodynamic one \mathbf{X}_f is defining a spline function through the combination of the RBF (Equation (3.65)), with an additional requirement that the sum of the weighted polynomials q is equal to zero.

$$\mathbf{X}_f = \sum_{j=1}^{n_f} \gamma_j \Phi(|x - x_{s_j}|) + q(x) \quad (3.65)$$

$$\text{with} \quad (3.66)$$

$$\sum_{j=1}^{n_f} \gamma_j q(X_{f_j}) = 0 \quad (3.67)$$

With the RBF defined, it is possible to determine the interpolation matrix H_{fs} that contains the spline definitions of the RBF. This matrix is then capable to map the displacements in the OWENS frame Δh_s to the one in UMPM Δh_f (Equation (3.68)). The entries of such a matrix can be determined by finding the coefficients γ and β on the same mesh. γ is a vector, that contains all weights of the fitted polynomial and β includes the polynomial coefficients. These coefficient manage that the RBF results into a spline function and can be determined by solving Equation (3.69) on its own mesh. Then β and γ can be substituted in Equation (3.70), which results into transformation matrix H_{fs}

$$\Delta h_f = H_{fs} \Delta h_s \quad (3.68)$$

$$\begin{bmatrix} \mathbf{X}_f \\ 0 \end{bmatrix} = \begin{bmatrix} \Phi(|X_{f_i} - X_{f_j}|) & [1 \ x_f \ y_f] \\ [1 \ x_f \ y_f]^T & 0 \end{bmatrix} \begin{bmatrix} \gamma \\ \beta \end{bmatrix} \quad (3.69)$$

$$\begin{bmatrix} \mathbf{X}_s \\ 0 \end{bmatrix} = \begin{bmatrix} \Phi(|X_{s_i} - X_{f_j}|) & [1 \ x_s \ y_s] \\ [1 \ x_s \ y_s]^T & 0 \end{bmatrix} \begin{bmatrix} \gamma \\ \beta \end{bmatrix} \quad (3.70)$$

$$H_{fs} = \begin{bmatrix} \Phi(|X_{s_i} - X_{f_j}|) & [1 \ x_s \ y_s] \\ [1 \ x_s \ y_s]^T & 0 \end{bmatrix} \begin{bmatrix} \Phi(|X_{f_i} - X_{f_j}|) & [1 \ x_f \ y_f] \\ [1 \ x_f \ y_f]^T & 0 \end{bmatrix}^{-1} \quad (3.71)$$

During the coupling, it was noticed that the vortex panel code has numerical issues close to the root, especially in the region where the local TSR is below 1.5. This is due to the fact that the wind speed is transporting the wake downwind which pushes the vortex filaments into the ones of the blades. This will lead to a non-singular solution. In order to prevent such an error, it is advisable to model the blade only outside this local TSR, sadly this will mean that the structure mesh contains points outside of the aerodynamic domain. That is not an issue, while mapping from OWENS to UMPM. But the other way around causes problems, because the RBF is defined as an interpolation method and the UMPM domain lays inside of the OWENS one. So there is a need for an extrapolation scheme. A robust scheme is the linear extrapolation using the last points of UMPM to determine a trend. This approach was also implemented in VÆMPS and is given in Equation (3.72). The distance between the points is known and the force F is determined during postprocessing. The found relation can be then added to the transformation matrix H_{sf} at the corresponding locations. Every force outside the UMPM domain can be modeled with this approach. The only disadvantage is that at further distance the difference between the actual force and the extrapolate one might be significantly larger. But its simplicity and robustness make it the most attractive extrapolation method.

$$F(x_{s,i}) = \begin{bmatrix} 1 - \frac{x_{s,i} - x_{f,j}}{x_{f,j+1} - x_{f,j}} & \frac{x_{s,i} - x_{f,j}}{x_{f,j+1} - x_{f,j}} \end{bmatrix} \begin{bmatrix} F(x_{f,j}) \\ F(x_{f,j+1}) \end{bmatrix} \quad (3.72)$$

3.4.2 Coupling Of Two Models

After the information can be mapped on the different discretization, it is necessary to couple both methods and arrange an exchange of data. OWENS and UMPM operate both on MATLAB but in two different simulations. In order to keep the possibility of exchanging the solvers, it was decided to use Java network sockets as a communication portal.

Firstly it needs to be decided on how the communication is done. Figure 3.31 shows two options of communication. Either the coupling is done with via an external server or by direct communication. The first option allows that both simulation only act as a client, and can be focused on their own simulation. The second option is a direct approach where both models act as a client and server. The advantage of this setup is that

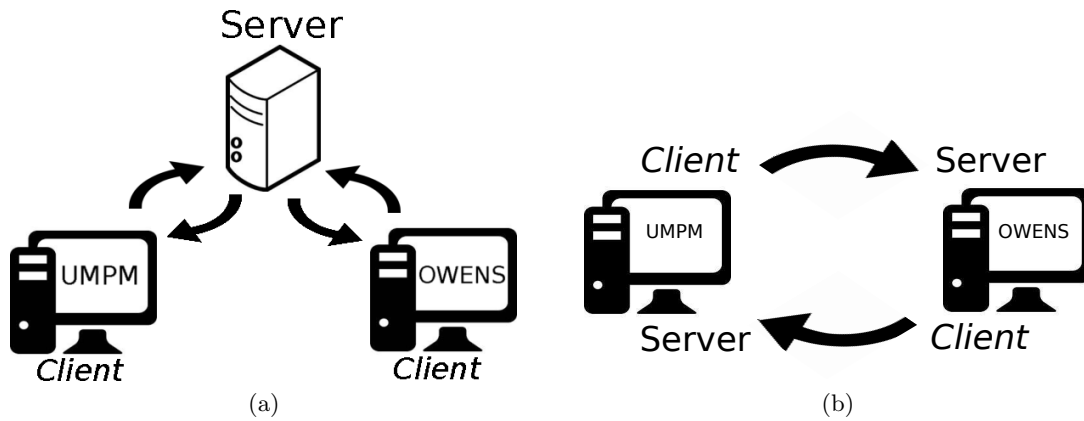


Figure 3.31: Possible network communications in VÆMPS

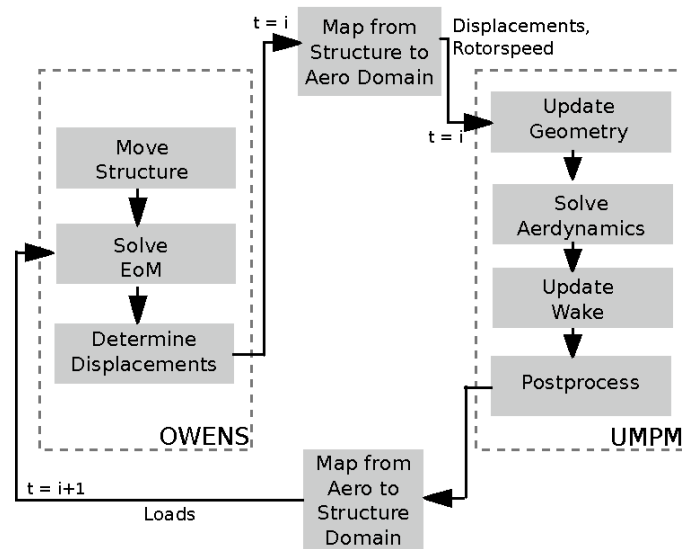


Figure 3.32: Schematic interpretation of communication between the models

no additional element is required, thereby increasing the reliability. It also requires less steps in the setup and was favored during the development of VÆMPS.

The interface in both models has to be defined such as in Figure 3.32. In this figure the two simulations are displayed in a simplified way, such that the interaction points can be seen. OWENS sends the displacements and other information to UMPM which will be used in the first part of the iteration. The resulting forces will be then included in the EoM of the next time step ($i + 1$). It becomes clear that there is a small offset in time, due to the fact that OWENS uses UMPM output of time step i , while being one step ahead. Therefore the time step needs to be chosen wisely, such that the blade does not move so much that the difference in force is significantly. This approach is also known as *loose coupling*, where no sub-iterations are executed. It was preferred due to the fact that the computational cost can be kept low and responds faster.

In order to distinguish between the different information, such that only the required is used, the data string has to be well defined. In Figure 3.33 six different types of

Length of Vector	Type	Information	Check-sum	General
1		Discretization of OWENS		
2		t, Ω , Ψ , # of elements, # of Blades, ... displacements ($dh_1, dh_2, dh_3, d\Phi, d\delta, d\Psi$)		
3		# of elements, # of Blades, ... loads ($F_{h1}, F_{h2}, F_{h3}, M_{h1}, M_{h2}, M_{h3}$)		
4		-1 (stop simulation)		
5		Offset between AC and EA		
616		Receiving type(2-4), as responds		Detailed

Figure 3.33: Definition of network strings

network strings can be found. In general the string contains four partitions, the amount of data in the string, the type, the information itself and the sum of all data in the string. The information will vary with the type. During the initialization, OWENS will submit its discretization, such that the mapping matrix (H_{fs} and H_{sf}) can be determined. Additionally, UMPM receives the distance between the *AC* and *EA* which has to be included in the moment calculations during postprocessing. The types 2 and 3 are the types that have been used also in Figure 3.32. In order to prevent that a data string is used at the wrong time, the transmission gets verified with type 616. This also allows the other member of the communication to know that the transmitted data is received. The last missing case is type 4, which sends only -1. This number will stop the entire simulation and shuts down the server-client connection. It can be seen as the exit button.

3.4.3 Initialization Of VÆMPS

After everything is defined, VÆMPS needs to be started. As both models are dynamical solvers, they require some time till they are at a continuous operating point. In UMPM the wake has to develop itself such that an influence can be noticed in the blade-wake interaction. OWENS also requires time until effects like *rotational stiffing* can be evaluated. Additionally the structural solver also considers acceleration, which occurs during starting and stopping of the turbine. It needs to be decided at which point the coupling should be executed. Two possible options are:

1. Start both separately and connect them after both simulations are at the operational point
2. Let OWENS be the simulation master and hand down the rotational speed to the UMPM

The first option would allow that both simulations can be connected after their initialization. But this is critical as it has to be ensured that the coupling happens at the same time step and azimuth position. In addition, OWENS is first turning without any wake effects and suddenly a complete developed wake is linked to the blades. This difference could lead to a numerical instability and loss of accuracy. Therefore the second option will be more likely. The simulations could start with both models in a parked condition

and the first motion as well as the time step are introduced through OWENS leading to one overall simulation tool VÆMPS.

3.5 Comparison Of HAWC2 And VÆMPS

The aeroelastic simulation tool should be compared to experimental values in order to see whether the tool performs as wanted or requires debugging. Unfortunately, there are no experimental evaluation points available. VÆMPS will be compared to HAWC2 with focus on the Sandia 34m Testbed. This turbine was chosen, because the structural properties are known and also noted down in Appendix C. The turbine is turning at a wind speed of 10 *m/s* and a tip speed ratio of 7, which is also summarized in Table 3.10. The geometry of the blade is determined through the center of gravity of each airfoil of which some points are noted down in Table 3.11.

Table 3.10: Simulation parameter of comparison

Parameter	Unit	Value
Density	[kg/m ³]	1.225
Wind speed	[m/s]	10.00
Turbulence intensity	[%]	0.0
TSR	[-]	7.00
ω	[-]	4.037

During the *Special Project* [61] the forces at different solidity and TSR were compared, so this project will focus on the displacements of the blade during operation. The blade which will be inspected is the first blade facing upwind. The azimuth angle is defined as presented in Figure 3.34, so the upwind position is between 0° and 180° and the downwind part is spanned over the rest of the circle.

Figure 3.35 and 3.36 show the displacements in the *H*-frame with respect to the simulation time. There are multiple things that can be noticed. Firstly VÆMPS only simulate the first 30 seconds following from the fact that modeling of the wake is memory intense and therefore limited to the machine. The curve has been shifted to the zoomed region, to make comparison possible. The curve marked with *flex* uses the same input data as

Table 3.11: Center of gravity points of SNL-blade

#	x-coord.	y-coord	z-coord.
1	0.00	0.00	0.00
2	6.12	0.00	4.20
3	10.88	0.00	8.40
4	12.75	0.00	10.50
5	15.47	0.00	14.70
6	16.83	0.00	18.90
7	17.00	0.00	21.00
8	16.32	0.00	25.20
9	14.28	0.00	29.40
10	10.88	0.00	33.60
11	6.12	0.00	37.80
12	0.00	0.00	42.00

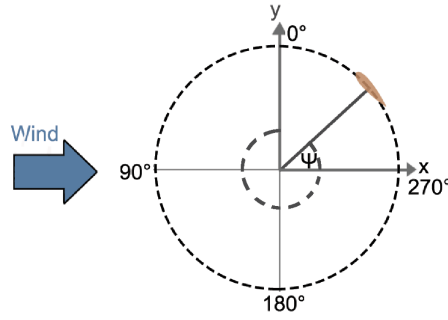


Figure 3.34: Azimuth angle definition

VÆMPS, while the *stiff* data have a higher Young's and Shear Modulus. This difference can be noticed through the fact that the *flex* curve has great displacements during the initialization and drops logarithmic to the same values as the *stiff* data. In the end of the simulation the two curves are approaching each other which is an indication of centrifugal stiffening. Such a behavior is not observed in VÆMPS, its output is more similar to the *stiff* curve, also with respect to the magnitude. During a closer look, it can be noticed that the displacements in H_1 is a combination of a low frequency with 2.39 Hz and a low one with 1.19 Hz, which is close to the one of HAWC2 of 1.28 Hz. These two frequencies lead to maximum difference of 33% in H_1 . In H_2 the maximum deflections of both simulations are nearly in the same range. There is also a shift in frequencies. While HAWC2 has the same frequency as in H_1 , VÆMPS simulates the displacements with 1.42 Hz, that also can be seen in the close up.

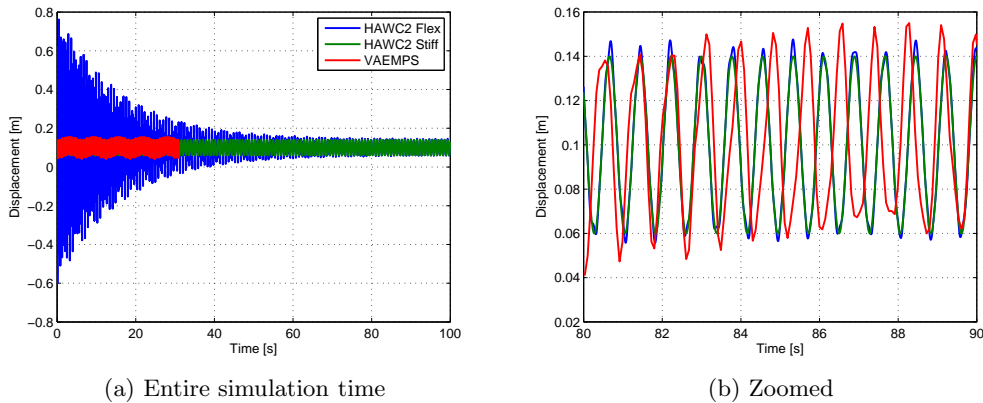


Figure 3.35: Displacement in H_1 versus time of the Sandia 34 m Testbed

Additionally, the output is averaged over a single revolution. In Figure 3.37 the difference become even more obvious. Because of the averaging the maximum difference of both curve have become increased up to 41% and to a phase shift of 35°. In H_2 the phase shift is only 15° and a difference up to 25% in the upwind region. There is also a small offset between the two HAWC2 simulations, where the *flexible* blade deflects a bit more than stiff one.

The difference between HAWC2 and VÆMPS has multiple sources, that require further

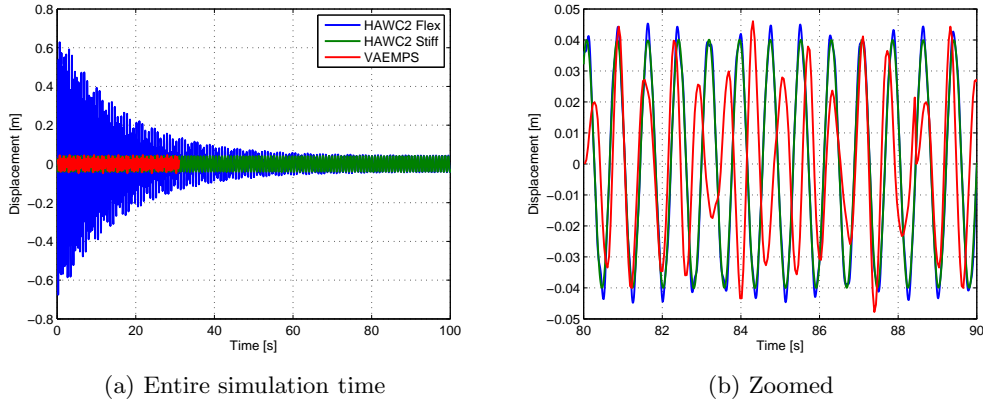


Figure 3.36: Displacement in H_2 versus time of the Sandia 34 m Testbed

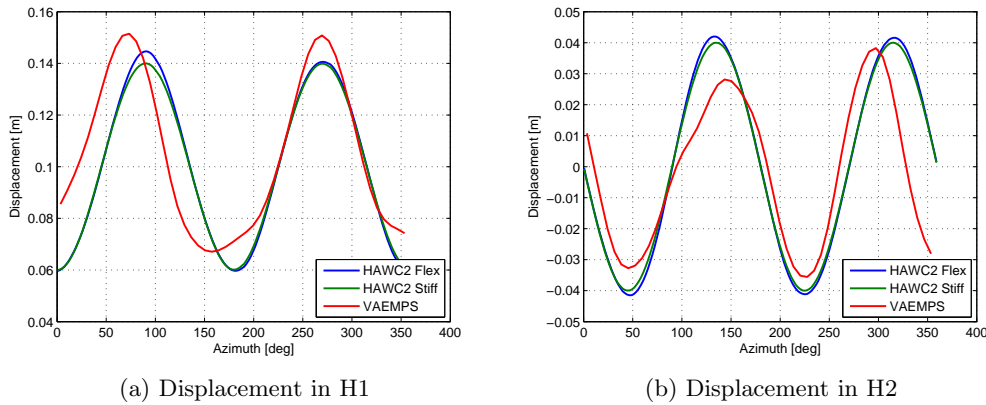


Figure 3.37: Averaged displacement versus azimuth angle of the Sandia 34 m Testbed

investigations. The main concerns are listed below:

- *Structural solver*
In OWENS the structural is assumed to consist out multiple non-linear elements [53] while HAWC2 models the sections with linear beam elements [40]. This slight difference will lead already to an offset concerning the deflection angles.
- *Aerodynamic forces*
During the *Special Project* [61] it was experienced that in a 2D there is a difference of aerodynamic forces along the downwind position and a slight phase shift of 10° . This effect might be even increased when inspecting 3D forces.
- *Wrong mapping in VÆMPS*
As mentioned earlier, the forces of UMPM have to be extrapolated towards the root regions. This will introduces uncertainties in the code that harms its accuracy.
- *Structural input values*
Both model require a different approach of handling the structural properties.

HAWC2 requires a the properties in the local x- and y-direction. However, OWENS uses the stiffness along the flap- and edgewise direction. Therefore numerical errors will be included due to the transformation between the frames. This can be avoided if a H -rotor is used during the further investigations. At this configuration the two frames are aligned.

All in all it can be concluded that VÆMPS already is on the correct way but still requires some debugging and closer inspections, to point out the differences following from the near-wake panel method. Another point, VÆMPS requires a lot of memory and computational time (15 days without GPU inclusion) in order to simulate 30 seconds of real time, while HAWC2 can simulate the 100 seconds in 2 hours. With respect to the limited time and the unidentified differences, it is decided to run the further aeroelastic simulations in HAWC2.

Simulation Results

The following chapter includes all optimization results (section 4.1). Some of these results have been analyzed in regard to stress distribution (section 4.2), the aeroelastic behavior (section 4.3) and the Campbell diagram (section 4.4). The C_P curve (4.5) and the capability of up-scaling the best design (section 4.6) are evaluated at the end of the chapter.

4.1 Overview Of Optimized Results

Figure 4.1 presents the mass to area ratio of the optimized rotors with a fixed height of 180 m and an area of approximately $1.325 \cdot 10^4 \text{m}^2$. These rotor configurations vary in their span wise distribution of blade sections. Following distributions of blade sections were used:

- **NACA0015** - Single blade section, with constant NACA 0015 airfoil
- **NACA0018** - Single blade section, with constant NACA 0018 airfoil
- **NACA0020** - Single blade section, with constant NACA 0020 airfoil
- **NACA0025** - Single blade section, with constant NACA 0025 airfoil
- **NACA0030** - Single blade section, with constant NACA 0030 airfoil
- **NACA0035** - Single blade section, with constant NACA 0035 airfoil
- **NACA0015-35** - varying blade section with NACA 0035 at root and NACA 0015 at equator
- **NACA0018-35** - varying blade section with NACA 0035 at root and NACA 0018 at equator
- **NACA0015-40** - varying blade section with NACA 0040 at root and NACA 0015 at equator
- **NACA0015-80** - varying blade section with NACA 0080 at root and NACA 0015 at equator

The last design (NACA0015-80) was included for inspecting whether a complete circular shape at the root section was more beneficial. The GFRP approach was not added due

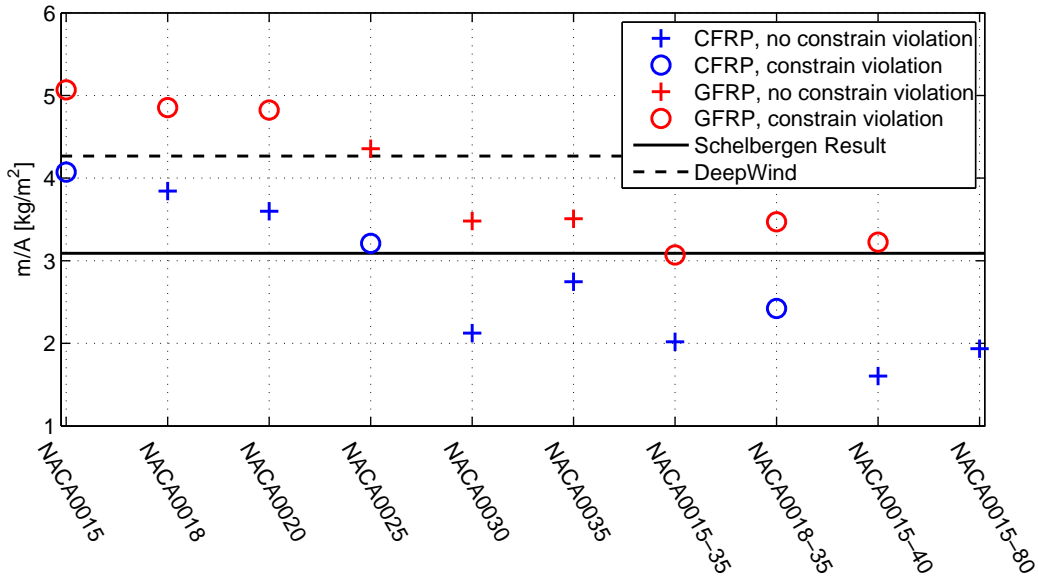


Figure 4.1: Function value of finished optimization

to challenges with panel buckling, which were obtained from the shell model in Nastran. Figure 4.1 displays the function values after the designs have been optimized on the area and the thickness distribution. It can be seen that the single blade section designs have the best mass over area ratio at NACA0035. The function values of the varying blade section are beneath this point, except for the NACA0018-35 design which also violates the optimization constrains. It is noticeable that the majority of the designs are below the function values of the original code and the DeepWind design. Some design points are marked differently in Figure 4.1, as they are violating the optimization constraints.

Figure 4.2 presents a similar trend as seen in Figure 4.1. The graph implies that a single thin blade section requires more mass, following from the fact that the designs from NACA0015 to NACA0025 have a greater mass than all other designs.

Figure 4.4 shows the quarter chord line of the blade sections, determined through the optimizer. The initial topology is included with a dotted black line. Some of the designs are marked with stars. These designs will be inspected in detail later on. Throughout the optimization, the rotor was fixed to a constant height of 180 m and was allowed to vary the radius, such that an area of a 5 MW can be reached at rated speed of 12 m/s and a C_P of 0.45. This resulted in a variety of rotor areas given in Figure 4.3. The CFRP designs show that thicker airfoils lead to a greater swept area, in order minimize the function value. The GFRP designs do not indicate a clear trend. It can only be stated that the designs are inside the area constraints. It was expected that thick airfoils will have a low function value, following from the higher structural integrity. This is confirmed in the plot. A more elaborate discussion can be found in subsection 5.1.1.

A detailed overview of the NACA0015-35 (CFRP), NACA0015-40 (CFRP) and NACA0030 (GFRP) is given in Table 4.1 as well as their thickness distributions in Figure 4.5. These

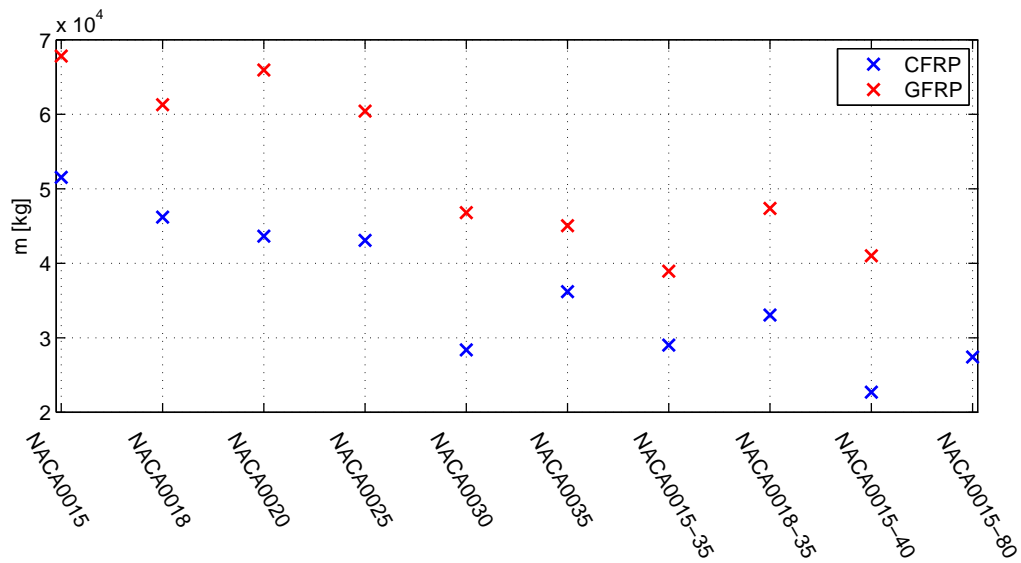


Figure 4.2: Blade mass of finished optimization

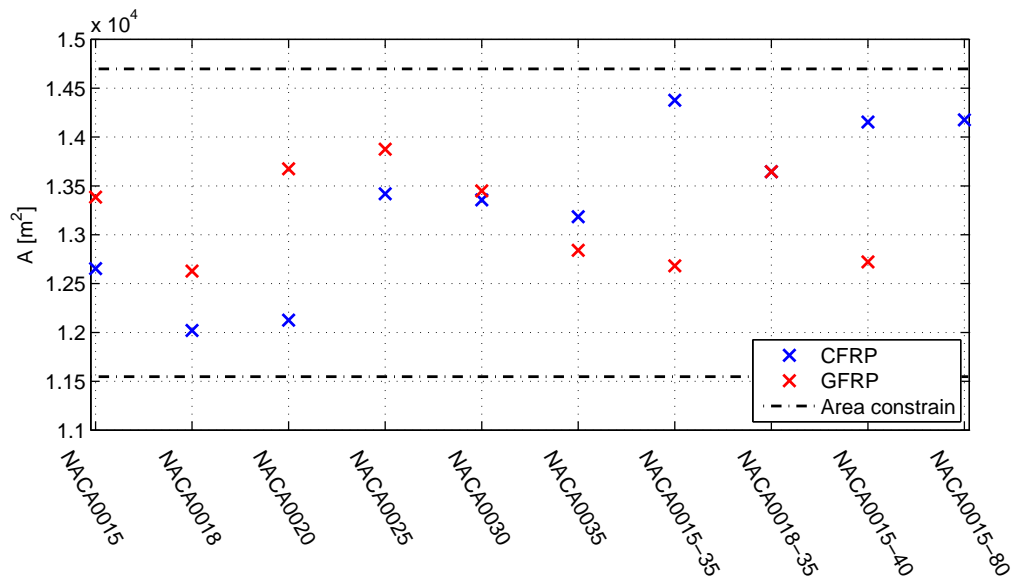
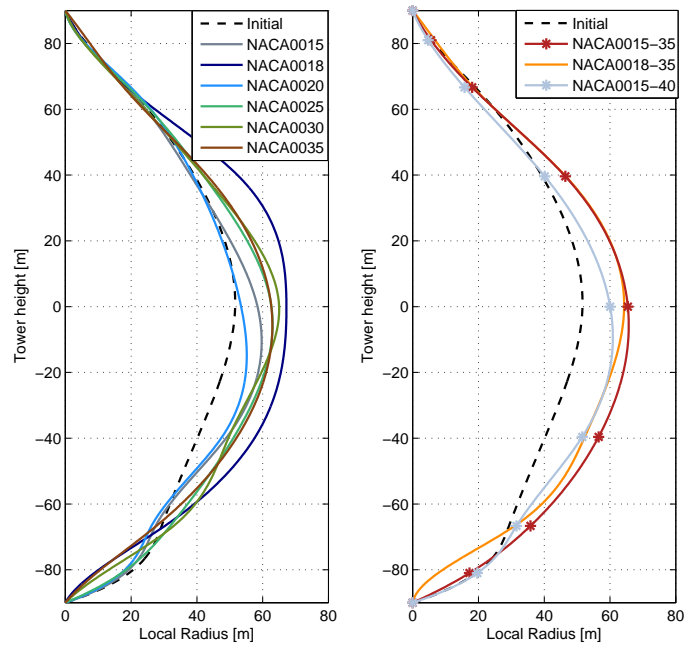
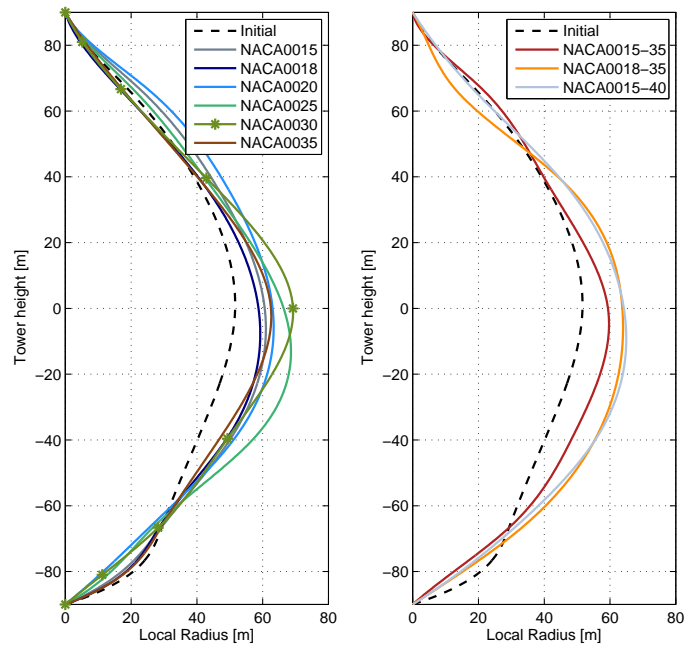


Figure 4.3: Swept rotor area of finished optimization



(a) CFRP



(b) GFRP

Figure 4.4: Optimized blade shape of a 5 MW Darrieus turbine

Table 4.1: Minimum/maximum thickness, blade characteristics and optimization output of selected designs (NACA0015-35 (CFRP), NACA0015-40 (CFRP) and NACA0030 (GFRP))

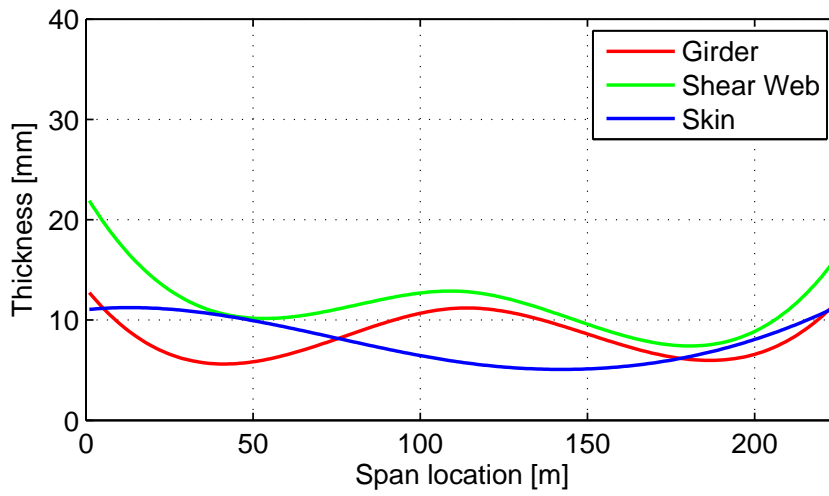
Property	NACA 0015-35	NACA 0015-40	NACA 0030
Material	CFRP	CFRP	GFRP
Amount of sections (Figure 3.1a)	5	5	5
$t_{girder_{max}}$ [mm]	13.144	12.230	34.727
$t_{girder_{min}}$ [mm]	7.274	7.570	16.114
$t_{shear_{max}}$ [mm]	22.438	17.276	24.786
$t_{shear_{min}}$ [mm]	8.769	5.882	16.416
$t_{skin_{max}}$ [mm]	11.399	24.772	26.797
$t_{skin_{min}}$ [mm]	5.270	6.149	10.338
Blade mass [kg]	28372.898	24970.645	51855.576
Swept area [m ²]	14376.122	14153.511	15277.168
Objective (m/A)	1.974	1.764	3.394
Constraint violation	0.023	0.019	0.188
Failure Index			
- Ult. strength Downwind	0.481	0.402	0.727
@ $z =$ [m]	65.55	-64.74	2.32
- Ult. strength Upwind	0.644	0.548	0.762
@ $z =$ [m]	25.46	-74.44	-65.14
- Ult. strength Parked	0.252	0.219	0.379
@ $z =$ [m]	-36.23	82.81	-53.75
- Ult. buck	0.874	0.678	1.088
@ $z =$ [m]	-75.67	-70.34	-0.52
- Max. Fatigue Damage	1.214	1.161	1.469
@ $z =$ [m]	79.60	-9.23	-0.52

three designs will be used in the aeroelastic simulations. A justification of this selection is given in subsection 5.1.1. It can be observed that these designs have a similar thickness distribution. Every cross-section has a greater thickness at the roots of the Troposkein blade. These plots disagree with the expectation that the minimum thickness is located around the equatorial region. However all plots indicate that the minimum thickness is at 50 m. The origin of the blade span is considered to be at the lower root, which will mean that 50 m is around $z = -70$ m, when the equator is used as the zero-plane.

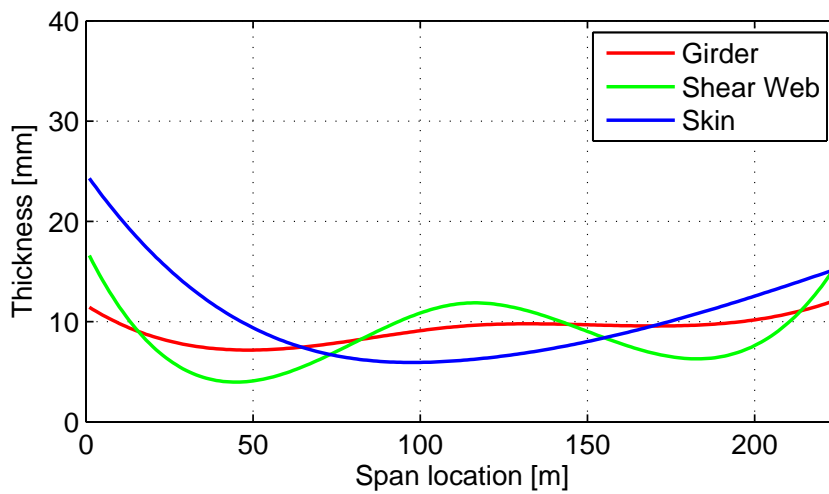
4.2 Stresses And Fatigue

The response of the blades during operation and while being parked, can be observed through the maximum failure index, shown in Figure 4.6 till 4.8. If the failure index is greater or equal to 1.0, the blade will be likely to break. In the figures this location is marked in a red. The applied loads can be found in Appendix F. Additionally, the maximum failure index and maximum fatigue damage have been stated in Table 4.1.

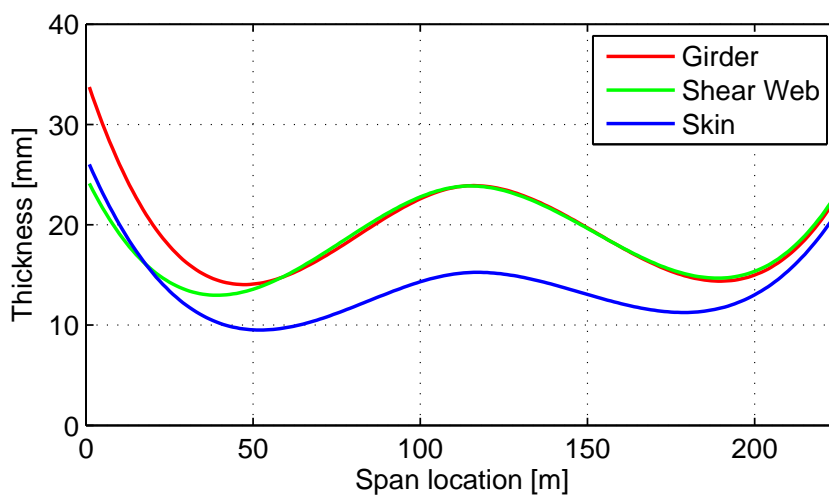
Figure 4.6 shows that the design has two critical points. The first one is located at $z = 79.60$ m. At this point the fatigue damage of the girder is beyond 1.0, indicating the region at which the design might break. The highest buckling reserve factor is at -75.67 m on the panel of on the pressure site. Figure 4.7 has a similar point concerning the buckling. Nevertheless the highest fatigue damage appears at $z = -9.23$ m at the skin.



(a) NACA 0015-35 CFRP



(b) NACA 0015-40 CFRP



(c) NACA 0030 GFRP

Figure 4.5: Cross-section thickness distribution of inspected optimized rotors

Table 4.2: Simulation environment of HAWC2 simulations

Property	Unit	Value
Wind speed	[m/s]	12
TSR	[-]	[3 4.5 6]
Turbulence Intensity	[-]	0.0
Wind shear	logarithmic	0.2
Density	[kg/m ³]	1.225
Blade location	[-]	Equator, mid-span

Figure 4.8 indicates other points concerning the fatigue. The difference is that both girder and skin have a reserve factor greater than 1.0 around the equator. The buckling analysis has determined that the NACA0035 has a great likelihood to buckle at $z = -59.50$ m and around the equator, where the fatigue is high too. A discussion of these results can be found in subsection 5.1.1.

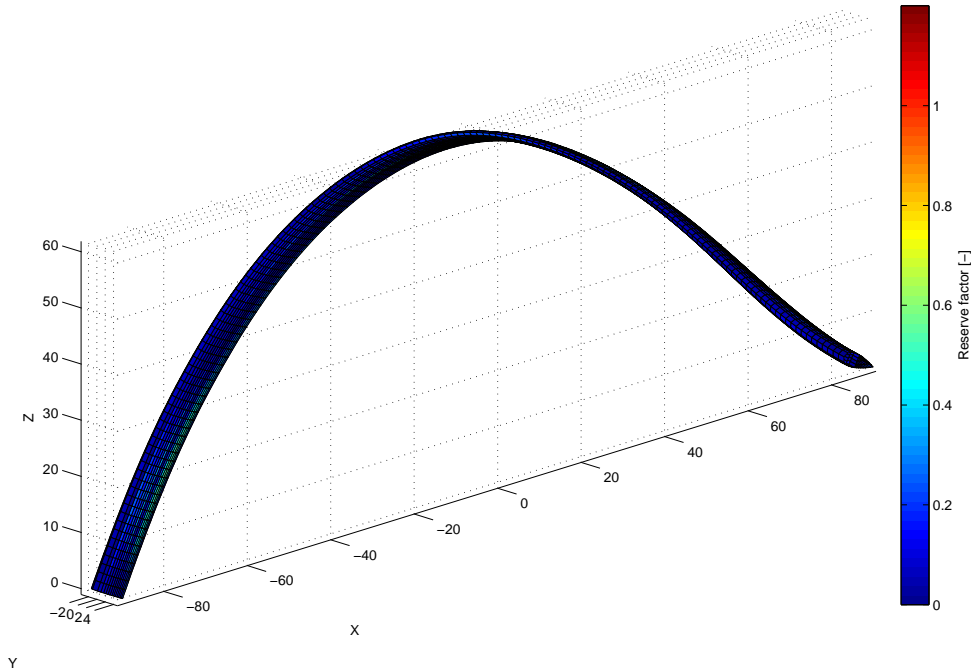
4.3 Aeroelastic Analysis Of Optimized Designs

The design conditions of the aeroelastic simulations can be found in Table 4.2. The structural properties were determined through the methods mentioned in subsection 3.3.2 and implemented in HAWC2 (Appendix D). The tower and the support structure had to be stiffened, such that no displacements were possible, in order to focus only on the blade motion. This was achieved by using high inertia and Young's modulus. The used polar coordinates can be found in Appendix E, they have been extracted from Xfoil at a Reynolds of 10^6 .

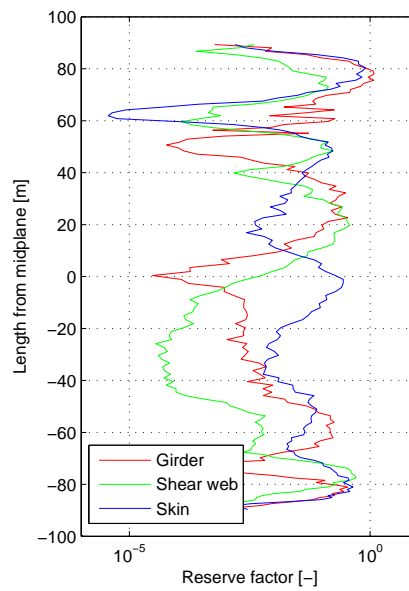
Figure 4.9 shows the displacements of the mid-span blade section versus time. The values were achieved by subtracting the position of a stiff blade from simulated results. The green line represents the TSR of 3, the blue one of 4.5 and the red one of 6. It can be seen that the curves have a periodical behavior, which increases with TSR. The same trend can be observed for the magnitude of the displacements.

The time series, determined earlier, are no indications of what displacements to expect along the rotational path. Therefore the displacements of the equatorial regions have been averaged for one revolution, shown in Figure 4.10. It can be observed that mostly the maximum displacement occur along the upwind path. However, these values are negative, which means that the cross-section experiences an inwards motion. An exception is the NACA0030 design, which has just positive displacements indicating an outwards deflection.

Instead of averaging the displacements, it is also possible to observe the appearing frequencies in the time series. This can be done with a Fourier analysis, shown in Figure 4.11. Mostly it can be noticed that the measured frequencies are multiples of the operational speed. Another option is that the frequency is close to the eigenfrequencies, which are displayed in Figure 4.12. *BM1* and *BM2* stand as an abbreviation for *Blade Mode*. In

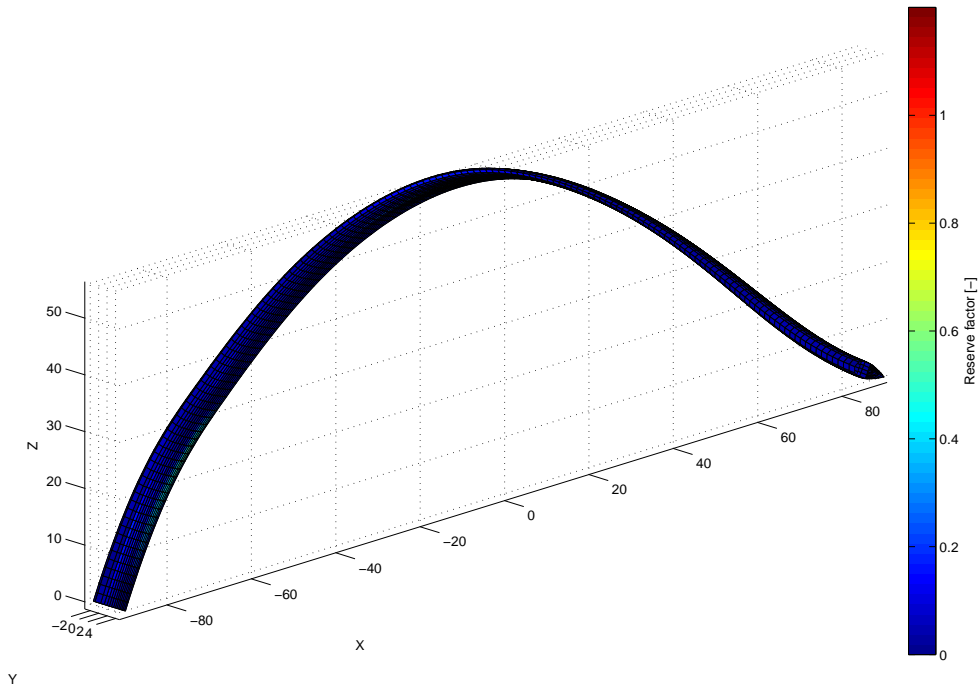


(a) Maximum Stress Failure of buckling analysis

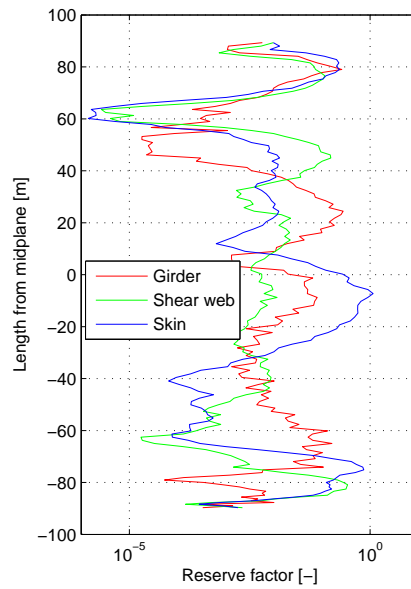


(b) Fatigue along blade

Figure 4.6: Stress and fatigue of NACA 0015-35 with CFRP

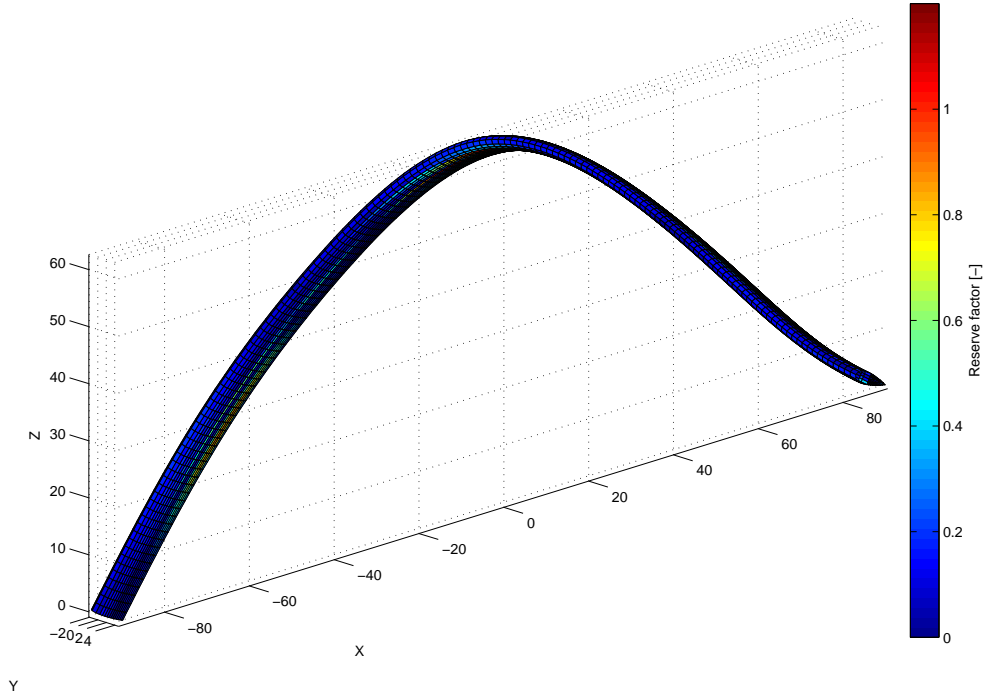


(a) Maximum Stress Failure of buckling analysis

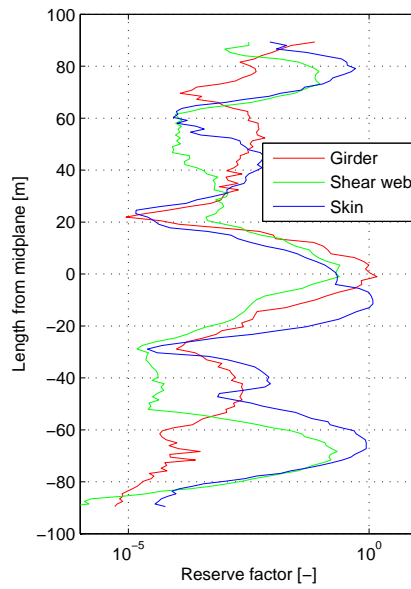


(b) Fatigue along blade

Figure 4.7: Stress and fatigue of NACA 0015-40 with CFRP

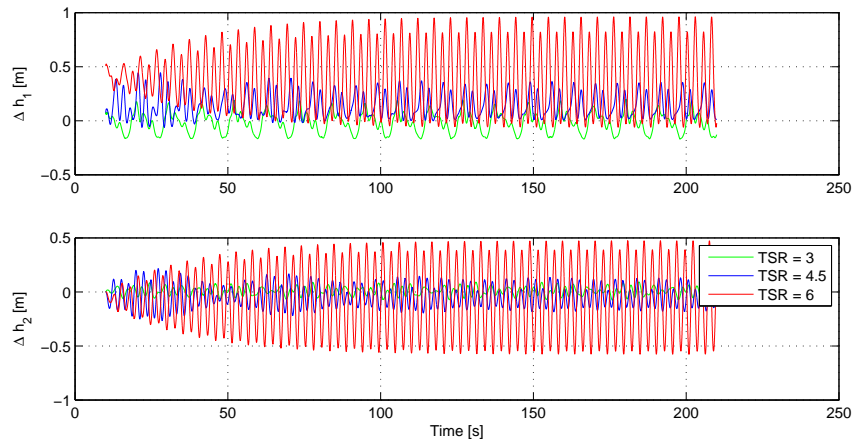


(a) Maximum Stress Failure of buckling analysis

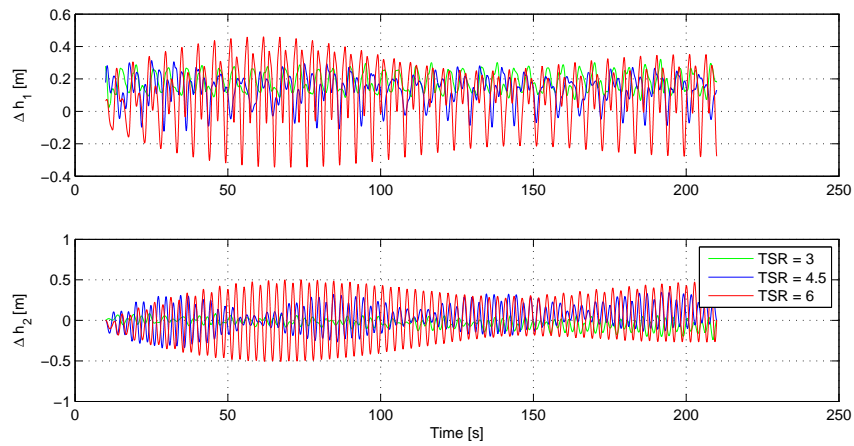


(b) Fatigue along blade

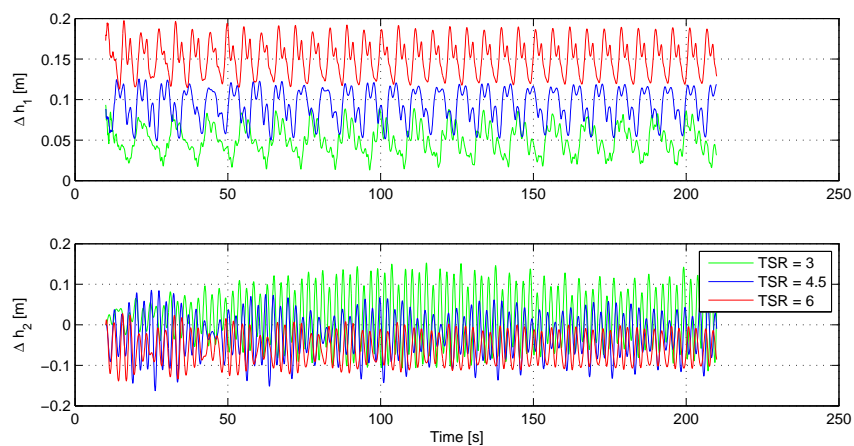
Figure 4.8: Stress and fatigue of NACA 0030 with GFRP



(a) NACA 0015-35 CFRP

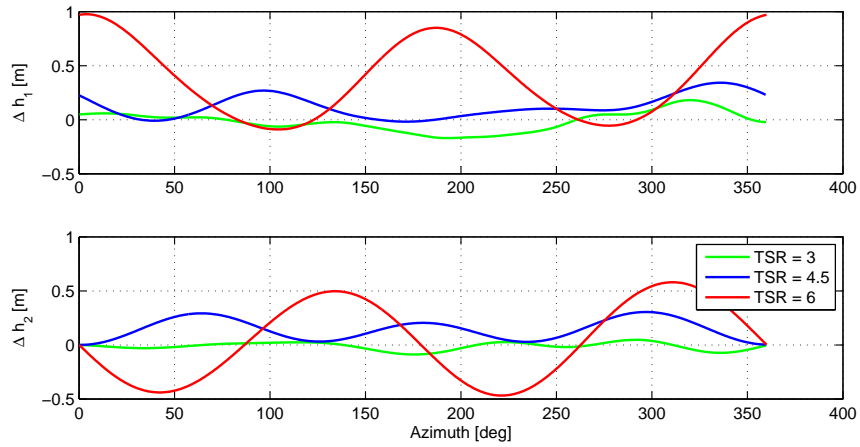


(b) NACA 0015-40 CFRP

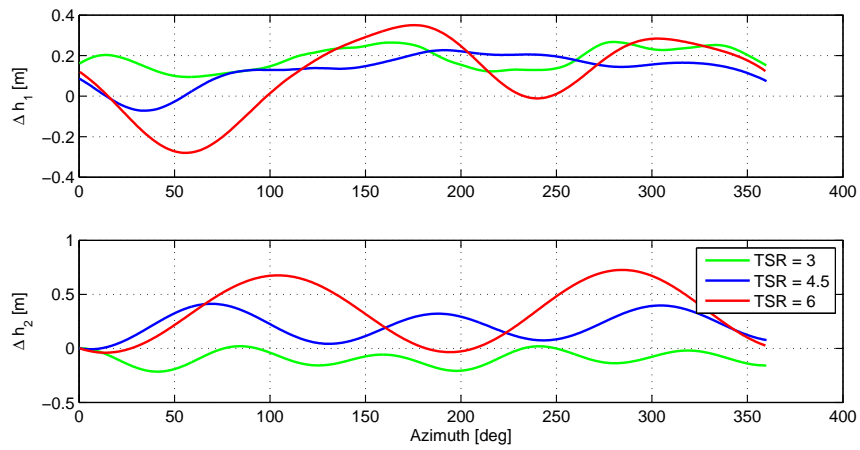


(c) NACA 0030 GFRP

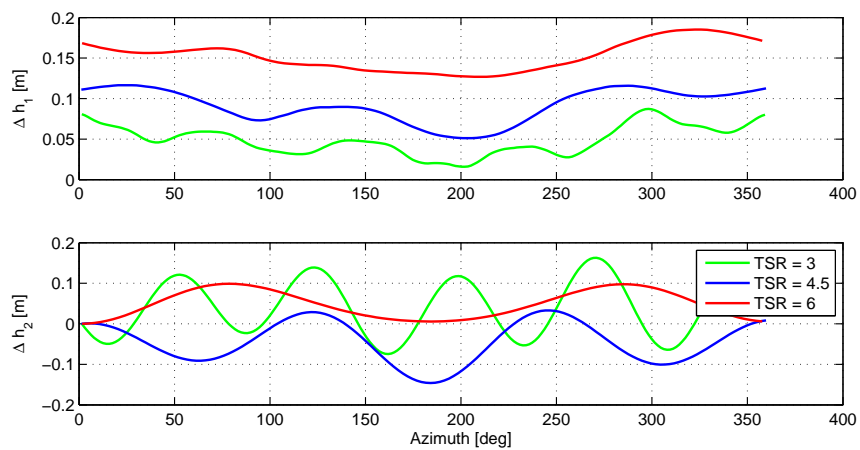
Figure 4.9: Displacement versus time of designed blade at the mid-span position



(a) NACA 0015-35 CFRP



(b) NACA 0015-40 CFRP



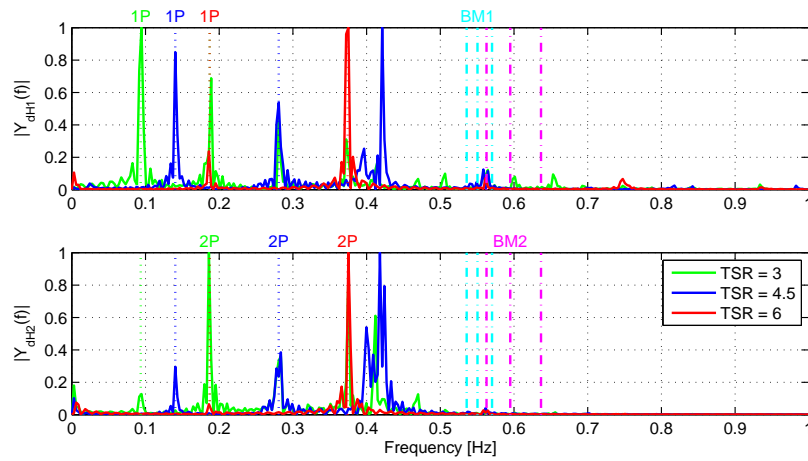
(c) NACA 0030 GFRP

Figure 4.10: Displacement averaged for one revolution of designed blade at the mid-span position

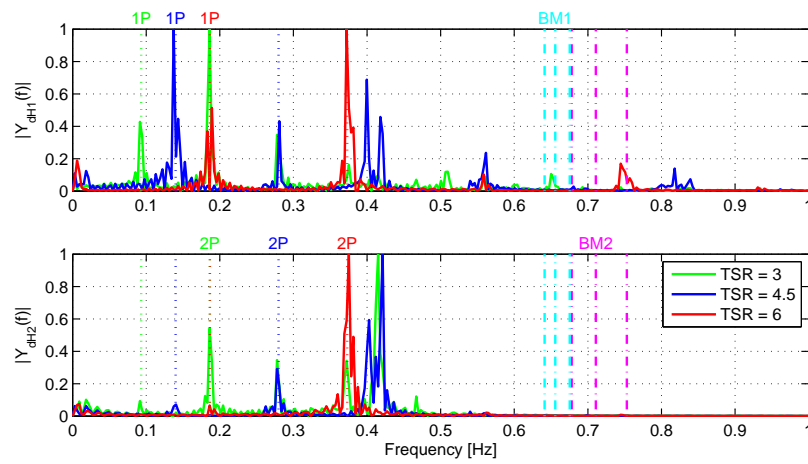
Figure 4.11c it can be seen that at a TSR of 6 the displacements, the eigenfrequency and the multiple of the operational speed are altogether close to the same frequency of 0.364 Hz. This situation will be critical as it can lead to resonance. An additional discussion can be found in subsection 5.1.3.

4.4 Campbell Diagram

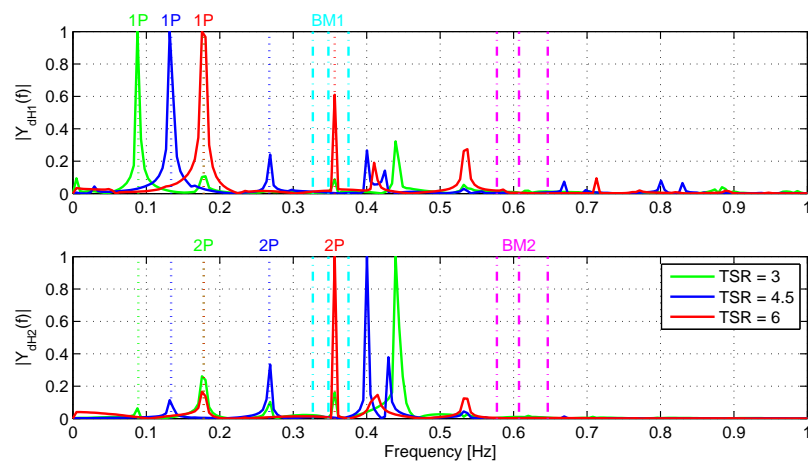
Through the Fourier analysis, the frequencies of the deflections were determined. The frequencies, which appear the most are included into the Campbell diagram of the rotor. The blade modes (BM) corresponding to the displayed eigenfrequencies can be found in Appendix G. The displacement frequencies are labeled with $dH1$ and $dH2$ corresponding to the displacement in flap-wise and edgewise direction. The frequencies of the multiples of the operational speed have been neglected, in order to not include the frequency of the excitation forces. It can be noticed that the frequencies of the aeroelastic simulations are below the eigenfrequencies determined through M. Schelbergen [62]. Additionally, the frequencies of the simulations have a descending trend, apart from all eigenfrequencies. An explanation can be found in subsection 5.1.4.



(a) NACA 0015-35 CFRP

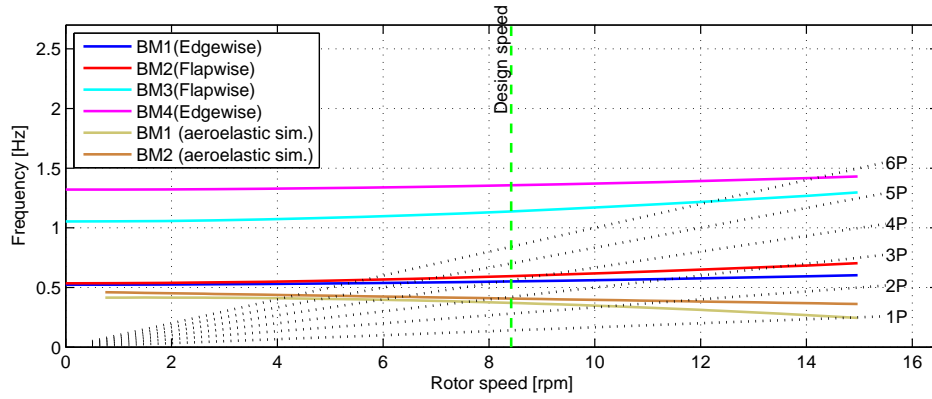


(b) NACA 0015-40 CFRP

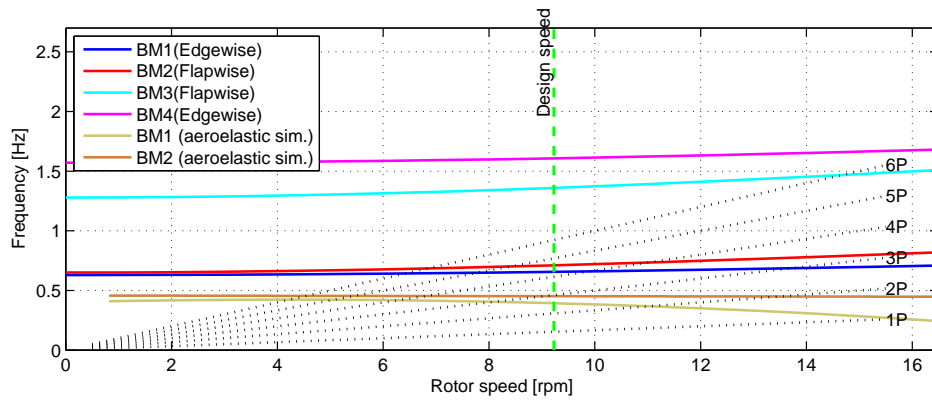


(c) NACA 0030 GFRP

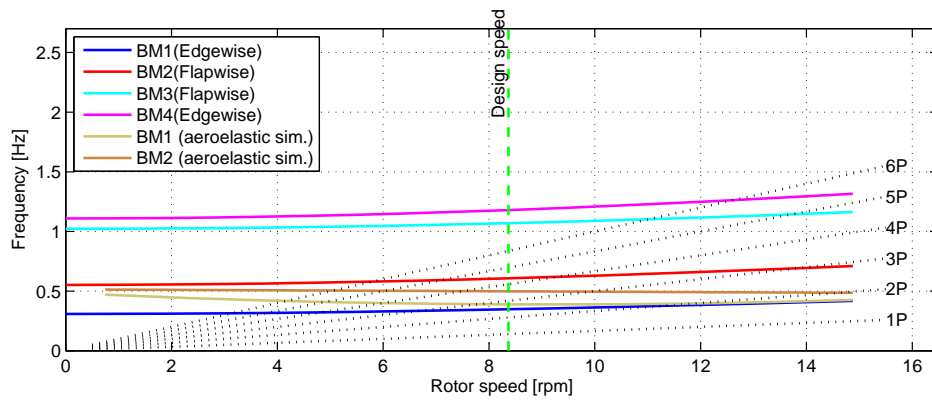
Figure 4.11: Fourier analysis of displacement (given in Figure 4.9) of designed blade at the mid-span position



(a) NACA00XX CFRP



(b) NACA00ZZ CFRP



(c) NACA0030 GFRP

Figure 4.12: Campbell diagram of the designed blade including the displacement frequencies of the mid-span position

4.5 Power Coefficient Curves Of Optimized Rotor Blades

Normal and tangential forces are dependent on the airfoil and the blade location. Through Troposkein shape, these forces vary and cannot simply be extrapolated from the equatorial plane. In this thesis, 25 blade locations were considered. The forces were interpolated along the span to obtain a representative power coefficient. The values can be found in Figure 4.13. As a comparison C_P curves are included, where the designs are considered to be rigid. Two offsets can be observed. The first one is between a TSR of 2 and 3. The second one at a TSR of 6, where the power coefficient drops suddenly. An exception is the curve of the NACA0030 (GFRP), which almost completely overlaps with the stiff curve. Subsection 5.1.5 contains a detailed discussion about these curves.

4.6 Up-Scaling Of Optimized Rotor Power Output

The best design (NACA 0015-40 with CFRP) is used in an up-scaling towards Multi-Megawatt dimensions. A GFRP analysis was not considered as the designs had issues with panel buckling. In Figure 4.14, the dotted black line is determined by M. Schelbergen [62]. The blue line is the result of the adapted optimizer. Additionally, some HAWT designs are included for a comparison between VAWT and HAWT. The HAWT designs are:

- NREL's 5 MW reference turbine [30]
- Vestas v164-8.0 [71]
- DUT's 10 MW reference turbine [18]
- SNL's 100 m blade [12]

It can be seen that the adapted optimization code produces designs that are competitive. However, it needs to be stated that the HAWT-design are based either on pure GFRP approach or on a mixture of materials.

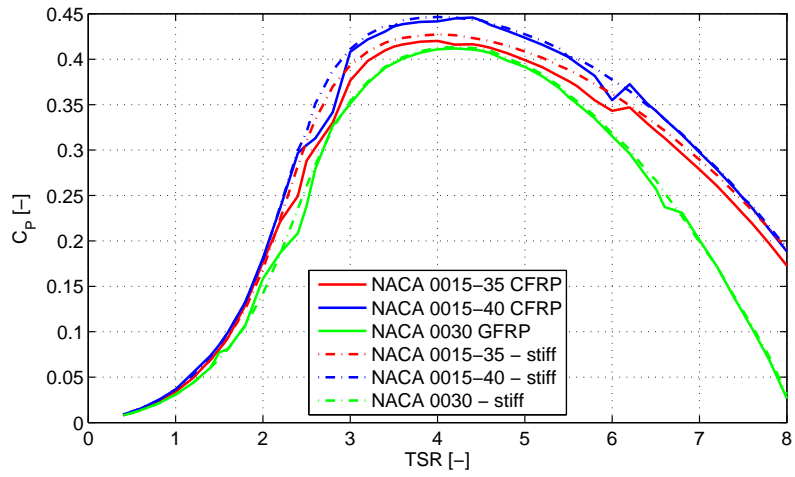


Figure 4.13: C_P versus TSR curve of designed blade

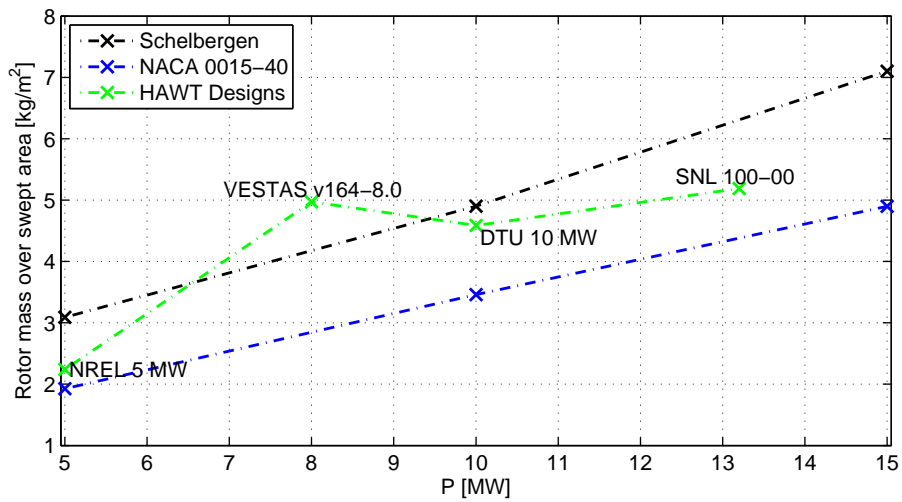


Figure 4.14: Scaling trend of VAWT rotor blades and HAWT designs [12, 18, 30, 71]

Discussion And Critical Review Of The Optimization Results

For this discussion firstly, the results of chapter 4 will be evaluated and judged in section 5.1, followed by a critical review of the simulation results in section 5.2. Lastly, an outlook on the possible improvements of the optimization code and of the aerolastic coupling will be given in section 6.2.

5.1 Discussion

5.1.1 Optimization Results

The developed optimizer aimed to obtain designs with the lowest mass to area ratio. This goal was achieved through varying the blade geometry, and the internal structural design. A trend was expected, that a thicker airfoil will result in a rotor with a lower mass to area ratio than a thin airfoil. This prediction was not always observed. It needs to be stated that all designs have resulted in different areas. However, the area was not the main driver of the function values, which lead to the fact that the area did not influence the further analysis. In both curves in Figure 4.1 it can be noticed that towards the thin airfoil the curve a has lower absolute gradient than the one after NACA 0020. For the case of a rotor with a single NACA 0015 airfoil along the span, it was not possible to find any design that does not violate the optimization constraints. Another interesting design is the rotor with varying blade section is the NACA 0018-35, which violates the design constraints too. A closer inspection showed that the violation has a value of $6.65 \cdot 10^{-3}$. This means that it crosses the constraint slightly and can be assumed as a valid design. The adapted optimization code indicated a lower mass to rotor area ratio than the initial design of M. Schelbergen [62] and the DeepWind concept [24]. However it needs to be stated that the DeepWind concepts was designed at a rated speed of 14 m/s, leading to higher loads during operation and a lower rotor area.

The m/A of the rotor with GFRP and constant blade section of a NACA 0030 is just slightly below the one of NACA 0035. This can be seen as a local minimum of the constant profiles. It was expected that the thick blade sections will have a lower function values. However, after a certain size, the thickness leads to more mass and thereby imbalance of the beneficial structural integrity and its own weight. In Figure 4.1 the plus signs indicated that only three of the GFRP blades did not violate the constrains. All other design points experienced panel buckling. The panel between trailing edge and shear web had a high likelihood of buckling. Unfortunately, this also happened with the variable blade sections. Such an issue might either occur from the shell model of Nastran. In reality the cross-section consists of multiple layers of material, forming a sandwich panel. Depending on the lay-up and thickness of the single layers, the structural properties change. In Nastran this panel is discretized as a shell, which includes all layers. During the optimization the thickness of the entire sandwich is altered, while it might be necessary to only vary one layer, such as the core. This could be solved through either recalculating the composition of the shell, adding more variations of the shell structure or by relocating the shear webs, to reduce the loads on the skin panel. Additionally, it can be noticed that the GFRP curve is similar to the CFRP results, besides the different magnitudes. This is because of the additional cross-section thickness that is required to counter the lower Young's Modulus of GFRP.

The swept area shown in Figure 4.3, is determined through the blade topology given in Figure 4.4. As it can be seen all swept areas are inside the area constrains, preventing physical unfeasible designs, where the rotor radius goes to infinity. It can be said that all designs are in the range of a 5 MW rotor area and might only require a different rated speed. Some of the CFRP design have a kink in the bottom region around $z = -70$ m. Such a kink might result out of the initial shape and the applied area constrain. It is possible that this phenomena vanish with a different starting shape. Nevertheless this kink was observed to be a stress concentration, because this region is carrying the weight while the turbine is parked and is deflecting outwards during operation.

The stresses can be obtained from the aerodynamic, the inertial and gravitational loads. Especially during the parking condition, the blade weight is a critical design factor. The CFRP design with a variable blade section of a NACA 0040 towards a NACA 0015 is considered during further investigations, because it had the lowest function value. Additionally, the NACA0015-35 (CFRP) and the GFRP design, using a constant NACA 0030, are included. The NACA0015-35 is chosen, following from the second lowest function value. The constant NACA 0030 (GFRP) is added as the lowest function value without a constrain violation.

5.1.2 Stress And Fatigue

After the selections of designs had been narrowed down, section 4.2 displays a closer inspection of the chosen points. In Table 4.1 it can be seen that every design has a buckling failure index close to 1.0 and a fatigue damage above 1.0. In case of the GFRP design the buckling failure index is even above one, which explains the violation of constraints. Therefore it can be extracted that buckling and fatigue are the main design drivers during

a Troposkein blade design process.

The CFRP rotor design with variable blade section NACA 0035 to NACA 0035 has two critical areas that can be allocated along the blade in Figure 4.6a: close to the root and in the top region next to the leading edge. The root regions are the connections towards the tower and have to carry the entire blade weight, leading to high reaction forces. The blade is so flexible that if the turbine changes from parked to rotating conditions, the layout will be pushed up- and outwards while compressing the inner side, leading to the displayed stress concentration at the second point. Additionally, the thickness is rather low as seen in Figure 4.5a. Around the equatorial region it can be noticed that the cross-section are increased in thickness in order to sustain the normal forces during operation. The fatigue damage of this design can be found in Figure 4.6b. These three points will have the highest probability of breaking as a result of fatigue.

The rotor design (NACA 0015-40 with CFRP) has similar critical points. The only difference in Figure 4.7a is that at the root region and at the equator the trailing edge and its connected panel is likely to buckle. This also explains the higher fatigue damage on the skin than on the girder, as seen in Figure 4.7b. The critical region remains in the upper half on the top site, where the loads concentrate during the variation from parking to operational. Also this point has the lowest thickness along the entire blade span (Figure 4.5b).

The critical regions of the rotor design (NACA 0030 with GFRP) are shown in Figure 4.8a. The failure index exceeds 1.0 at the equatorial region and at the panel connected to the trailing edge of the lower part. This means that the design is likely to buckle. Composite materials like GFRP, only have a small elastic deformation region, which means that if the material buckles it will also fail. The critical regions in Figure 4.8b are similar to the one inspected, except the root regions. But the fatigue damages are relatively small, which would mean that the design could sustain longer. Nearly every blade made with GFRP showed a likelihood to buckle and low fatigue damage. The results will become more accurate if another S-N curve is used. The buckling results will vary if a *panel* calculation instead of a *shell* structure is used. This leads to a different setup of the load calculation, that is more representative.

5.1.3 Aeroelastic Evaluation

Overall, the aeroelastic simulations show the deflection in the flapwise direction (ΔH_1) are almost equal to the ones in edgewise direction (ΔH_2). In Figure 4.9 and 4.10 it can be noticed, that the deflections are higher when the TSR is high. The GFRP design is an exception, as the amplitude of the deflections in H_1 are greater at lower TSR. At this point the frequency of the deflections are close to the second blademode, therefore close to a resonance.

Additionally, it can be noticed that none of the simulations indicate a diverging flutter motion, ensuring a safe operation. However, the simulations only considered a logarithmic wind shear without any turbulence, that might effect the stability of the blade. The deflections with an amplitude of 0.5 m appear close to the first eigenfrequency of NACA 0015-40 CFRP. Therefore it should be avoided to run the optimized blade at such high

TSR or to include an active control mechanism to counter these motions. Nevertheless it can be mentioned that these amplitudes are less than 1% of the rotor radius, which is rather low.

While inspecting Figure 4.10 it is possible to obtain the averaged displacements. The values are measured with respect to the position of a stiff blade, such that a positive deflection is an indication of an outward motion in H_1 and a lagging motion in H_2 . A lagging edgewise motion occurs due to the drag force on the blade. The flexible blade leads to a phase shift of the azimuth position with respect to the original position. This aspect has to be kept in mind while observing the motion in H_2 .

Figure 4.9b needs to be discussed in more detail. The growing and declining oscillations imply that two frequencies which are close to each other start to interact. Both frequencies are unequal to the eigenfrequencies as seen in Figure 4.11b. However, at the TSR of 6 the first eigenfrequency of the NACA 0015-40 is almost coinciding to the $3P$. Therefore the oscillation indicate the beginning of resonance, which could end fatal.

These motions are in relation with the operational speed, as seen in Figure 4.11. The Fourier analysis returns that the frequencies with the highest probability are either the operational frequency or a multiple of it. This makes sense as the exciting forces are obtained through the aerodynamic load, depending on the azimuth angle. Mostly at a low rotational speed, the blade perceives other frequencies, following from the main contribution through gravity, which makes the eigenfrequency more accessible.

5.1.4 Campbell Diagram

The determined frequencies had been entered in the Campbell diagram, which displays all eigenfrequencies of the blade at different rotational speeds. The dotted lines in Figure 4.12 are representative of operational speed of either one blade ($1P$) or the multiples of it (xP).

It is noticeable that the eigenfrequencies are relatively high with respect to the blade frequency of a HAWT [31]. This situation follows from the boundary conditions, that are applied in Nastran. It is assumed that the blade roots are not capable of moving. This is only achievable if either the blade roots are fixed in space or if the tower is infinitely stiff.

The first two blade modes of the CFRP designs, are very close to each other. The modes only cross the $3P$ line, which means that the eigenfrequencies do not overlap with the operational regime, marked through the vertical green line. The GFRP design has even lower frequencies. The first blade mode even crosses the $2P$ line at a speed of 11.3 rpm. Such rotational speed could be reached in multiple ways, such as:

- Increasing the rotational speed to a TSR of 6.08 with a radius of 61.615 m and a wind speed of 12 m/s
- An inwards deflection to a radius of 45.6 m at a TSR of 4.5 and a wind speed of 12 m/s
- An increase of the wind speed of 16.2 m/s, with a TSR of 4.5 and $R = 61.615m$

The most likely solution would be that the wind speed increases to 16.2 m/s through a gust, while the TSR is constant. During operation this should be kept in mind and avoided, by keeping the rotational speed constant and thereby decreasing the TSR at this point. Additionally, it can be seen that the displacement frequencies are partially overlapping with the operational speed.

The frequencies obtained through the aeroelastic simulations are mostly below the eigenfrequencies of the designed blade. The difference between the curves is because that blade roots are not fixed in space during the aeroelastic simulation and thereby shifting the frequencies downwards. It can be noticed that the frequencies are descending at higher TSR, following from a centrifugal softening. An exception is the frequency of ΔH_1 of the NACA 0030 GFRP design, where the frequency increases with the TSR.

The Campbell diagram can be also used to determine the required eigenfrequency of the, to not have the frequencies overlapping or inside the operational regime. A wise choice will be to design a *stiff-stiff* tower such that the assumptions of the blades being fixed in space is valid. However, in reality the tower cannot be so rigid that the blades are fixed in space. Therefore it should be considered to adapt the boundary conditions of the Campbell diagram to include a non-rigid tower. This modification will lead another degree of freedom of the blade and therefore to lower eigenfrequencies.

5.1.5 Power Coefficient Diagramm

The designed blade can be evaluated on their efficiency, as seen in Figure 4.13. The most efficient design is the NACA 0015-40. Therefore the design with the lowest mass to area ratio is also the best performing. The offset to the NACA 0015-35 is following from the less thick airfoil at the root region. In this region the turbine is drag-driven as long as the local TSR is below 1.0.

In general it could be said, that the flexible blades have a lower performance than their stiff equivalent. The additional motions of the blade decrease the torque. An interesting region is around the TSR of 2 till 3. Inside this region centrifugal stiffening and centrifugal softening interact with each other and leading to fast oscillations of the blade. Another point of interest is at a TSR of 6.0, where eigenfrequencies are close to the operational speed. A similar behavior can be observed with the NACA 0015-35, where the only difference is that the offset between stiff and flexible blade is more obvious around the design TSR of 4.5. The GFRP NACA 0030 has an almost identical curve as its stiff version, meaning that the NACA 0030 is only slightly flexible.

It becomes obvious that the choice of airfoil is the leading factor of the efficiency. So it is possible to increase the C_p . If the root section is reduced in thickness, the weight will go up by 4000 kg to reinforce the structure. With CFRP this additional weight costs 80 000 € (assuming 20 €/kg [14]). The same can be checked with the GFRP design. The NACA 0030 blade has a mass of 51855.6 kg, being thereby half as expensive as the CFRP designs, when assuming a price of 5.18 €/kg [14]. On the other hand a lighter blade leads to a lighter support structure and so to less investment cost. The best option would be to include a mixture of materials and a possible third shear web such that a

light blade without the possibility of panel buckling can be developed. A list of further aspects requiring inspection is given in the section 6.2.

5.1.6 Up-Scaling Trend Of VAWT Rotor

Lastly the best design, the NACA 0015-40, is used during an evaluation of a 10 and 15 MW design. Figure 4.14 displays the original curve determined by M. Schelbergen [62] and the results of the adapted version. Both curve have a linear trend. But the gradient of the modified optimizer is lower. The longer the blade and the same amount of design sections, the more mass reduction can be achieved, by interpolating the thicknesses of the cross-section member.

Additionally, a comparison between four HAWT-configuration is presented. The only existing turbine is the Vestas v164-8.0, the other turbines are reference turbines, designed by research institutions. It can be noticed that the trend of Schelbergen's design is similar to the HAWT designs. The new trend scales up slowly such that a VAWT is more favorable in the Multi-Megawatt region. It only needs to be kept in mind that the VAWT is assumed to be out of CFRP. The HAWT designs are a combination of multiple materials to reduce their cost.

5.2 Critical Review Of Results

In the optimization procedure two results should be examined with care and in detail. The first one is the entire series of the GFRP designs. Mentioned earlier, it was not possible to find a design, which does not violate the buckling constrain. This situation is probably following from the choice of the composite panel. A method to counter this situation will be to increase the core thickness, for example by adding more balsa wood to the core. Additionally, it was noticed that the calculation of the fatigue damage of GFRP produced lower values than with CFRP, while at the same time the design is buckling. Such results are either obtained through the difference of material, from a wrong stress ratio or because of the used S-N curve approximation. The load handling of composites is highly dependent on the orientation of the fibers, as they are non-unidirectional. A single S-N curve as a representation is a rather rough method. It will be better to include multiple curves describing multiple fiber orientation.

The NACA 0018-35 made with CFRP is another optimization result that raises awareness. The objective function value was higher than the other transient designs by a 0.4 kg/m^2 and it violates the stress constrain along the shear web in the root region. It seems not logical that this design is not feasible as the design does not vary that much from the others. A thicker profile has more resistance against the bending moment. A possible cause could be a wrong starting point, where the optimization algorithm is captured at a local minimum and is not capable of overcome the descending trend of the design space.

Lastly, the displacements in edgewise direction H_2 are almost the same magnitude than in the flapwise direction. This would mean that the blade is as stiff along the chord than

along the flapwise direction, which is mostly the flexible direction of HAWT-blades. A possible reason for such a behavior could be following from the used models. It might be that the edgewise stiffness is not correct, or the determination of the deflections is based on a wrong azimuth angle, required to transform the blade position from the Cartesian system into the blade fixed coordinate system. Currently, the azimuth angle is estimated through its initial position at $t = 0$ and the product of rotational speed and time. However it can be said that magnitudes of the deflections of the blades are rather small with respect to the overall rotor radius.

Conclusions And Further Perspective

This chapter contains a conclusion on the entire thesis' objective and ends with possible topics of further investigations.

6.1 Conclusions

A design with a low mass to area ratio is achieved through CFRP and a changing blade cross-section from a NACA 0040 at the roots towards a NACA 0015 at the equator. Unfortunately, the designs made out GFRP had a high likelihood of panel buckling.

Thick NACA 4-digits airfoils have a high drag coefficient. Allocating these airfoils at the roots leads to a reduction of the angle of attack and therefore to a lower drag. Additionally, the structural integrity of the thick airfoils can be used to their full potential. An aeroelastic analysis showed that the displacements of the blade increased with the tip speed ratio. These deflections had an amplitude of 0.5 m in flap- and edgewise direction. The edgewise motion indicated a backwards phase shift with respect to the angle measured in the root region. Nonetheless, the blade did not indicate any increasing deflection, which would cause a blade failure. Additionally, maximum power losses of 5% were observed due to the flexibility of the blade. However, the designed blades showed a satisfying scaling trend that had a better mass over area ratio than some HAWTs.

All in all, it can be said that a rotor design with thick blade sections at the root and thin blade sections at the equator is beneficial from an aerodynamic point of view as well as from a structural one. This concept also proved to be aeroelastically stable. Furthermore, the designed blade did not have any resonance issues over a wide range of rotational velocities, due to the high eigenfrequencies. All this together ensures a safe usage.

6.2 Further Research

Throughout the development of this thesis, topics have been identified that require further investigation. A brief overview can be found in the following subsections.

6.2.1 Optimization Improvement

- *Variable blade section thickness along the blade span*
Currently, the code allows a change of the blade section thickness by using fixed values. As it was noticed during the optimization, a change of these values will lead to a different result. Therefore a variable value would lead to an even better design instead of the designs obtained through fixed values. Additionally, it was proposed that the thickness could be increased to a height of 50% of the chord length, in order to use the drag beneficially. It only needs to be considered that the drag part is limited to a region where the local TSR is below 1.0, to avoid a performance loss.
- *Variable chord length*
Next to an alternating thickness, the chord could also be varying from root to equator. Initially this could be done with fixed values, such as it was done with the airfoil thickness. In a further development the chord of each section could be modeled as another design variable. While implementing them, a geometric relation should be used, to limit the amount of design variables and thereby bounding the calculation time.
- *3rd shear web*
While using GFRP it was noticed that panel buckling is an issue. This can be resolved by including a third shear web further in the direction of the trailing edge. Unfortunately, this approach has a drawback. A CG closer or behind the elastic axis decreases the stability of divergence [28]. Additionally, it might be considered to neglect the buckling constrain based on the fact that shell model of Nastran is not representative enough.
- *Individual thickness of each airfoil part*
At this instance the optimization code determines the thickness of shear web, skin and girder. Those values are applied to all members of the cross-section. In this way the skin thickness of the upper panel is equal to all other skin parts, which means that the leading edge might be over-designed and could be reduced to save mass.
- *Allowing different materials*
Most of the designed blades consist out of several materials. Therefore it will be necessary to modify the code such that each part of the cross-section is assigned to its individual material configuration, e.g. a skin out of GFRP and a girder out of CFRP.

Some of these improvements will lead to additional design variables. The amount of these variables should be limited to restrain the computational time. Additionally, if more variables are included, the domain becomes more complex and could contain more local optima. This will make the search for a global optimum more difficult.

6.2.2 VÆMPS Improvement and Debugging

During the aeroelastic simulation of the SNL 34m Testbed, the displacements of the equatorial blade section, determined through VÆMPS and HAWC2, did not coincide (section 3.5). Still, in the *SpecialProject* [61] it was seen that the aerodynamic forces were similar to each other. Therefore it is necessary to debug VÆMPS further. The main points that need to be considered, can be summarized as following:

- *Checking structural component*
Throughout the *Special Project* the aerodynamics were checked without the influence of structural deformation. The same should be done with the dynamic structural solvers of VÆMPS and HAWC2. This can be achieved by neglecting the coupling and evaluating their individual output.
- *Checking a simpler geometry*
A Troposkein design is a rather complex design, as the forces not only point in tangential and radial direction, but also in the z-direction (*H3*-direction). This is a limitation of the Actuator Cylinder model, used in HAWC2. Therefore a test case with an H-rotor has to be considered, to neglect the influence of the blade geometry.

In addition to the error revision, the aeroelastic solver also requires some adjustments that could improve its performance and accuracy.

1. *Reducing computational time*
The aerodynamic solver is memory intense and requires a long computational time. One method, reducing the intensity would be by searching for redundant variables and inefficient loops.
2. *Including blade deflection in the wake update*
The current state of VÆMPS uses the wake motion only during the determination of the inflow and the angle of attack. But the blade motion and deflection will influence the wake development and thereby the induced velocities. Due to that, the blade motion should be updated.

These points carry the risk of numerical instabilities of the aerodynamic code, especially the last one. The solver will have a non-singular solution, if the blade is deformed such that the wake filament occurs inside the cross-section. Such aspects should be kept in mind during the further development.

6.2.3 Additional Research Topics

- *Comparison of optimization results with NACA 4-digit airfoils and VAWT airfoils*
Only the NACA 4-digit airfoils have been considered for a blade design. Some of the participating institutes already designed airfoils that are only considered for VAWT configurations. These airfoils will have a higher power output and could lead to a rotor design with a lower mass over area ratio.

- *Difference in aeroelastic behavior between Near-Wake analysis and Actuator Cylinder*

After the near wake aeroelastic simulation is completely debugged, a comparison between the HAWC2 and VÆMPS will be required in more detail. It should be inspected whether the near-wake solver leads to a significant difference of the blade motion and fatigue damage.

- *Reduction of mass through supporting struts*

During the optimization it was assumed that the Darrieus blades are self-bearing. If struts were included in the bottom and top region, the blade weight would be reduced even further. However, the struts increase the drag on the blade and disturb the flow. This will lead to a lower efficiency of the turbine. If the support is placed in the region where the local TSR is below 1.0, the thereby created drag can be used during power production and even as start-up mechanism.

- *Development of a VAWT comparison test case*

During the comparison of the models, it became clear that there is no standardized comparison model. For HAWTs this model is mostly the NREL 5 MW turbine. But in case of VAWTs it is not that obvious. Some codes use a fictitious turbine, other ones refer to the Sandia 34m Testbed or to the DeepWind project, making a comparison between different papers problematic. In the future one standard model should be developed, that can act both as a comparison base and as an initial design point for new VAWT designs.

Appendix A

Force Transformation

Lift and Drag act perpendicular and parallel in the direction of the apparent velocity. It is required to transform them into normal and tangential force, which are dependent on the angle of attack. The forces can be defined as written below. In order to save space sine and cosine are abbreviated with s and c.

$$N = L \cos(\alpha_{tot}) + D \sin(\alpha_{tot}) \quad (\text{A.1})$$

$$T = L \sin(\alpha_{tot}) - D \cos(\alpha_{tot}) \quad (\text{A.2})$$

$$\begin{aligned} N = L [& c(\alpha) c(\theta) c(\Delta\alpha_{\dot{\zeta}}) c(\Delta\alpha_{\dot{\eta}}) - c(\alpha) c(\theta) s(\Delta\alpha_{\dot{\zeta}}) s(\Delta\alpha_{\dot{\eta}}) \\ & -s(\alpha) s(\theta) c(\Delta\alpha_{\dot{\zeta}}) c(\Delta\alpha_{\dot{\eta}}) + s(\alpha) s(\theta) s(\Delta\alpha_{\dot{\zeta}}) s(\Delta\alpha_{\dot{\eta}}) \\ & -s(\alpha) c(\theta) s(\Delta\alpha_{\dot{\zeta}}) c(\Delta\alpha_{\dot{\eta}}) - s(\alpha) c(\theta) c(\Delta\alpha_{\dot{\zeta}}) s(\Delta\alpha_{\dot{\eta}}) \\ & -c(\alpha) s(\theta) s(\Delta\alpha_{\dot{\zeta}}) c(\Delta\alpha_{\dot{\eta}}) - c(\alpha) s(\theta) c(\Delta\alpha_{\dot{\zeta}}) s(\Delta\alpha_{\dot{\eta}})] \end{aligned} \quad (\text{A.3})$$

$$\begin{aligned} & +D [s(\alpha) c(\theta) c(\Delta\alpha_{\dot{\zeta}}) c(\Delta\alpha_{\dot{\eta}}) - s(\alpha) c(\theta) s(\Delta\alpha_{\dot{\zeta}}) s(\Delta\alpha_{\dot{\eta}}) \\ & +c(\alpha) s(\theta) c(\Delta\alpha_{\dot{\zeta}}) c(\Delta\alpha_{\dot{\eta}}) - c(\alpha) s(\theta) s(\Delta\alpha_{\dot{\zeta}}) s(\Delta\alpha_{\dot{\eta}}) \\ & +c(\alpha) c(\theta) s(\Delta\alpha_{\dot{\zeta}}) c(\Delta\alpha_{\dot{\eta}}) + c(\alpha) c(\theta) c(\Delta\alpha_{\dot{\zeta}}) s(\Delta\alpha_{\dot{\eta}}) \\ & -s(\alpha) s(\theta) s(\Delta\alpha_{\dot{\zeta}}) c(\Delta\alpha_{\dot{\eta}}) - s(\alpha) s(\theta) c(\Delta\alpha_{\dot{\zeta}}) s(\Delta\alpha_{\dot{\eta}})] \\ T = L [& s(\alpha) c(\theta) c(\Delta\alpha_{\dot{\zeta}}) c(\Delta\alpha_{\dot{\eta}}) - s(\alpha) c(\theta) s(\Delta\alpha_{\dot{\zeta}}) s(\Delta\alpha_{\dot{\eta}}) \\ & +c(\alpha) s(\theta) c(\Delta\alpha_{\dot{\zeta}}) c(\Delta\alpha_{\dot{\eta}}) - c(\alpha) s(\theta) s(\Delta\alpha_{\dot{\zeta}}) s(\Delta\alpha_{\dot{\eta}}) \\ & +c(\alpha) c(\theta) s(\Delta\alpha_{\dot{\zeta}}) c(\Delta\alpha_{\dot{\eta}}) + c(\alpha) c(\theta) c(\Delta\alpha_{\dot{\zeta}}) s(\Delta\alpha_{\dot{\eta}}) \\ & -s(\alpha) s(\theta) s(\Delta\alpha_{\dot{\zeta}}) c(\Delta\alpha_{\dot{\eta}}) - s(\alpha) s(\theta) c(\Delta\alpha_{\dot{\zeta}}) s(\Delta\alpha_{\dot{\eta}})] \end{aligned} \quad (\text{A.4})$$

$$\begin{aligned} & -D [c(\alpha) c(\theta) c(\Delta\alpha_{\dot{\zeta}}) c(\Delta\alpha_{\dot{\eta}}) - c(\alpha) c(\theta) s(\Delta\alpha_{\dot{\zeta}}) s(\Delta\alpha_{\dot{\eta}}) \\ & -s(\alpha) s(\theta) c(\Delta\alpha_{\dot{\zeta}}) c(\Delta\alpha_{\dot{\eta}}) + s(\alpha) s(\theta) s(\Delta\alpha_{\dot{\zeta}}) s(\Delta\alpha_{\dot{\eta}}) \\ & -s(\alpha) c(\theta) s(\Delta\alpha_{\dot{\zeta}}) c(\Delta\alpha_{\dot{\eta}}) - s(\alpha) c(\theta) c(\Delta\alpha_{\dot{\zeta}}) s(\Delta\alpha_{\dot{\eta}}) \\ & -c(\alpha) s(\theta) s(\Delta\alpha_{\dot{\zeta}}) c(\Delta\alpha_{\dot{\eta}}) - c(\alpha) s(\theta) c(\Delta\alpha_{\dot{\zeta}}) s(\Delta\alpha_{\dot{\eta}})] \end{aligned}$$

Some of those angles could be seen as small angles, which then simplifies the equations as given below. It is assumed that $\Delta\alpha_{\zeta}$, $\Delta\alpha_{\eta}$ and θ are so small such that the small angle approach can be used ($\sin \alpha \approx \alpha$ and $\cos \alpha \approx \alpha$).

$$\begin{aligned}
N = L & \left[\theta \left(s(\alpha_0)(-1 + \Delta\alpha_{\zeta}\Delta\alpha_{\eta}) - \Delta\alpha_{\eta}c(\alpha_0) \right) \right. \\
& \left. + c(\alpha_0)(1 - \Delta\alpha_{\zeta}\Delta\alpha_{\eta} - \Delta\alpha_{\eta}) - s(\alpha_0)(\Delta\alpha_{\zeta}\Delta\alpha_{\eta} + \Delta\alpha_{\eta}) \right] \\
+ D & \left[\theta \left(c(\alpha_0)(1 - \Delta\alpha_{\zeta}\Delta\alpha_{\eta}) - c(\alpha_0)(\Delta\alpha_{\zeta} + \Delta\alpha_{\eta}) \right) \right. \\
& \left. + s(\alpha_0)(1 - \Delta\alpha_{\zeta}\Delta\alpha_{\eta}) - c(\alpha_0)(\Delta\alpha_{\zeta} + \Delta\alpha_{\eta}) \right]
\end{aligned} \tag{A.5}$$

$$\begin{aligned}
T = L & \left[\theta \left(s(\alpha_0) \left(\Delta\alpha_{\zeta} - \alpha_{\eta} \right) - c(\alpha_0) \left(1 + \Delta\alpha_{\zeta}\Delta\alpha_{\eta} - \Delta\alpha_{\zeta} \right) \right) \right. \\
& \left. + s(\alpha_0) \left(1 - \Delta\alpha_{\zeta}\Delta\alpha_{\eta} \right) - c(\alpha_0)\Delta\alpha_{\eta} \right] \\
- D & \left[\theta \left(s(\alpha_0) \left(\Delta\alpha_{\zeta}\Delta\alpha_{\eta} - 1 \right) - c(\alpha_0) \left(\Delta\alpha_{\zeta} - \Delta\alpha_{\eta} \right) \right) \right. \\
& \left. + c(\alpha_0) \left(1 - \Delta\alpha_{\zeta}\Delta\alpha_{\eta} \right) - s(\alpha_0) \left(\Delta\alpha_{\zeta} + \Delta\alpha_{\eta} \right) \right]
\end{aligned} \tag{A.6}$$

Appendix B

Parameter Study On A NACA 0018 Airfoil

As in aeroelastic the flow conditions around an airfoil are changing it should be inspected on how the airfoil characteristics changes in a changing environment. The investigation was done on a NACA 0018, which was used in the Sandia 34m Test bed. The Study will have three main parameter that will be changed. The first one is the Reynolds number followed by an elongation of the chord. The last evaluation is focused on the effect of panel buckling, as large wind turbines are more likely to have panel buckling.

Influence of the Reynolds number

The Reynolds number is a scaling number in aerodynamics. It is an indicator how fast the flow crosses the an airfoil. The definition can be found in Equation (B.1).

$$Re = \frac{\rho \vec{v} L}{\mu} \quad (\text{B.1})$$

VAWTs operate on rotational plane, which is aligned with the wind speed. Following from that it becomes clear that the airfoil is some times rotating into the wind and otherwise against the wind, meaning that the apparent wind is changing in magnitude and direction. Due to the fact that the airfoil is rotating with a TSR higher then one, will mean the there is no flow reversal and the apparent wind speed always approaches on the leading edge.

But the magnitude changes and so the Reynolds number changes as well. Therefore it will be a good decision, to inspect the effect on the aerodynamic coefficients. The set up for this study was to run sequence of different angle of attack at different Reynolds number and let it analyze through XFOIL. The outcomes can be found in Figure B.1.

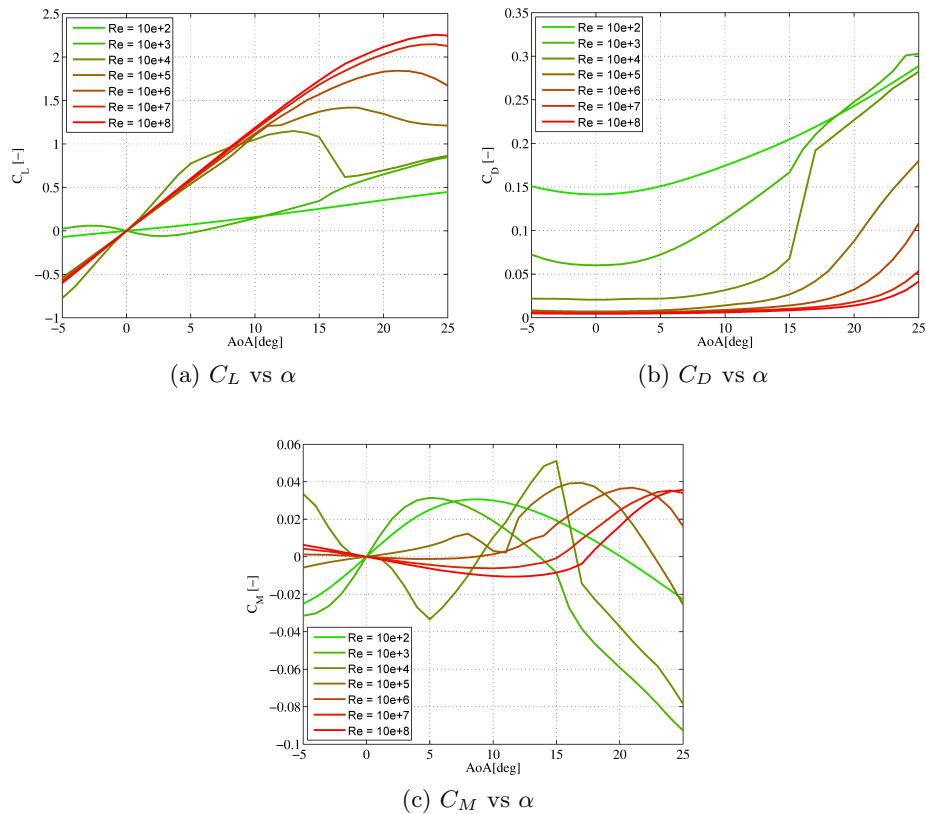


Figure B.1: Influence of Reynolds number on profile coefficient of a NACA 0018

In Figure B.1a it can be seen that the airfoil starts producing lift at Reynolds numbers above 10^5 . At lower regions the flow is close to a creeping flow [7]. At this kind of condition the airfoil is more of an obstacle than it is a lifting device. This is also observable in Figure B.1b. With an increasing Reynolds number the drag coefficient is reducing. Initially this decrease has a high change but at higher Reynolds numbers the variation decays. Figure B.1c displays the moment coefficient around the quarter chord. As for low Reynolds numbers, drag is the driving force, leading to a higher variation of the moment coefficient at different angle of attacks. What holds for all three coefficients is that at higher Reynolds numbers the change of values is lower. Resulting from that it can be said that in case of a VAWT it will be sufficient enough to use a look-up table along the operation range, as long as the table was made with the appropriate Reynolds number.

Influence of geometric stretching

The next study is evaluated on the airfoil geometry. During higher speeds the airfoil could be deformed, such deformation could be that the airfoil becomes thinner and therefore the chord elongates or the panels start to buckle. The situations are inspected at a Reynolds number of 10^8 . It is assumed that when the chord length is elongated, the thickness is reduced and the enclosed area remains constant. There two scaling factors

are defined, their relation can be found in Figure B.2a. It can be seen that the relation is inverse proportional to each other. As XFOIL prefers normalized coordinates the airfoils will be represented in that matter. When displaying on top of each other (Figure B.2b), it becomes clear that elongating the chord length by 120% the original NACA 0018 comes close to a NACA 0012. So basically this stretching is more a comparison between different thickness.

In Figure B.3 the aerodynamic coefficients outcome for the different thickness can be

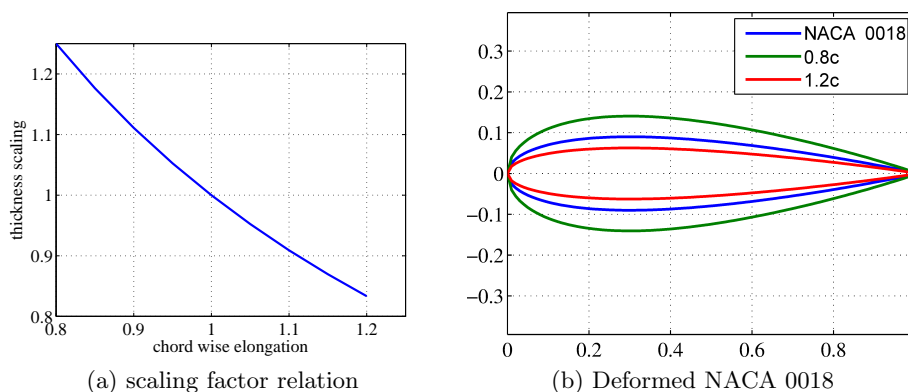


Figure B.2: Scaling of airfoil

found. For the lift curve the airfoil thickness does not have a significant difference. The thicknesses which were simulated are still in the region, where an airfoil can be assumed to be thin plate. This can be recognized by checking the slope of the curve, which is close to 2π . The drag coefficient (Figure B.3b) is influenced slightly influenced. It can be seen that when thickness is decreased also the zero-lift drag (C_{D_0}) goes down. At last it can be said that the more elongated airfoils, do have a smaller absolute value of the moment coefficient than the thicker airfoils. After 15° this phenomena is turned around. At this point the flow usually starts to separate, which explains the higher C_M for thicker airfoils.

Influence of upper Panel Buckling

The last influence which is taken into account is panel buckling. The set-up is similar to the one before. The main difference is that the chord length is unchanged but instead a theoretical spar is placed at $0.35c$, which will mean that the airfoil is only capable of having a buckling panel. For this inspection only the upper panel will be deformed, which is simulated with a second order polynomial. It is implemented that the trailing edge and the spar point have to be constant. In between these points the maximum deflection is located in the middle with a varying percentage of the chord length. The maximum deflections can be found in Figure B.4.

In Figure B.5 it can be seen that panel buckling has the largest effect on the aerodynamic properties. For the lift coefficient (Figure B.5a) the gradient of the curve is decreased as the buckling is more outboard. At the same instance is the stall angle shifted to higher

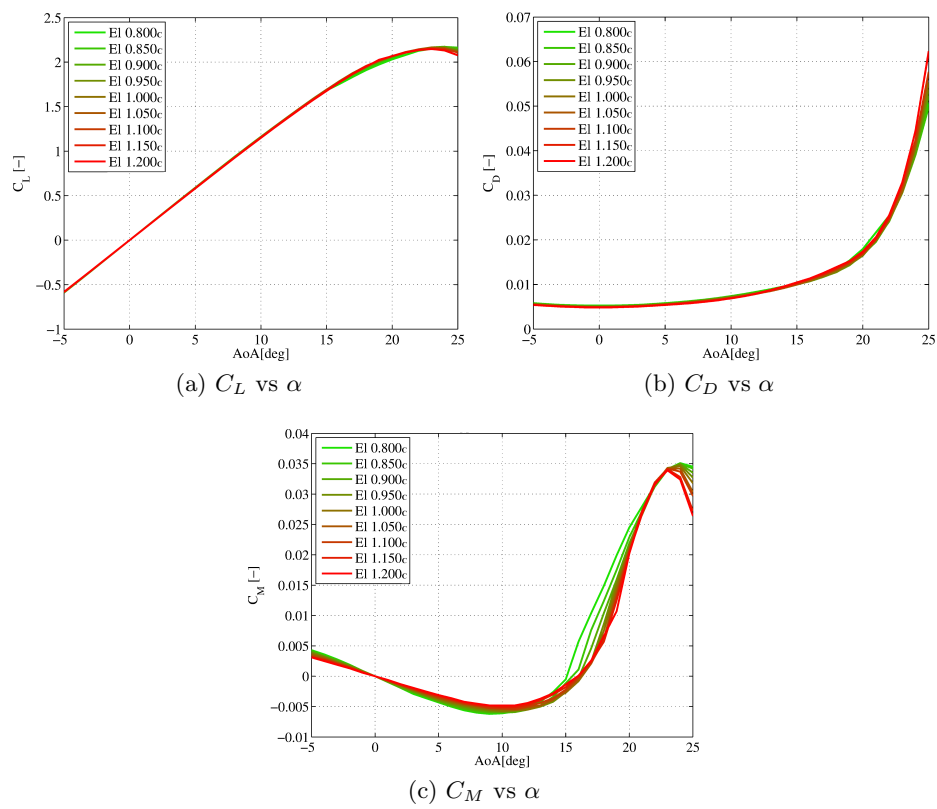


Figure B.3: Influence of chord elongation on profile coefficient of a NACA 0018

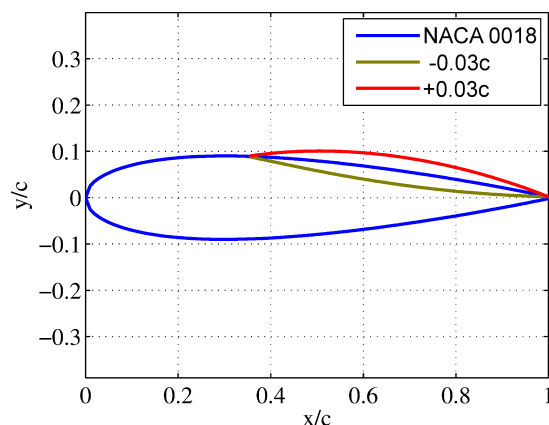


Figure B.4: Visualization of panel buckling with spar at $0.35c$

angle of attacks and the zero-lift angle is moved to lower angles. The drag coefficient (Figure B.5b) is nearly unchanged in below 10° . Afterwards the drag increases if the buckling is inside the airfoil. Lastly it can be recognized that the moment coefficient (Figure B.5c) is influenced the strongest. At high angle of attack it seems to converge to the same values. But during the operational range the moment coefficient is decreasing if the buckling bends out of the airfoil. When the buckling is inwards the airfoil is similar to the ones which are used in a flying wing [32]. In most wind turbine models, the airfoil is simulated as a rigid cross-section, which means that this behavior could be ignored during simulations. Nevertheless this has to be kept in mind and should be prevented during the design phase.

It can be concluded that during deformations of an airfoil, the aerodynamic properties do not vary significantly. Therefore it can be said that during aeroelastic simulation look-up tables could be used to obtain the wanted properties. The majority of the structural solvers use a beam model and assume a rigid airfoil shape, which makes a look-up table even more applicable.

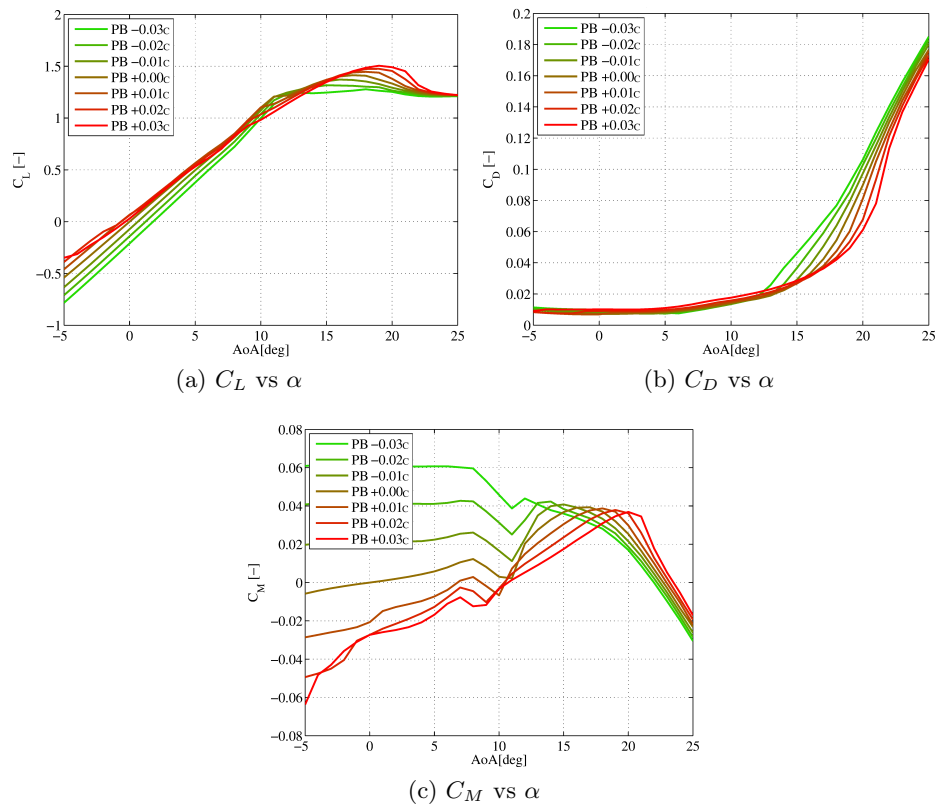


Figure B.5: Influence of upper panel buckling with spar at $0.35c$ on profile coefficient of a NACA 0018

Appendix C

**Sandia 34m Testbed VAWTGen
Input**

Listing C.1: VAWTGen input of Sandia 34m Testbed tower

```

1 -----
2 ----- FAST INDIVIDUAL BLADE FILE -----
3 Properties generated on 18-Feb-11 using NuMAD2PreComp compiled on 2011.01.21
4 ----- BLADE PARAMETERS -----
5 69 NBlInpSt - Number of blade input stations (-)
6 FALSE CalcBMode - Calculate blade mode shapes internally {T: ignore mode shapes from ...
   "below," F: use mode shapes from below} [CURRENTLY IGNORED] (flag)
7 1.5 BldFlDmp(1) - Blade flap mode #1 structural damping in percent of critical (%)
8 1.5 BldFlDmp(2) - Blade flap mode #2 structural damping in percent of critical (%)
9 1.5 BldEdDmp(1) - Blade edge mode #1 structural damping in percent of critical (%)
10 ----- BLADE ADJUSTMENT FACTORS -----
11 1 FlStTunr(1) - Blade flapwise modal stiffness "tuner," 1st mode (-)
12 1 FlStTunr(2) - Blade flapwise modal stiffness "tuner," 2nd mode (-)
13 1 AdjBlMs - Factor to adjust blade mass density (-)
14 1 AdjFlSt - Factor to adjust blade flap stiffness (-)
15 1 AdjEdSt - Factor to adjust blade edge stiffness (-)
16 ----- DISTRIBUTED BLADE PROPERTIES -----
17 BlFract AeroCent StrcTwst BMassDen FlpStiff EdgStiff GJStiff EASTstiff Alpha FlpIner EdgIner PrecrvRef ...
   PreswpRef FlpcgOf EdgcgOf FlpEAOf EdgEAOf
18 (-) (-) (deg) (kg/m) (Nm^2) (Nm^2) (Nm^2) (N) (-) (kg m) (kg m) (m) (m) (m) (m) (m) (m) (m) (m)
19 0.0000 0.2 0 353.43 9.16E+09 9.16E+09 6.80E+09 8.21E+09 0 316.71 316.71 0 0 0 0 0 0
20 0.2000 0.2 0 353.43 9.16E+09 9.16E+09 6.80E+09 8.21E+09 0 316.71 316.71 0 0 0 0 0 0
21 0.4000 0.2 0 353.43 9.16E+09 9.16E+09 6.80E+09 8.21E+09 0 316.71 316.71 0 0 0 0 0 0
22 0.6000 0.2 0 353.43 9.16E+09 9.16E+09 6.80E+09 8.21E+09 0 316.71 316.71 0 0 0 0 0 0
23 0.8000 0.2 0 353.43 9.16E+09 9.16E+09 6.80E+09 8.21E+09 0 316.71 316.71 0 0 0 0 0 0
24 1.0000 0.2 0 353.43 9.16E+09 9.16E+09 6.80E+09 8.21E+09 0 316.71 316.71 0 0 0 0 0 0
25 ----- BLADE MODE SHAPES -----
26 0.191466 BldFl1Sh(2) - Flap mode "1," coeff of x^2
27 -0.244746 BldFl1Sh(3) - "," coeff of x^3
28 2.08616 BldFl1Sh(4) - "," coeff of x^4
29 -1.88019 BldFl1Sh(5) - "," coeff of x^5
30 0.847313 BldFl1Sh(6) - "," coeff of x^6
31 0.207345 BldFl2Sh(2) - Flap mode "2," coeff of x^2
32 -4.65051 BldFl2Sh(3) - "," coeff of x^3
33 11.5381 BldFl2Sh(4) - "," coeff of x^4
34 -15.0152 BldFl2Sh(5) - "," coeff of x^5
35 8.92026 BldFl2Sh(6) - "," coeff of x^6
36 0.563928 BldEdgSh(2) - Edge mode "1," coeff of x^2
37 2.18532 BldEdgSh(3) - "," coeff of x^3
38 -5.1355 BldEdgSh(4) - "," coeff of x^4
39 5.50472 BldEdgSh(5) - "," coeff of x^5
40 -2.11847 BldEdgSh(6) - "," coeff of x^6

```

Listing C.2: VAWTGen input of Sandia 34m Testbed blade

```

1 -----
2 ----- FAST INDIVIDUAL BLADE FILE -----
3 baseline blade model properties from InputData1.5A08V07adm.xls (from C. Hansen) with bugs removed.
4 ----- BLADE PARAMETERS -----
5 64 NBlInpSt - Number of blade input stations (-)
6 FALSE CalcBMode - Calculate blade mode shapes internally {T: ignore mode shapes from ...
   "below," F: use mode shapes from below} [CURRENTLY IGNORED] (flag)
7 3.882 BldFlDmp(1) - Blade flap mode #1 structural damping in percent of critical (%)
8 3.882 BldFlDmp(2) - Blade flap mode #2 structural damping in percent of critical (%)
9 5.9 BldEdDmp(1) - Blade edge mode #1 structural damping in percent of critical (%)
10 ----- BLADE ADJUSTMENT FACTORS -----
11 1 FlStTunr(1) - Blade flapwise modal stiffness "tuner," 1st mode (-)
12 1 FlStTunr(2) - Blade flapwise modal stiffness "tuner," 2nd mode (-)
13 1 AdjBlMs - Factor to adjust blade mass density (-)
14 1 AdjFlSt - Factor to adjust blade flap stiffness (-)
15 1 AdjEdSt - Factor to adjust blade edge stiffness (-)
16 ----- DISTRIBUTED BLADE PROPERTIES -----
17 BlFract AeroCent StrcTwst BMassDen FlpStiff EdgStiff GJStiff EASTstiff Alpha FlpIner EdgIner PrecrvRef ...
   PreswpRef FlpcgOf EdgcgOf FlpEAOf EdgEAOf
18 (-) (-) (deg) (kg/m) (Nm^2) (Nm^2) (Nm^2) (N) (-) (kg m) (kg m) (m) (m) (m) (m) (m) (m)
19 0.0000 0.25 0 103.98 16200000 283000000 16300000 2620000000 0 0.688 11.278 0 0 0 0 0 0
20 0.0133 0.25 0 103.98 16200000 283000000 16300000 2620000000 0 0.688 11.278 0.8528 0 0 0 0 ...
   0 0
21 0.0265 0.25 0 103.98 16200000 283000000 16300000 2620000000 0 0.688 11.278 1.7057 0 0 0 0 ...
   0 0
22 0.0398 0.25 0 103.98 16200000 283000000 16300000 2620000000 0 0.688 11.278 2.5585 0 0 0 0 ...
   0 0
23 0.053 0.25 0 103.98 16200000 283000000 16300000 2620000000 0 0.688 11.278 3.4114 0 0 0 0 ...
   0 0
24 0.0663 0.25 0 103.98 16200000 283000000 16300000 2620000000 0 0.688 11.278 4.2642 0 0 0 0 ...
   0 0
25 0.0795 0.25 0 103.98 16200000 283000000 16300000 2620000000 0 0.688 11.278 5.1171 0 0 0 0 ...
   0 0
26 0.0928 0.25 0 103.98 16200000 283000000 16300000 2620000000 0 0.688 11.278 5.9699 0 0 0 0 ...
   0 0
27 0.106 0.25 0 103.98 16200000 283000000 16300000 2620000000 0 0.688 11.278 6.8228 0 0 0 0 ...
   0 0
28 0.1193 0.25 0 103.98 16200000 283000000 16300000 2620000000 0 0.688 11.278 7.6756 0 0 0 0 ...
   0 0
29 0.1325 0.25 0 103.98 16200000 283000000 16300000 2620000000 0 0.688 11.278 8.5284 0 0 0 0 ...
   0 0
30 0.1441 0.25 0 103.98 16200000 283000000 16300000 2620000000 0 0.688 11.278 9.1161 0 0 0 0 ...

```


	0	0														
53	0.5191	0.25	0	46.194	2970000	70300000	3360000	1160000000	0	0.129	2.705	16.7377	0	0	0	...
	0	0														
54	0.5401	0.25	0	46.194	2970000	70300000	3360000	1160000000	0	0.129	2.705	16.6556	0	0	0	...
	0	0														
55	0.561	0.25	0	46.194	2970000	70300000	3360000	1160000000	0	0.129	2.705	16.5285	0	0	0	...
	0	0														
56	0.5817	0.25	0	46.194	2970000	70300000	3360000	1160000000	0	0.129	2.705	16.3569	0	0	0	...
	0	0														
57	0.6021	0.25	0	46.194	2970000	70300000	3360000	1160000000	0	0.129	2.705	16.1411	0	0	0	...
	0	0														
58	0.6222	0.25	0	46.194	2970000	70300000	3360000	1160000000	0	0.129	2.705	15.8817	0	0	0	...
	0	0														
59	0.642	0.25	0	46.194	2970000	70300000	3360000	1160000000	0	0.129	2.705	15.5795	0	0	0	...
	0	0														
60	0.6614	0.25	0	46.194	2970000	70300000	3360000	1160000000	0	0.129	2.705	15.2351	0	0	0	...
	0	0														
61	0.664	0.25	0	46.194	2970000	70300000	3360000	1160000000	0	0.129	2.705	15.1854	0	0	0	...
	0	0														
62	0.6804	0.25	0	46.194	2970000	70300000	3360000	1160000000	0	0.129	2.705	14.8487	0	0	0	...
	0	0														
63	0.7041	0.25	0	46.194	2970000	70300000	3360000	1160000000	0	0.129	2.705	14.279	0	0	0	...
	0	0														
64	0.7217	0.25	0	58.646	5100000	121000000	5630000	1480000000	0	0.219	4.709	13.7578	0	0	0	...
	0	0														
65	0.732	0.25	0	58.646	5100000	121000000	5630000	1480000000	0	0.219	4.709	13.441	0	0	0	...
	0	0														
66	0.7421	0.25	0	58.646	5100000	121000000	5630000	1480000000	0	0.219	4.709	13.1165	0	0	0	...
	0	0														
67	0.7521	0.25	0	58.646	5100000	121000000	5630000	1480000000	0	0.219	4.709	12.7846	0	0	0	...
	0	0														
68	0.7619	0.25	0	58.646	5100000	121000000	5630000	1480000000	0	0.219	4.709	12.4453	0	0	0	...
	0	0														
69	0.7716	0.25	0	58.646	5100000	121000000	5630000	1480000000	0	0.219	4.709	12.0988	0	0	0	...
	0	0														
70	0.7811	0.25	0	58.646	5100000	121000000	5630000	1480000000	0	0.219	4.709	11.7451	0	0	0	...
	0	0														
71	0.7905	0.25	0	58.646	5100000	121000000	5630000	1480000000	0	0.219	4.709	11.3844	0	0	0	...
	0	0														
72	0.7998	0.25	0	58.646	5100000	121000000	5630000	1480000000	0	0.219	4.709	11.0168	0	0	0	...
	0	0														
73	0.8088	0.25	0	58.646	5100000	121000000	5630000	1480000000	0	0.219	4.709	10.6445	0	0	0	...
	0	0														
74	0.8213	0.25	0	58.646	5100000	121000000	5630000	1480000000	0	0.219	4.709	10.0907	0	0	0	...

0	0																
75	0.8356	0.25	0	103.98	16200000	283000000	16300000	2620000000	0	0.688	11.278	9.2869	0	0	0	...	
0	0																
76	0.8498	0.25	0	103.98	16200000	283000000	16300000	2620000000	0	0.688	11.278	8.483	0	0	0	...	
0	0																
77	0.864	0.25	0	103.98	16200000	283000000	16300000	2620000000	0	0.688	11.278	7.6792	0	0	0	...	
0	0																
78	0.8783	0.25	0	103.98	16200000	283000000	16300000	2620000000	0	0.688	11.278	6.8753	0	0	0	...	
0	0																
79	0.8925	0.25	0	103.98	16200000	283000000	16300000	2620000000	0	0.688	11.278	6.0715	0	0	0	...	
0	0																
80	0.9067	0.25	0	103.98	16200000	283000000	16300000	2620000000	0	0.688	11.278	5.2676	0	0	0	...	
0	0																
81	0.921	0.25	0	103.98	16200000	283000000	16300000	2620000000	0	0.688	11.278	4.4637	0	0	0	...	
0	0																
82	0.9352	0.25	0	103.98	16200000	283000000	16300000	2620000000	0	0.688	11.278	3.6599	0	0	0	...	
0	0																
83	0.9494	0.25	0	103.98	16200000	283000000	16300000	2620000000	0	0.688	11.278	2.856	0	0	0	...	
0	0																
84	0.9637	0.25	0	103.98	16200000	283000000	16300000	2620000000	0	0.688	11.278	2.0522	0	0	0	...	
0	0																
85	0.9779	0.25	0	103.98	16200000	283000000	16300000	2620000000	0	0.688	11.278	1.2483	0	0	0	...	
0	0																
86	0.9921	0.25	0	103.98	16200000	283000000	16300000	2620000000	0	0.688	11.278	0.4445	0	0	0	...	
0	0																
87	1.000	0.25	0	103.98	16200000	283000000	16300000	2620000000	0	0.688	11.278	0	0	0	0	0	0
88	----- BLADE MODE SHAPES -----																
89	0.191466	BldFl1Sh (2)	-	Flap	mode	"1,"	coeff	of	x^2								
90	-0.244746	BldFl1Sh (3)	-	"	coeff	of	x^3										
91	2.08616	BldFl1Sh (4)	-	"	coeff	of	x^4										
92	-1.88019	BldFl1Sh (5)	-	"	coeff	of	x^5										
93	0.847313	BldFl1Sh (6)	-	"	coeff	of	x^6										
94	0.207345	BldFl2Sh (2)	-	Flap	mode	"2,"	coeff	of	x^2								
95	-4.65051	BldFl2Sh (3)	-	"	coeff	of	x^3										
96	11.5381	BldFl2Sh (4)	-	"	coeff	of	x^4										
97	-15.0152	BldFl2Sh (5)	-	"	coeff	of	x^5										
98	8.92026	BldFl2Sh (6)	-	"	coeff	of	x^6										
99	0.563928	BldEdgSh (2)	-	Edge	mode	"1,"	coeff	of	x^2								
100	2.18532	BldEdgSh (3)	-	"	coeff	of	x^3										
101	-5.1355	BldEdgSh (4)	-	"	coeff	of	x^4										
102	5.50472	BldEdgSh (5)	-	"	coeff	of	x^5										
103	-2.11847	BldEdgSh (6)	-	"	coeff	of	x^6										

Appendix D

Structural Input Of Optimized Blade Into HAWC2

In List D.1 the structural properties of the optimized blades can be found. The values have been displayed such that they can be directly used in HAWC2.

Listing D.1: Structure Input File of Optimized Blade

1	#1	Optimized blade through VAWTOPTI												
2	r	m	I_y	x_cg	I_p	y_cg	ri_x	ri_y	x_sh	y_sh	E	G	I_x	...
						k_x	k_y	A	pitch	x_e	y_e			
3	\$1	50	NACA00XX	CFRP										
4	0.00	550.77	0	0	3.233484e-02	8.364319e-02	0.004000	0.000000	2.583543e+10	1.433537e+10	...			
		5.758478e-01	0	0	3.853253e+00	4.429101e+00	0.500000	0.500000	0.859008	0	0.004000	0.000000		
5	4.67	543.66	0	0	3.144214e-02	8.361912e-02	0.004000	0.000000	2.546523e+10	1.402766e+10	...			
		5.374684e-01	0	0	3.801369e+00	4.338837e+00	0.500000	0.500000	0.847107	0	0.004000	0.000000		
6	9.34	536.34	0	0	3.051642e-02	8.359631e-02	0.004000	0.000000	2.508521e+10	1.371653e+10	...			
		4.994693e-01	0	0	3.748140e+00	4.247610e+00	0.500000	0.500000	0.834842	0	0.004000	0.000000		
7	14.02	528.83	0	0	2.955992e-02	8.357518e-02	0.004000	0.000000	2.469676e+10	1.340343e+10	...			
		4.620845e-01	0	0	3.693768e+00	4.155852e+00	0.500000	0.500000	0.822253	0	0.004000	0.000000		
8	18.71	521.17	0	0	2.857775e-02	8.355624e-02	0.004000	0.000000	2.430242e+10	1.309062e+10	...			
		4.256316e-01	0	0	3.638610e+00	4.064242e+00	0.500000	0.500000	0.809415	0	0.004000	0.000000		
9	23.39	513.42	0	0	2.757637e-02	8.354001e-02	0.004000	0.000000	2.390516e+10	1.278060e+10	...			
		3.904299e-01	0	0	3.583091e+00	3.973521e+00	0.500000	0.500000	0.796420	0	0.004000	0.000000		
10	28.07	505.63	0	0	2.656281e-02	8.352700e-02	0.004000	0.000000	2.350811e+10	1.247578e+10	...			
		3.567625e-01	0	0	3.527647e+00	3.884409e+00	0.500000	0.500000	0.783367	0	0.004000	0.000000		
11	32.72	497.86	0	0	2.554322e-02	8.351766e-02	0.004000	0.000000	2.311390e+10	1.217810e+10	...			
		3.248299e-01	0	0	3.472653e+00	3.797483e+00	0.500000	0.500000	0.770340	0	0.004000	0.000000		
12	37.38	490.13	0	0	2.452116e-02	8.351238e-02	0.004000	0.000000	2.272409e+10	1.188852e+10	...			
		2.947092e-01	0	0	3.418326e+00	3.713035e+00	0.500000	0.500000	0.757385	0	0.004000	0.000000		
13	42.04	482.45	0	0	2.349623e-02	8.351153e-02	0.004000	0.000000	2.233867e+10	1.160684e+10	...			
		2.663458e-01	0	0	3.364671e+00	3.631016e+00	0.500000	0.500000	0.744501	0	0.004000	0.000000		
14	46.74	474.80	0	0	2.246753e-02	8.351556e-02	0.004000	0.000000	2.195749e+10	1.133272e+10	...			
		2.396750e-01	0	0	3.311667e+00	3.551342e+00	0.500000	0.500000	0.731679	0	0.004000	0.000000		
15	51.45	467.29	0	0	2.144839e-02	8.352481e-02	0.004000	0.000000	2.158553e+10	1.106948e+10	...			
		2.149699e-01	0	0	3.260013e+00	3.474983e+00	0.500000	0.500000	0.719084	0	0.004000	0.000000		
16	56.15	460.03	0	0	2.045397e-02	8.353935e-02	0.004000	0.000000	2.122817e+10	1.082047e+10	...			
		1.924596e-01	0	0	3.210456e+00	3.402915e+00	0.500000	0.500000	0.706900	0	0.004000	0.000000		
17	60.82	453.08	0	0	1.949522e-02	8.355901e-02	0.004000	0.000000	2.088895e+10	1.058758e+10	...			
		1.722008e-01	0	0	3.163482e+00	3.335682e+00	0.500000	0.500000	0.695250	0	0.004000	0.000000		
18	65.47	446.51	0	0	1.857960e-02	8.358344e-02	0.004000	0.000000	2.056994e+10	1.037164e+10	...			
		1.541345e-01	0	0	3.119375e+00	3.273509e+00	0.500000	0.500000	0.684213	0	0.004000	0.000000		
19	70.10	440.32	0	0	1.771233e-02	8.361216e-02	0.004000	0.000000	2.027232e+10	1.017283e+10	...			
		1.381408e-01	0	0	3.078290e+00	3.216430e+00	0.500000	0.500000	0.673837	0	0.004000	0.000000		
20	74.74	434.55	0	0	1.689771e-02	8.364454e-02	0.004000	0.000000	1.999683e+10	9.991060e+09	...			
		1.240796e-01	0	0	3.040322e+00	3.164402e+00	0.500000	0.500000	0.664158	0	0.004000	0.000000		
21	79.41	429.23	0	0	1.614037e-02	8.367975e-02	0.004000	0.000000	1.974428e+10	9.826307e+09	...			
		1.118185e-01	0	0	3.005574e+00	3.117392e+00	0.500000	0.500000	0.655216	0	0.004000	0.000000		
22	84.11	424.39	0	0	1.544894e-02	8.371658e-02	0.004000	0.000000	1.951671e+10	9.679385e+09	...			
		1.012888e-01	0	0	2.974315e+00	3.075604e+00	0.500000	0.500000	0.647096	0	0.004000	0.000000		

23	88.82	420.11	0	0	1.483455e-02	8.375336e-02	0.004000	0.000000	1.931690e+10	9.551573e+09	...
		9.245109e-02			2.946914e+00	3.039366e+00	0.500000	0.500000	0.639913	0	0.004000
24	93.53	416.44	0	0	1.430634e-02	8.378828e-02	0.004000	0.000000	1.914690e+10	9.443703e+09	...
		8.523425e-02			2.923639e+00	3.008873e+00	0.500000	0.500000	0.633759	0	0.004000
25	98.22	413.43	0	0	1.387118e-02	8.381948e-02	0.004000	0.000000	1.900809e+10	9.356207e+09	...
		7.954849e-02			2.904658e+00	2.984207e+00	0.500000	0.500000	0.628703	0	0.004000
26	102.90	411.10	0	0	1.353396e-02	8.384527e-02	0.004000	0.000000	1.890126e+10	9.289235e+09	...
		7.530105e-02			2.890070e+00	2.965371e+00	0.500000	0.500000	0.624792	0	0.004000
27	107.56	409.48	0	0	1.329801e-02	8.386419e-02	0.004000	0.000000	1.882690e+10	9.242801e+09	...
		7.241047e-02			2.879924e+00	2.952334e+00	0.500000	0.500000	0.622059	0	0.004000
28	112.21	408.56	0	0	1.316578e-02	8.387512e-02	0.004000	0.000000	1.878537e+10	9.216928e+09	...
		7.081949e-02			2.874260e+00	2.945079e+00	0.500000	0.500000	0.620528	0	0.004000
29	116.85	408.38	0	0	1.313962e-02	8.387731e-02	0.004000	0.000000	1.877716e+10	9.211822e+09	...
		7.050720e-02			2.873141e+00	2.943648e+00	0.500000	0.500000	0.620225	0	0.004000
30	121.50	408.96	0	0	1.322264e-02	8.387039e-02	0.004000	0.000000	1.880322e+10	9.228040e+09	...
		7.150105e-02			2.876693e+00	2.948194e+00	0.500000	0.500000	0.621186	0	0.004000
31	126.16	410.31	0	0	1.341889e-02	8.385441e-02	0.004000	0.000000	1.886496e+10	9.266546e+09	...
		7.388302e-02			2.885115e+00	2.958998e+00	0.500000	0.500000	0.623459	0	0.004000
32	130.84	412.47	0	0	1.373255e-02	8.382991e-02	0.004000	0.000000	1.896409e+10	9.328588e+09	...
		7.778572e-02			2.898648e+00	2.976434e+00	0.500000	0.500000	0.627095	0	0.004000
33	135.52	415.48	0	0	1.416677e-02	8.379804e-02	0.004000	0.000000	1.910226e+10	9.415507e+09	...
		8.338530e-02			2.917532e+00	3.000917e+00	0.500000	0.500000	0.632136	0	0.004000
34	140.22	419.33	0	0	1.472255e-02	8.376050e-02	0.004000	0.000000	1.928071e+10	9.528546e+09	...
		9.089161e-02			2.941957e+00	3.032849e+00	0.500000	0.500000	0.638606	0	0.004000
35	144.92	424.03	0	0	1.539776e-02	8.371950e-02	0.004000	0.000000	1.949997e+10	9.668639e+09	...
		1.005341e-01			2.972019e+00	3.072553e+00	0.500000	0.500000	0.646496	0	0.004000
36	149.62	429.55	0	0	1.618645e-02	8.367746e-02	0.004000	0.000000	1.975954e+10	9.836215e+09	...
		1.125425e-01			3.007673e+00	3.120215e+00	0.500000	0.500000	0.655758	0	0.004000
37	154.31	435.83	0	0	1.707866e-02	8.363687e-02	0.004000	0.000000	2.005768e+10	1.003102e+10	...
		1.271239e-01			3.048703e+00	3.175827e+00	0.500000	0.500000	0.666302	0	0.004000
38	158.98	442.80	0	0	1.806080e-02	8.359994e-02	0.004000	0.000000	2.039137e+10	1.025205e+10	...
		1.444384e-01			3.094716e+00	3.239154e+00	0.500000	0.500000	0.677997	0	0.004000
39	163.63	450.37	0	0	1.911854e-02	8.356836e-02	0.004000	0.000000	2.075712e+10	1.049799e+10	...
		1.646192e-01			3.145246e+00	3.309865e+00	0.500000	0.500000	0.690699	0	0.004000
40	168.28	458.46	0	0	2.023788e-02	8.354328e-02	0.004000	0.000000	2.115125e+10	1.076737e+10	...
		1.877715e-01			3.199799e+00	3.387570e+00	0.500000	0.500000	0.704266	0	0.004000
41	172.93	466.96	0	0	2.140309e-02	8.352535e-02	0.004000	0.000000	2.156913e+10	1.105797e+10	...
		2.139106e-01			3.257738e+00	3.471648e+00	0.500000	0.500000	0.718527	0	0.004000
42	177.60	475.76	0	0	2.259674e-02	8.351477e-02	0.004000	0.000000	2.200505e+10	1.136668e+10	...
		2.429281e-01			3.318277e+00	3.561205e+00	0.500000	0.500000	0.733284	0	0.004000
43	182.28	484.72	0	0	2.379988e-02	8.351130e-02	0.004000	0.000000	2.245228e+10	1.168939e+10	...
		2.745601e-01			3.380480e+00	3.655040e+00	0.500000	0.500000	0.748307	0	0.004000
44	186.98	493.68	0	0	2.499210e-02	8.351429e-02	0.004000	0.000000	2.290304e+10	1.202087e+10	...
		3.083567e-01			3.443257e+00	3.751614e+00	0.500000	0.500000	0.763341	0	0.004000

45	191.68	502.49	0	0	2.615160e-02	8.352277e-02	0.004000	0.000000	2.334849e+10	1.235466e+10	...	
		3.436537e-01			3.505372e+00	3.849026e+00	0.500000	0.500000	0.778101	0	0.004000	0.000000
46	196.36	510.94	0	0	2.725532e-02	8.353551e-02	0.004000	0.000000	2.377884e+10	1.268308e+10	...	
		3.795545e-01			3.565446e+00	3.945001e+00	0.500000	0.500000	0.792275	0	0.004000	0.000000
47	201.03	518.91	0	0	2.828638e-02	8.355118e-02	0.004000	0.000000	2.418632e+10	1.299949e+10	...	
		4.151867e-01			3.622380e+00	4.037567e+00	0.500000	0.500000	0.805624	0	0.004000	0.000000
48	205.69	526.31	0	0	2.923814e-02	8.356866e-02	0.004000	0.000000	2.456706e+10	1.329999e+10	...	
		4.499285e-01			3.675621e+00	4.125550e+00	0.500000	0.500000	0.818037	0	0.004000	0.000000
49	210.36	533.10	0	0	3.010486e-02	8.358691e-02	0.004000	0.000000	2.491754e+10	1.358078e+10	...	
		4.831523e-01			3.724666e+00	4.207819e+00	0.500000	0.500000	0.829415	0	0.004000	0.000000
50	215.04	539.22	0	0	3.088138e-02	8.360504e-02	0.004000	0.000000	2.523456e+10	1.383823e+10	...	
		5.142342e-01			3.769055e+00	4.283289e+00	0.500000	0.500000	0.839668	0	0.004000	0.000000
51	219.73	544.64	0	0	3.156482e-02	8.362231e-02	0.004000	0.000000	2.551589e+10	1.406949e+10	...	
		5.426409e-01			3.808467e+00	4.351108e+00	0.500000	0.500000	0.848738	0	0.004000	0.000000
52	224.40	549.34	0	0	3.215648e-02	8.363822e-02	0.004000	0.000000	2.576118e+10	1.427328e+10	...	
		5.680418e-01			3.842844e+00	4.410886e+00	0.500000	0.500000	0.856624	0	0.004000	0.000000
53	225.96	550.77	0	0	3.233484e-02	8.364319e-02	0.004000	0.000000	2.583543e+10	1.433537e+10	...	
		5.758478e-01			3.853253e+00	4.429101e+00	0.500000	0.500000	0.859008	0	0.004000	0.000000
54	\$2 50	NACA changing	ZZ - CFRP									
55	0.00	550.77	0	0	3.233484e-02	8.364319e-02	0.004000	0.000000	2.583543e+10	1.433537e+10	...	
		5.758478e-01			3.853253e+00	4.429101e+00	0.500000	0.500000	0.859008	0	0.004000	0.000000
56	4.63	544.45	0	0	3.154202e-02	8.362172e-02	0.004000	0.000000	2.550647e+10	1.406171e+10	...	
		5.416771e-01			3.807147e+00	4.348824e+00	0.500000	0.500000	0.848435	0	0.004000	0.000000
57	9.28	537.81	0	0	3.070257e-02	8.360072e-02	0.004000	0.000000	2.516131e+10	1.377845e+10	...	
		5.069654e-01			3.758796e+00	4.265762e+00	0.500000	0.500000	0.837302	0	0.004000	0.000000
58	13.95	530.83	0	0	2.981479e-02	8.358056e-02	0.004000	0.000000	2.479985e+10	1.348604e+10	...	
		4.718625e-01			3.708194e+00	4.180056e+00	0.500000	0.500000	0.825599	0	0.004000	0.000000
59	18.62	523.55	0	0	2.888349e-02	8.356182e-02	0.004000	0.000000	2.442467e+10	1.318706e+10	...	
		4.367720e-01			3.655706e+00	4.092478e+00	0.500000	0.500000	0.813401	0	0.004000	0.000000
60	23.28	516.02	0	0	2.791427e-02	8.354512e-02	0.004000	0.000000	2.403866e+10	1.288422e+10	...	
		4.020898e-01			3.601743e+00	4.003833e+00	0.500000	0.500000	0.800794	0	0.004000	0.000000
61	27.91	508.30	0	0	2.691179e-02	8.353108e-02	0.004000	0.000000	2.364424e+10	1.257973e+10	...	
		3.681353e-01			3.546651e+00	3.914786e+00	0.500000	0.500000	0.787850	0	0.004000	0.000000
62	32.53	500.41	0	0	2.587848e-02	8.352030e-02	0.004000	0.000000	2.324294e+10	1.227500e+10	...	
		3.351192e-01			3.490648e+00	3.825768e+00	0.500000	0.500000	0.774612	0	0.004000	0.000000
63	37.16	492.34	0	0	2.481455e-02	8.351346e-02	0.004000	0.000000	2.283544e+10	1.197075e+10	...	
		3.031653e-01			3.433838e+00	3.737003e+00	0.500000	0.500000	0.761093	0	0.004000	0.000000
64	41.82	484.14	0	0	2.372337e-02	8.351132e-02	0.004000	0.000000	2.242361e+10	1.166852e+10	...	
		2.724755e-01			3.376489e+00	3.648955e+00	0.500000	0.500000	0.747347	0	0.004000	0.000000
65	46.50	475.95	0	0	2.262321e-02	8.351462e-02	0.004000	0.000000	2.201481e+10	1.137366e+10	...	
		2.435979e-01			3.319633e+00	3.563231e+00	0.500000	0.500000	0.733612	0	0.004000	0.000000
66	51.18	467.92	0	0	2.153353e-02	8.352383e-02	0.004000	0.000000	2.161638e+10	1.109116e+10	...	
		2.169697e-01			3.264295e+00	3.481265e+00	0.500000	0.500000	0.720132	0	0.004000	0.000000
67	55.84	460.15	0	0	2.047069e-02	8.353905e-02	0.004000	0.000000	2.123413e+10	1.082459e+10	...	

		1.928255e-01		3.211282e+00	3.404108e+00	0.500000	0.500000	0.707104	0	0.004000	0.000000	
68	60.48	452.74	0	0	1.944816e-02	8.356012e-02	0.004000	0.000000	2.087243e+10	1.057633e+10	...	
		1.712420e-01		3.161196e+00	3.332438e+00	0.500000	0.500000	0.694681	0	0.004000	0.000000	
69	65.11	445.77	0	0	1.847674e-02	8.358656e-02	0.004000	0.000000	2.053441e+10	1.034778e+10	...	
		1.521814e-01		3.114466e+00	3.266648e+00	0.500000	0.500000	0.682978	0	0.004000	0.000000	
70	69.73	439.28	0	0	1.756506e-02	8.361762e-02	0.004000	0.000000	2.022222e+10	1.013961e+10	...	
		1.355305e-01		3.071380e+00	3.206911e+00	0.500000	0.500000	0.672082	0	0.004000	0.000000	
71	74.36	433.30	0	0	1.672004e-02	8.365234e-02	0.004000	0.000000	1.993727e+10	9.952045e+09	...	
		1.211337e-01		3.032122e+00	3.153256e+00	0.500000	0.500000	0.662055	0	0.004000	0.000000	
72	79.01	427.88	0	0	1.594820e-02	8.368953e-02	0.004000	0.000000	1.968074e+10	9.785140e+09	...	
		1.088290e-01		2.996841e+00	3.105670e+00	0.500000	0.500000	0.652955	0	0.004000	0.000000	
73	83.67	423.06	0	0	1.525779e-02	8.372760e-02	0.004000	0.000000	1.945430e+10	9.639345e+09	...	
		9.848739e-02		2.965752e+00	3.064240e+00	0.500000	0.500000	0.644858	0	0.004000	0.000000	
74	88.33	418.87	0	0	1.465643e-02	8.376479e-02	0.004000	0.000000	1.925939e+10	9.514992e+09	...	
		8.997846e-02		2.939036e+00	3.029015e+00	0.500000	0.500000	0.637836	0	0.004000	0.000000	
75	93.00	415.36	0	0	1.415023e-02	8.379921e-02	0.004000	0.000000	1.909697e+10	9.412173e+09	...	
		8.316774e-02		2.916809e+00	2.999977e+00	0.500000	0.500000	0.631944	0	0.004000	0.000000	
76	97.66	412.55	0	0	1.374359e-02	8.382907e-02	0.004000	0.000000	1.896759e+10	9.330783e+09	...	
		7.792529e-02		2.899126e+00	2.977052e+00	0.500000	0.500000	0.627223	0	0.004000	0.000000	
77	102.31	410.45	0	0	1.343941e-02	8.385276e-02	0.004000	0.000000	1.887143e+10	9.270587e+09	...	
		7.413475e-02		2.885998e+00	2.960133e+00	0.500000	0.500000	0.623697	0	0.004000	0.000000	
78	106.95	409.07	0	0	1.323935e-02	8.386901e-02	0.004000	0.000000	1.880847e+10	9.231310e+09	...	
		7.170211e-02		2.877409e+00	2.949111e+00	0.500000	0.500000	0.621379	0	0.004000	0.000000	
79	111.58	408.42	0	0	1.314440e-02	8.387691e-02	0.004000	0.000000	1.877866e+10	9.212755e+09	...	
		7.056425e-02		2.873346e+00	2.943910e+00	0.500000	0.500000	0.620280	0	0.004000	0.000000	
80	116.21	408.49	0	0	1.315557e-02	8.387597e-02	0.004000	0.000000	1.878216e+10	9.214934e+09	...	
		7.069749e-02		2.873823e+00	2.944521e+00	0.500000	0.500000	0.620409	0	0.004000	0.000000	
81	120.85	409.31	0	0	1.327445e-02	8.386612e-02	0.004000	0.000000	1.881950e+10	9.238182e+09	...	
		7.212540e-02		2.878913e+00	2.951039e+00	0.500000	0.500000	0.621786	0	0.004000	0.000000	
82	125.49	410.89	0	0	1.350311e-02	8.384770e-02	0.004000	0.000000	1.889152e+10	9.283144e+09	...	
		7.491930e-02		2.888740e+00	2.963659e+00	0.500000	0.500000	0.624435	0	0.004000	0.000000	
83	130.15	413.24	0	0	1.384333e-02	8.382156e-02	0.004000	0.000000	1.899924e+10	9.350648e+09	...	
		7.919249e-02		2.903449e+00	2.982642e+00	0.500000	0.500000	0.628380	0	0.004000	0.000000	
84	134.81	416.37	0	0	1.429577e-02	8.378901e-02	0.004000	0.000000	1.914352e+10	9.441563e+09	...	
		8.509337e-02		2.923175e+00	3.008269e+00	0.500000	0.500000	0.633636	0	0.004000	0.000000	
85	139.47	420.28	0	0	1.485925e-02	8.375181e-02	0.004000	0.000000	1.932489e+10	9.556663e+09	...	
		9.279713e-02		2.948009e+00	3.040806e+00	0.500000	0.500000	0.640201	0	0.004000	0.000000	
86	144.14	424.96	0	0	1.553028e-02	8.371200e-02	0.004000	0.000000	1.954333e+10	9.696497e+09	...	
		1.024951e-01		2.977969e+00	3.080464e+00	0.500000	0.500000	0.648049	0	0.004000	0.000000	
87	148.80	430.37	0	0	1.630271e-02	8.367177e-02	0.004000	0.000000	1.979812e+10	9.861282e+09	...	
		1.143820e-01		3.012977e+00	3.127359e+00	0.500000	0.500000	0.657128	0	0.004000	0.000000	
88	153.44	436.46	0	0	1.716788e-02	8.363319e-02	0.004000	0.000000	2.008776e+10	1.005082e+10	...	
		1.286414e-01		3.052846e+00	3.181488e+00	0.500000	0.500000	0.667361	0	0.004000	0.000000	
89	158.07	443.19	0	0	1.811532e-02	8.359811e-02	0.004000	0.000000	2.041006e+10	1.026453e+10	...	

		1.454393e-01		3.097296e+00	3.242735e+00	0.500000	0.500000	0.678649	0	0.004000	0.000000	
90	162.70	450.49	0	0	1.913499e-02	8.356793e-02	0.004000	0.000000	2.076286e+10	1.050188e+10	...	
		1.649459e-01		3.146040e+00	3.310986e+00	0.500000	0.500000	0.690898	0	0.004000	0.000000	
91	167.33	458.30	0	0	2.021558e-02	8.354370e-02	0.004000	0.000000	2.114333e+10	1.076191e+10	...	
		1.872918e-01		3.198701e+00	3.385993e+00	0.500000	0.500000	0.703994	0	0.004000	0.000000	
92	171.97	466.52	0	0	2.134349e-02	8.352608e-02	0.004000	0.000000	2.154757e+10	1.104285e+10	...	
		2.125221e-01		3.254746e+00	3.467269e+00	0.500000	0.500000	0.717794	0	0.004000	0.000000	
93	176.63	475.06	0	0	2.250280e-02	8.351534e-02	0.004000	0.000000	2.197046e+10	1.134198e+10	...	
		2.405601e-01		3.313470e+00	3.554030e+00	0.500000	0.500000	0.732117	0	0.004000	0.000000	
94	181.30	483.78	0	0	2.367521e-02	8.351134e-02	0.004000	0.000000	2.240558e+10	1.165541e+10	...	
		2.711686e-01		3.373980e+00	3.645149e+00	0.500000	0.500000	0.746743	0	0.004000	0.000000	
95	185.98	492.54	0	0	2.484019e-02	8.351357e-02	0.004000	0.000000	2.284519e+10	1.197797e+10	...	
		3.039117e-01		3.435197e+00	3.739108e+00	0.500000	0.500000	0.761417	0	0.004000	0.000000	
96	190.65	501.14	0	0	2.597498e-02	8.352114e-02	0.004000	0.000000	2.328019e+10	1.230308e+10	...	
		3.381192e-01		3.495845e+00	3.833964e+00	0.500000	0.500000	0.775844	0	0.004000	0.000000	
97	195.28	509.41	0	0	2.705617e-02	8.353289e-02	0.004000	0.000000	2.370074e+10	1.262304e+10	...	
		3.729074e-01		3.554539e+00	3.927447e+00	0.500000	0.500000	0.789709	0	0.004000	0.000000	
98	199.90	517.26	0	0	2.807354e-02	8.354766e-02	0.004000	0.000000	2.410178e+10	1.293341e+10	...	
		4.076627e-01		3.610564e+00	4.018227e+00	0.500000	0.500000	0.802860	0	0.004000	0.000000	
99	204.53	524.65	0	0	2.902533e-02	8.356451e-02	0.004000	0.000000	2.448155e+10	1.323209e+10	...	
		4.420037e-01		3.663661e+00	4.105664e+00	0.500000	0.500000	0.815254	0	0.004000	0.000000	
100	209.19	531.57	0	0	2.990933e-02	8.358260e-02	0.004000	0.000000	2.483816e+10	1.351683e+10	...	
		4.755230e-01		3.713556e+00	4.189079e+00	0.500000	0.500000	0.826842	0	0.004000	0.000000	
101	213.86	537.97	0	0	3.072244e-02	8.360119e-02	0.004000	0.000000	2.516944e+10	1.378508e+10	...	
		5.077699e-01		3.759935e+00	4.267705e+00	0.500000	0.500000	0.837565	0	0.004000	0.000000	
102	218.53	543.82	0	0	3.146168e-02	8.361963e-02	0.004000	0.000000	2.547329e+10	1.403431e+10	...	
		5.382902e-01		3.802499e+00	4.340789e+00	0.500000	0.500000	0.847367	0	0.004000	0.000000	
103	223.16	549.10	0	0	3.212600e-02	8.363738e-02	0.004000	0.000000	2.574850e+10	1.426270e+10	...	
		5.667146e-01		3.841067e+00	4.407782e+00	0.500000	0.500000	0.856217	0	0.004000	0.000000	
104	224.71	550.77	0	0	3.233484e-02	8.364319e-02	0.004000	0.000000	2.583543e+10	1.433537e+10	...	
		5.758478e-01		3.853253e+00	4.429101e+00	0.500000	0.500000	0.859008	0	0.004000	0.000000	
105	\$3 50	NACA 0030	-	GFRP								
106	0.00	808.70	0	0	6.226500e-02	8.522543e-02	0.004000	0.000000	4.015372e+10	3.000015e+10	...	
		3.135280e+00		5.873903e+00	9.009182e+00	0.500000	0.500000	1.290483	0	0.004000	0.000000	
107	4.72	792.46	0	0	6.048176e-02	8.511826e-02	0.004000	0.000000	3.921755e+10	2.872984e+10	...	
		2.898870e+00		5.741500e+00	8.640370e+00	0.500000	0.500000	1.263355	0	0.004000	0.000000	
108	9.44	775.85	0	0	5.864678e-02	8.500993e-02	0.004000	0.000000	3.826517e+10	2.747400e+10	...	
		2.668495e+00		5.606829e+00	8.275325e+00	0.500000	0.500000	1.235593	0	0.004000	0.000000	
109	14.23	758.66	0	0	5.673642e-02	8.489935e-02	0.004000	0.000000	3.728558e+10	2.622039e+10	...	
		2.442142e+00		5.468344e+00	7.910485e+00	0.500000	0.500000	1.206862	0	0.004000	0.000000	
110	19.06	741.10	0	0	5.477185e-02	8.478814e-02	0.004000	0.000000	3.629104e+10	2.498685e+10	...	
		2.223264e+00		5.327781e+00	7.551044e+00	0.500000	0.500000	1.177509	0	0.004000	0.000000	
111	23.89	723.42	0	0	5.278000e-02	8.467814e-02	0.004000	0.000000	3.529615e+10	2.379206e+10	...	
		2.015257e+00		5.187214e+00	7.202471e+00	0.500000	0.500000	1.147956	0	0.004000	0.000000	

112	28.68	705.87	0	0	5.078717e-02	8.457110e-02	0.004000	0.000000	3.431454e+10	2.265125e+10	...	
		1.820677e+00			5.048574e+00	6.869251e+00	0.500000	0.500000	1.118608	0	0.004000	0.000000
113	33.40	688.58	0	0	4.880850e-02	8.446803e-02	0.004000	0.000000	3.335376e+10	2.157085e+10	...	
		1.640390e+00			4.912933e+00	6.553323e+00	0.500000	0.500000	1.089697	0	0.004000	0.000000
114	38.08	671.52	0	0	4.683899e-02	8.436891e-02	0.004000	0.000000	3.241136e+10	2.054551e+10	...	
		1.473240e+00			4.779950e+00	6.253190e+00	0.500000	0.500000	1.061155	0	0.004000	0.000000
115	42.78	654.47	0	0	4.485304e-02	8.427279e-02	0.004000	0.000000	3.147544e+10	1.956054e+10	...	
		1.316651e+00			4.647953e+00	5.964604e+00	0.500000	0.500000	1.032625	0	0.004000	0.000000
116	47.55	637.24	0	0	4.282835e-02	8.417915e-02	0.004000	0.000000	3.053641e+10	1.860521e+10	...	
		1.168877e+00			4.515596e+00	5.684473e+00	0.500000	0.500000	1.003808	0	0.004000	0.000000
117	52.38	620.19	0	0	4.080232e-02	8.409033e-02	0.004000	0.000000	2.961238e+10	1.769689e+10	...	
		1.032502e+00			4.385443e+00	5.417946e+00	0.500000	0.500000	0.975257	0	0.004000	0.000000
118	57.20	603.67	0	0	3.881960e-02	8.400866e-02	0.004000	0.000000	2.872360e+10	1.685250e+10	...	
		9.097023e-01			4.260350e+00	5.170052e+00	0.500000	0.500000	0.947605	0	0.004000	0.000000
119	62.00	587.95	0	0	3.691274e-02	8.393559e-02	0.004000	0.000000	2.788362e+10	1.608045e+10	...	
		8.011129e-01			4.142222e+00	4.943335e+00	0.500000	0.500000	0.921292	0	0.004000	0.000000
120	66.78	573.21	0	0	3.510415e-02	8.387182e-02	0.004000	0.000000	2.710067e+10	1.538321e+10	...	
		7.063632e-01			4.032211e+00	4.738574e+00	0.500000	0.500000	0.896601	0	0.004000	0.000000
121	71.52	559.53	0	0	3.340866e-02	8.381750e-02	0.004000	0.000000	2.637913e+10	1.475948e+10	...	
		6.245150e-01			3.930919e+00	4.555434e+00	0.500000	0.500000	0.873697	0	0.004000	0.000000
122	76.25	546.98	0	0	3.183588e-02	8.377237e-02	0.004000	0.000000	2.572083e+10	1.420593e+10	...	
		5.543756e-01			3.838592e+00	4.392967e+00	0.500000	0.500000	0.852668	0	0.004000	0.000000
123	80.98	535.57	0	0	3.039239e-02	8.373587e-02	0.004000	0.000000	2.512620e+10	1.371846e+10	...	
		4.947070e-01			3.755273e+00	4.249980e+00	0.500000	0.500000	0.833557	0	0.004000	0.000000
124	85.72	525.35	0	0	2.908598e-02	8.370733e-02	0.004000	0.000000	2.459612e+10	1.329379e+10	...	
		4.444410e-01			3.681066e+00	4.125507e+00	0.500000	0.500000	0.816422	0	0.004000	0.000000
125	90.48	516.36	0	0	2.792800e-02	8.368593e-02	0.004000	0.000000	2.413279e+10	1.293014e+10	...	
		4.027496e-01			3.616265e+00	4.019014e+00	0.500000	0.500000	0.801365	0	0.004000	0.000000
126	95.24	508.69	0	0	2.693057e-02	8.367069e-02	0.004000	0.000000	2.373872e+10	1.262631e+10	...	
		3.689268e-01			3.561196e+00	3.930123e+00	0.500000	0.500000	0.788495	0	0.004000	0.000000
127	100.02	502.38	0	0	2.610559e-02	8.366050e-02	0.004000	0.000000	2.341636e+10	1.238146e+10	...	
		3.423715e-01			3.516183e+00	3.858554e+00	0.500000	0.500000	0.777922	0	0.004000	0.000000
128	104.79	497.50	0	0	2.546413e-02	8.365418e-02	0.004000	0.000000	2.316797e+10	1.219505e+10	...	
		3.225903e-01			3.481521e+00	3.804111e+00	0.500000	0.500000	0.769745	0	0.004000	0.000000
129	109.57	494.11	0	0	2.501586e-02	8.365064e-02	0.004000	0.000000	2.299559e+10	1.206682e+10	...	
		3.092088e-01			3.457477e+00	3.766686e+00	0.500000	0.500000	0.764055	0	0.004000	0.000000
130	114.34	492.24	0	0	2.476896e-02	8.364901e-02	0.004000	0.000000	2.290106e+10	1.199690e+10	...	
		3.019915e-01			3.444297e+00	3.746289e+00	0.500000	0.500000	0.760929	0	0.004000	0.000000
131	119.11	491.95	0	0	2.473015e-02	8.364877e-02	0.004000	0.000000	2.288623e+10	1.198595e+10	...	
		3.008668e-01			3.442230e+00	3.743097e+00	0.500000	0.500000	0.760438	0	0.004000	0.000000
132	123.88	493.27	0	0	2.490507e-02	8.364988e-02	0.004000	0.000000	2.295313e+10	1.203538e+10	...	
		3.059566e-01			3.451557e+00	3.757514e+00	0.500000	0.500000	0.762652	0	0.004000	0.000000
133	128.65	496.24	0	0	2.529818e-02	8.365278e-02	0.004000	0.000000	2.310404e+10	1.214738e+10	...	
		3.175943e-01			3.472603e+00	3.790197e+00	0.500000	0.500000	0.767636	0	0.004000	0.000000

134	133.42	500.90	0	0	2.591199e-02	8.365844e-02	0.004000	0.000000	2.334119e+10	1.232484e+10	...	
		3.363223e-01			3.505690e+00	3.842012e+00	0.500000	0.500000	0.775450	0	0.004000	0.000000
135	138.18	507.27	0	0	2.674631e-02	8.366822e-02	0.004000	0.000000	2.366644e+10	1.257112e+10	...	
		3.628856e-01			3.551100e+00	3.913986e+00	0.500000	0.500000	0.786128	0	0.004000	0.000000
136	142.94	515.36	0	0	2.779765e-02	8.368376e-02	0.004000	0.000000	2.408103e+10	1.288994e+10	...	
		3.982210e-01			3.609028e+00	4.007249e+00	0.500000	0.500000	0.799678	0	0.004000	0.000000
137	147.70	525.14	0	0	2.905905e-02	8.370679e-02	0.004000	0.000000	2.458527e+10	1.328519e+10	...	
		4.434411e-01			3.679549e+00	4.122990e+00	0.500000	0.500000	0.816071	0	0.004000	0.000000
138	152.45	536.58	0	0	3.052015e-02	8.373890e-02	0.004000	0.000000	2.517846e+10	1.376083e+10	...	
		4.998110e-01			3.762592e+00	4.262403e+00	0.500000	0.500000	0.835241	0	0.004000	0.000000
139	157.20	549.62	0	0	3.216768e-02	8.378144e-02	0.004000	0.000000	2.585881e+10	1.432074e+10	...	
		5.687203e-01			3.857936e+00	4.426657e+00	0.500000	0.500000	0.857086	0	0.004000	0.000000
140	161.94	564.17	0	0	3.398634e-02	8.383538e-02	0.004000	0.000000	2.662359e+10	1.496880e+10	...	
		6.516618e-01			3.965228e+00	4.616889e+00	0.500000	0.500000	0.881473	0	0.004000	0.000000
141	166.69	580.17	0	0	3.596015e-02	8.390130e-02	0.004000	0.000000	2.746955e+10	1.570904e+10	...	
		7.502303e-01			4.084029e+00	4.834260e+00	0.500000	0.500000	0.908255	0	0.004000	0.000000
142	171.45	597.46	0	0	3.806917e-02	8.397923e-02	0.004000	0.000000	2.839128e+10	1.654406e+10	...	
		8.658777e-01			4.213603e+00	5.079481e+00	0.500000	0.500000	0.937216	0	0.004000	0.000000
143	176.23	615.88	0	0	4.028733e-02	8.406859e-02	0.004000	0.000000	2.938004e+10	1.747340e+10	...	
		9.996118e-01			4.352733e+00	5.352345e+00	0.500000	0.500000	0.968047	0	0.004000	0.000000
144	181.02	635.16	0	0	4.258219e-02	8.416809e-02	0.004000	0.000000	3.042330e+10	1.849234e+10	...	
		1.151704e+00			4.499659e+00	5.651363e+00	0.500000	0.500000	1.000324	0	0.004000	0.000000
145	185.82	655.00	0	0	4.491525e-02	8.427574e-02	0.004000	0.000000	3.150454e+10	1.959067e+10	...	
		1.321379e+00			4.652056e+00	5.973436e+00	0.500000	0.500000	1.033515	0	0.004000	0.000000
146	190.62	675.01	0	0	4.724274e-02	8.438893e-02	0.004000	0.000000	3.260341e+10	2.075172e+10	...	
		1.506529e+00			4.807045e+00	6.313574e+00	0.500000	0.500000	1.066987	0	0.004000	0.000000
147	195.40	694.75	0	0	4.951660e-02	8.450453e-02	0.004000	0.000000	3.369599e+10	2.195161e+10	...	
		1.703461e+00			4.961242e+00	6.664703e+00	0.500000	0.500000	1.100017	0	0.004000	0.000000
148	200.13	713.78	0	0	5.168706e-02	8.461905e-02	0.004000	0.000000	3.475608e+10	2.315976e+10	...	
		1.906897e+00			5.110930e+00	7.017827e+00	0.500000	0.500000	1.131833	0	0.004000	0.000000
149	204.84	731.84	0	0	5.373011e-02	8.473025e-02	0.004000	0.000000	3.576901e+10	2.435507e+10	...	
		2.112759e+00			5.254017e+00	7.366777e+00	0.500000	0.500000	1.162026	0	0.004000	0.000000
150	209.56	748.88	0	0	5.564455e-02	8.483722e-02	0.004000	0.000000	3.673121e+10	2.552795e+10	...	
		2.318783e+00			5.389987e+00	7.708770e+00	0.500000	0.500000	1.190524	0	0.004000	0.000000
151	214.34	764.87	0	0	5.742779e-02	8.493910e-02	0.004000	0.000000	3.763869e+10	2.666784e+10	...	
		2.522499e+00			5.518259e+00	8.040758e+00	0.500000	0.500000	1.217239	0	0.004000	0.000000
152	219.17	779.68	0	0	5.907017e-02	8.503475e-02	0.004000	0.000000	3.848392e+10	2.775921e+10	...	
		2.720509e+00			5.637760e+00	8.358269e+00	0.500000	0.500000	1.241984	0	0.004000	0.000000
153	223.99	793.11	0	0	6.055274e-02	8.512250e-02	0.004000	0.000000	3.925461e+10	2.877945e+10	...	
		2.908042e+00			5.746742e+00	8.654783e+00	0.500000	0.500000	1.264432	0	0.004000	0.000000
154	228.69	804.95	0	0	6.185354e-02	8.520055e-02	0.004000	0.000000	3.993679e+10	2.970261e+10	...	
		3.079616e+00			5.843220e+00	8.922836e+00	0.500000	0.500000	1.284211	0	0.004000	0.000000
155	230.28	808.70	0	0	6.226500e-02	8.522543e-02	0.004000	0.000000	4.015372e+10	3.000015e+10	...	
		3.135280e+00			5.873903e+00	9.009182e+00	0.500000	0.500000	1.290483	0	0.004000	0.000000

Appendix E

Polar Data Of Used Airfoils

In Figure E.2 the polar data of all used airfoils can be found. The data have been extracted from XFOil at a Reynolds number of 10^6 . The angle of attack is only taken from a range between -21° and 21° , due to the fact that XFOil has its imitation determine post stall. Values beyond this point have been taken from the Lectures of *Introduction to Wind Turbine Technology* [21] and can be examined in Figure E.1.

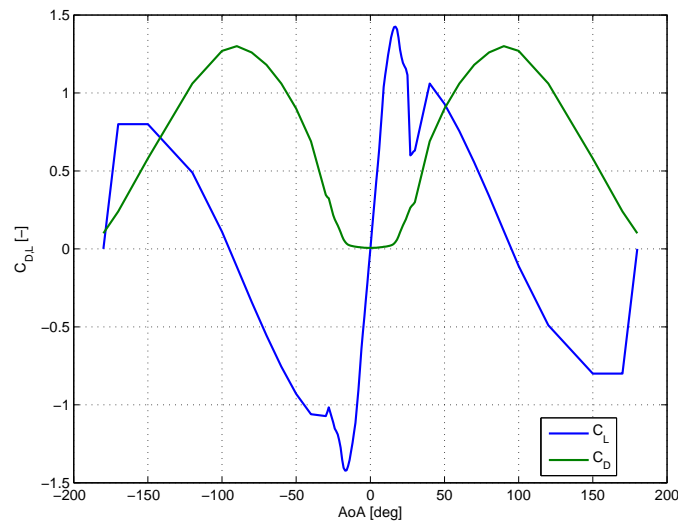


Figure E.1: Extrapolated profile coefficient of NACA0015 at $Re = 10^6$ [21]

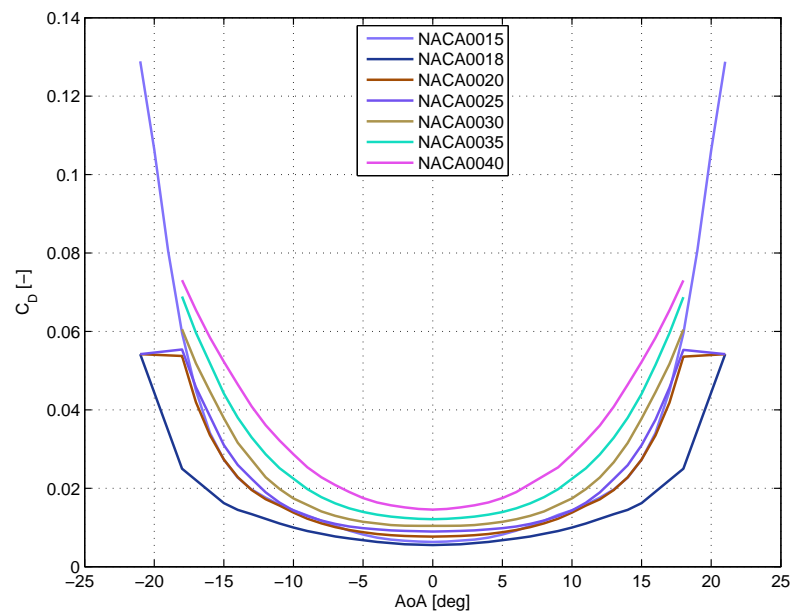
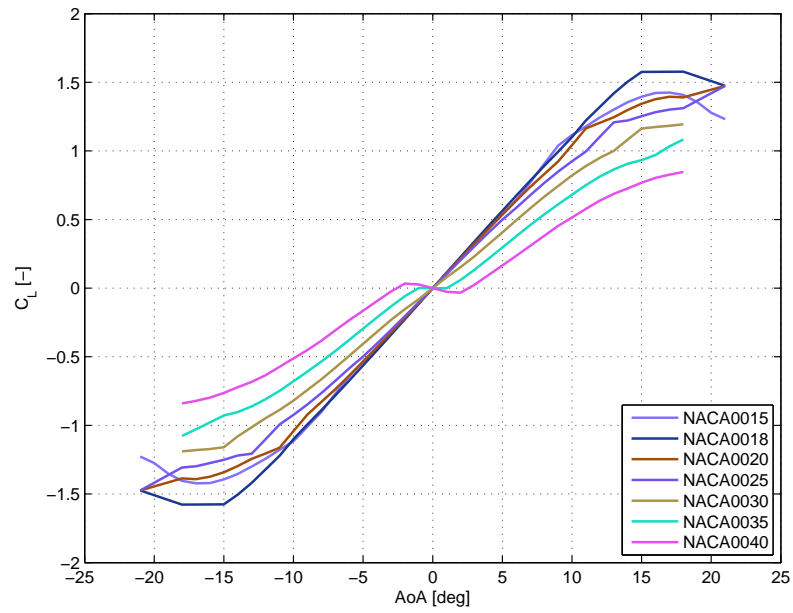


Figure E.2: Profile coefficient of used airfoils at $Re = 10^6$

Appendix F

Loads On Optimized Blades

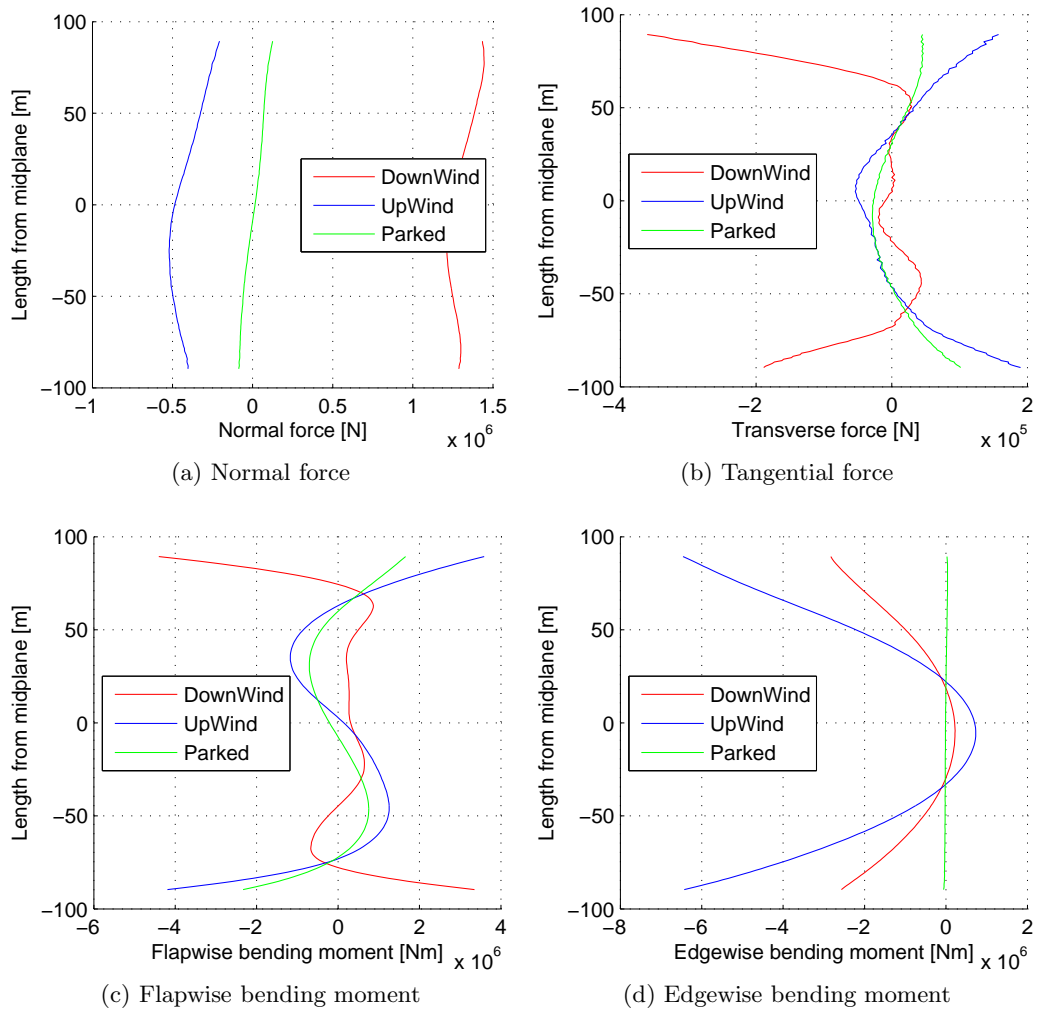


Figure F.1: Force and moments on the NACA 0015-35 CFRP blade

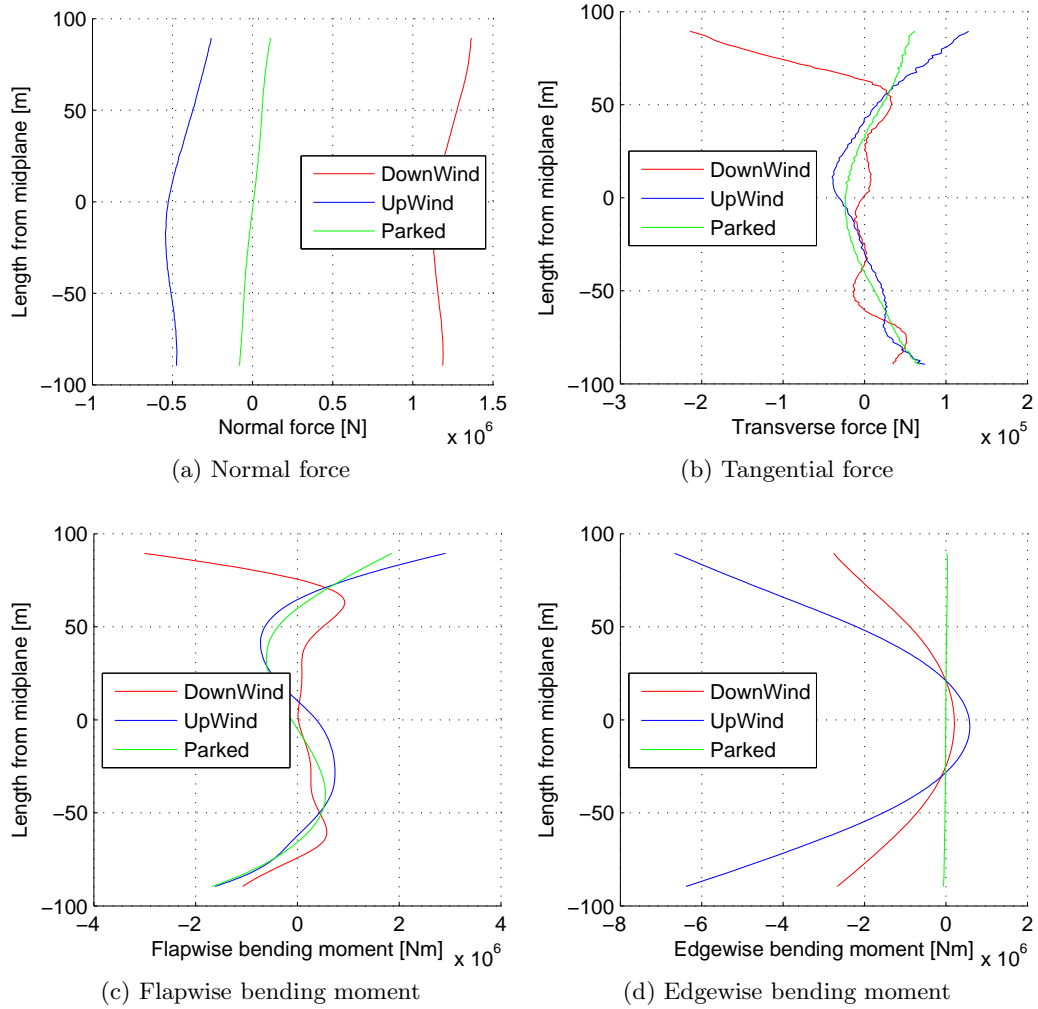


Figure F.2: Force and moments on the NACA 0015-40 CFRP blade

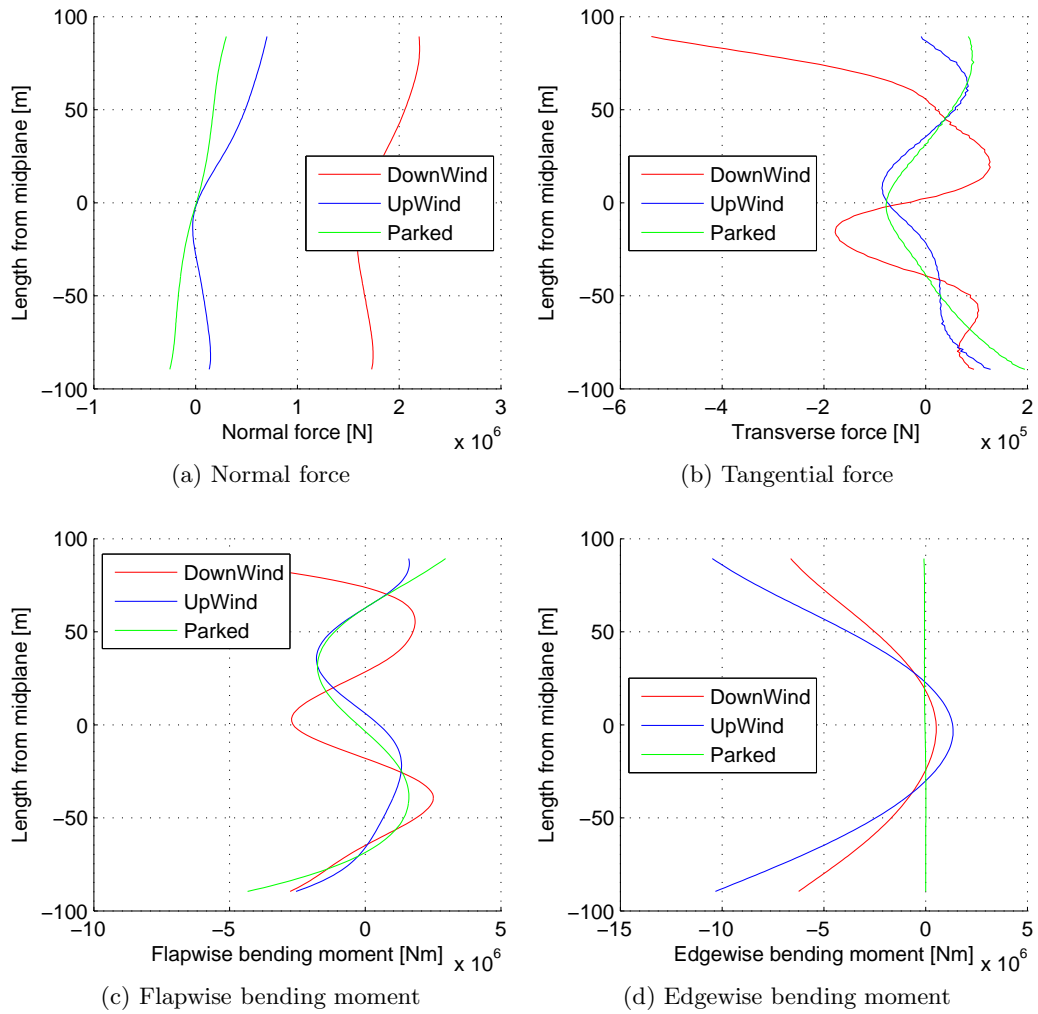
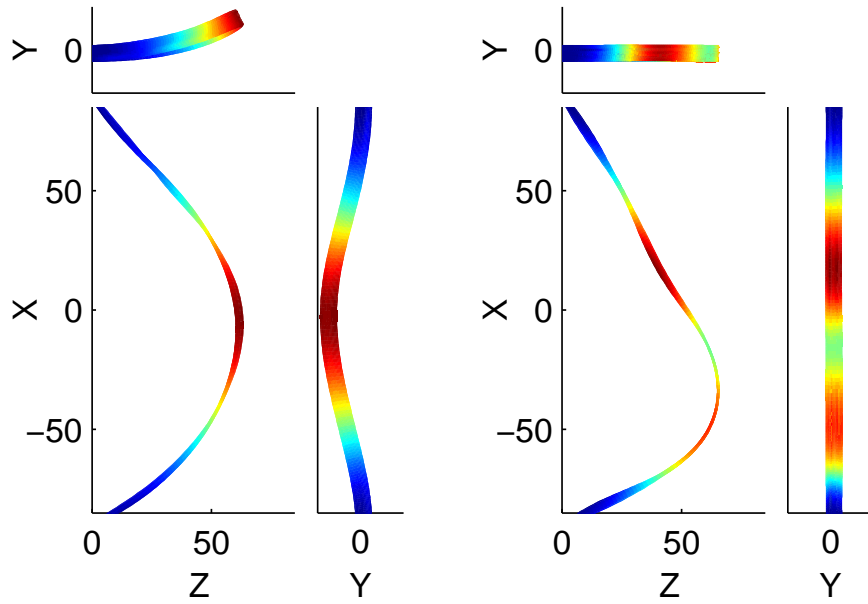


Figure F.3: Force and moments on the NACA 0030 GFRP blade

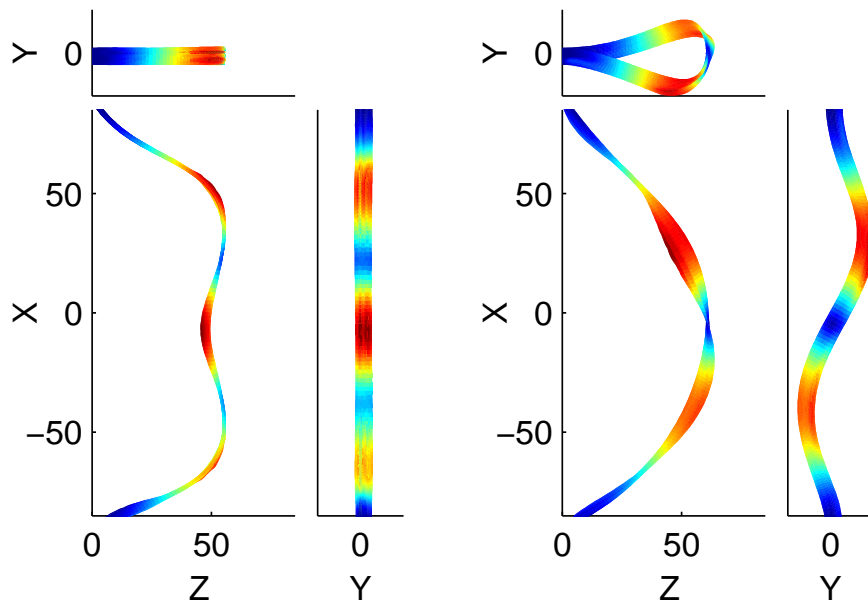
Appendix G

Blade Modes Of Optimized Blades



(a) Blade mode 1 (Edgewise)

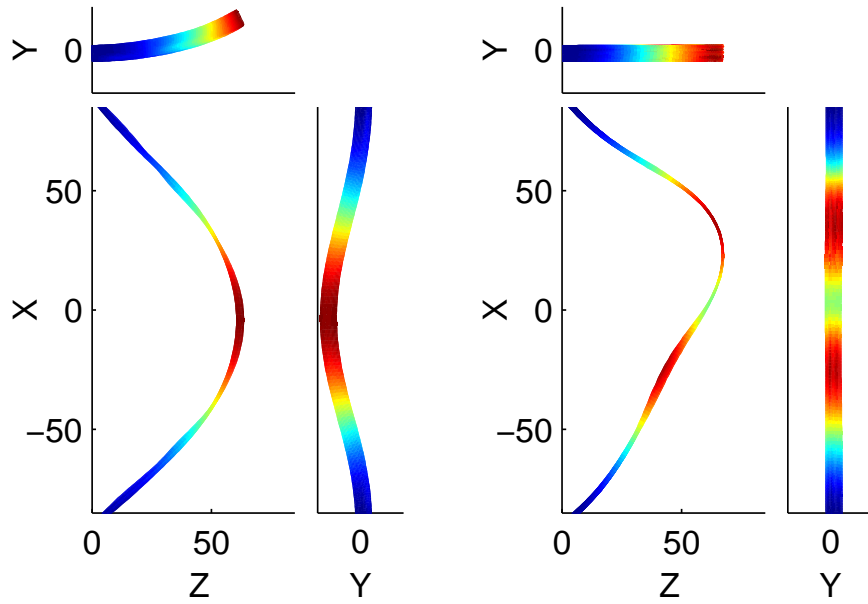
(b) Blade mode 2 (Flapwise)



(c) Blade mode 3 (Flapwise)

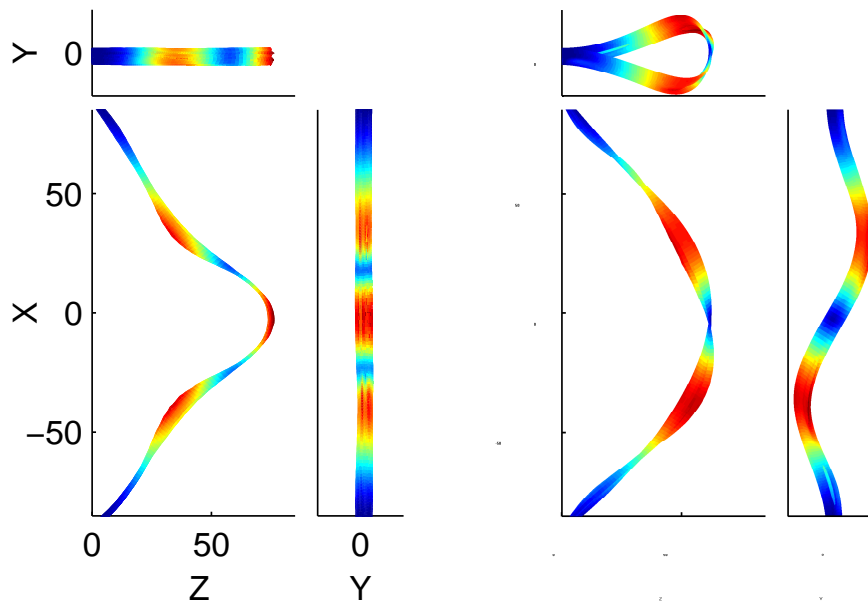
(d) Blade mode 4 (Edgewise)

Figure G.1: Blade modes with profile NACA 0015-35 out of CFRP



(a) Blade mode 1 (Edgewise)

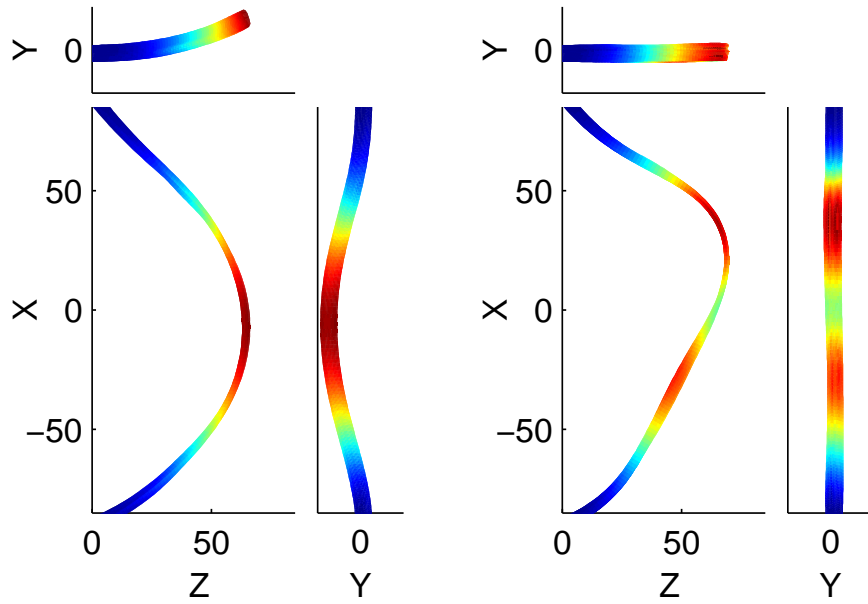
(b) Blade mode 2 (Flapwise)



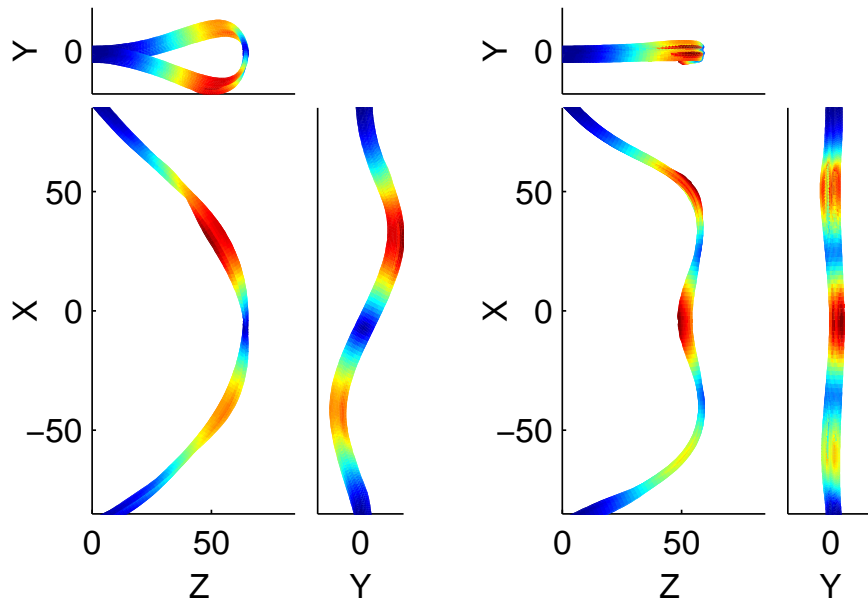
(c) Blade mode 3 (Flapwise)

(d) Blade mode 4 (Edgewise)

Figure G.2: Blade modes with profile NACA 0015-40 out of CFRP



(a) Blade mode 1 (Edgewise) (b) Blade mode 2 (Flapwise)



(c) Blade mode 3 (Flapwise) (d) Blade mode 4 (Edgewise)

Figure G.3: Blade modes with profile NACA 0030 out of GFRP

References

- [1] Brian Adams. *DAKOTA 5.0 and JAGUAR 2.0 - Capability Overview*. Sandia National Laboratories, 1.0 edition, January 2010.
- [2] J. W. Anderson. Mc donnell 40 kw giromill wind system. Technical report, Mc Donnell Aircraft Company, August 1979.
- [3] Inc ANSYS. Mechanical products. Webpae, March 2014. URL <http://www.ansys.com/staticassets/ANSYS/staticassets/resourcelibrary/brochure/ansys-mechanical-suite-brochure-14.0.pdf>.
- [4] Kirby A. Baker. *Lecture Notes of The Mathematics of Computer Graphics (M149)*. University of California, Los Angeles, December 2002. http://www.math.ucla.edu/~baker/149.1.02w/handouts/dd_splines.pdf.
- [5] Habtamu Ber. Double multiple stream tube model and numerical analysis of vertical axis wind turbine. *Energy and Power Engineering*, 3:262–270, 2011. doi: 10.4236.
- [6] Vishal Kevat Bhavesh Patel. Performance prediction of a straight bladed darrieus wind turbine by single streamtube model. *International Journal of Advanced Engineering Technology*, IV(II):86–89, April-June 2013.
- [7] Harry B. Bingham. *Lecture Notes of Computational Fluid Dynamics (41319)*. DTU Campus Bookstore, 2012.
- [8] F.J. Blom. A monolithical fluid-structure interaction algorithm applied to the piston problem. *Computer Methods in Applied Mechanics and Engineering*, 167:367–391, 1998.
- [9] R. De. Breuker. *Lecture Notes of Wind Turbine Aeroelasticity*. TU Delft, June 2013.
- [10] P. Le Tallec C. Farhat, M. Lesoinne. Load and motion transfer algorithms for fluid/structure interaction problems with non-matching discrete interfaces: Momentum and energy conservation, optimal discretization and application to aeroelasticity. *Computer Methods in Applied Mechanics and Engineering*, 157:95–114, 1998.

- [11] Robert Clark. *A Modern Course in Aeroelasticity*. Kluwer Academic Publisher, 2nd edition, 2005.
- [12] Thomas D. Ashwill D. Todd Griffith. The sandia 100-meter all-glass baseline wind turbine blade: Snl100-00. Technical Report SAND2011-3779, Sandia National Laboratories, June 2011.
- [13] G.J.M. Darrieus. Turbine having its rotating shaft transverse to the flow of the current, 1931.
- [14] Granta Design. Ces edupack. Software, 2013.
- [15] K.R. Dixon. *The Near Wake Structure of a Vertical Axis Wind Turbine*. PhD thesis, Technical University of Delft, April 2008.
- [16] C. Farhat. Partitioned procedures for the transient solution of coupled aeroelastic problem. *Computer Methods in Applied Mechanics and Engineering*, 124:79–112, 1995.
- [17] Carlos S. Ferreira. *The near wake of the VAWT*. PhD thesis, Technical University of Delft, 2009.
- [18] Taeseong Kim Anders Yde Frederik Zahle, Robert Bitsche. The dtu 10-mw reference wind turbine. Technical report, DTU Wind Energy, 2012.
- [19] Paul Gipe. Photos of vertical axis wind turbines by paul gipe. Website (31st January 2014), 2014. URL <http://www.wind-works.org/cms/index.php?id=219>.
- [20] Martin O.L. Hansen. *Aerodynamics of Wind Turbines*. Earthscan, second edition, 2008.
- [21] Martin O.L. Hansen. *Lecture Notes of Introduction to Wind Turbine Technology (46300)*. Denmark Technical University, September 2012.
- [22] Luca Vita Helge A. Madsen, Uwe S. Paulsen. Implementation of the actuator cylinder flow model in the hawc2 code for aeroelastic simulations on vertical axis wind turbines. In *51st AIAA Aerospace Sciences Meeting including the New Horizons Forum and Aerospace Exposition*, number 51st, Grapevine (Dallas/Ft. Worth Region), Texas, January 2013. AIAA.
- [23] Uwe S. Paulsen Helge A. Madsen. 1st deepwind 5 mw baseline design. *Energy Procedia*, 24:27–25, 2012.
- [24] Uwe S. Paulsen Helge A. Madsen. Design optimization of a 5 mw floating offshore vertical-axis wind turbine. *Energy Procedia*, 35:22–32, 2013.
- [25] Thomas D. Ashwill Herbert J. Sutherland, Dale E. Berg. A retrospective of vawt technology. Technical report, Sandia National Laboratories, 2012.
- [26] J. L. Hess and A. M. O. Smith. Calculation of potential flow about arbitrary bodies. *Progress in Aerospace Sciences*, 8(1–138), 1967.
- [27] R.C. Hibbeler. *Mechanics of Materials*. Pearson, 2011.

- [28] S. J. Hulshoff. *Lecture Notes of Aeroelasticity (AE4930)*. TU Delft, September 2013.
- [29] F. Delclaux I. Paraschivoiu. Aerodynamic analysis of the darrieus rotor including secondary effects. *Journal of Energy*, 7:416–422, 1983.
- [30] W. Musial J. Jonkman, S. Butterfield. Definition of a 5-mw reference wind turbine for offshore system development. Technical Report NREL/TP-500-38060, NREL, February 2009.
- [31] A.L. Rogers J.F. Manwell, J.G. McGowan. *Wind Energy Explained - Theory, Design and Application*. John Wiley and Sons Ltd., second edition, 2009.
- [32] Jr. John D. Anderson. *Fundamentals of Aerodynamics*. Mcgraw-Hill Publ.Comp., 5th edition, 2011.
- [33] D. Zafirakis John K. Kaldellis. The wind energy (r)evolution: A short review of a long history. *Renewable Energy*, 36:1887–1901, 2011.
- [34] I. C. Jong. Guiding rules in the conjugate beam method. *Int. J. Engng*, 26:1422–1427, 2010.
- [35] Jason M. Jonkman. *FAST User's Guide*. National Renewable Energy Laboratory, nrel/el-500-38230 edition, August 2005.
- [36] Christos Kassapoglou. *Design and Analysis of Composite Structures: With Applications to Aerospace*. John Wiley & Sons Ltd, 2nd edition, May 2013. ISBN: 9781118401606.
- [37] Joseph Katz. *Low-Speed Aerodynamics*. Cambridge University, 2001.
- [38] Soren Kroh. *The Economics of Wind Energy - A report by the European Wind Energy Association*, 2009.
- [39] Mathijs Langelaar. *Lecture Notes of Engineering Optimization (WB1440)*. TU Delft, May 2013.
- [40] Torben J. Larsen. Hawc2 description. Website (29th August 2013), 2011. URL <http://www.hawc2.dk/>.
- [41] T.D. Ashwill, D.W. Lobitz. Aeroelastic effects in the structural dynamic analysis of vawt. Technical report, Sandia National Laboratories, April 1986.
- [42] J.E. Mottershead M. Friswell. *Finite Element Model Updating in Structural Dynamics*. Springer, 1995.
- [43] Helge A. Madsen. Analysis of vawt aerodynamics and design using the actuator cylinder flow model. In *TORQUE 2012*, 2012.
- [44] Helge A. Madsen. Implementation of the actuator cylinder flow model in the hawc2 code for aeroelastic simulations on vertical axis wind turbines. In T.J. Larsen, editor, *51st AIAA Aerospace Sciences Meeting including the New Horizons Forum and Aerospace Exposition*, number AIAA 2013-0913, Grapevine, Texas, USA, January 2013. AIAA.

- [45] D. Sørensen Martin O.L. Hansen. Cfd model for vertical axis wind turbine. In *Wind Energy for the New Millennium-Proceedings of the European Wind Energy Conference*, Copenhagen, Denmark, 2001.
- [46] Josh Paquette Matt Barone. Vertical-axis wind turbine revisited: A sandia perspective. In *Wind Turbine Blade Workshop*. Sandia National Laboratories, June 2012.
- [47] T.H.G. Megson. *Aircraft Structures for Engineering Students*. Elsevier, 2007.
- [48] L. Meirovitch. *Computational Methods in Structural Dynamics*. Mechanics: Dynamical Systems, 1980.
- [49] C. Farhat N. Maman. Matching fluid and structure meshed for aeroelastic computations: A parallel approach. *Computers and Structures*, 54(5):779–785, 1995.
- [50] Hans Bruun Nielsen. *DACE - A MATLAB Kriging Toolbox*. Technical University of Denmark, 2.0 edition, August 2002.
- [51] Niki Nixon. Timeline: The history of wind power. Website (26th August 2013), October 2008. URL <http://www.theguardian.com/environment/2008/oct/17/wind-power-renewable-energy>.
- [52] U.S. Department of Energy. Total electricity net consumption (billion kilowatthours). Website (28th May 2014), 2011. URL <http://www.eia.gov/cfapps/ipdbproject/IEDIndex3.cfm?tid=2&pid=2&aid=2>.
- [53] Brian C. Owens. Aeroelastic modeling of large offshore vertical-axis wind turbines: Development of the offshore wind energy simulation toolkit. In D. Todd Griffith, editor, *54th AIAA/ASME/ASCE/AHS/ASC Structures, Structural Dynamics, and Materials Conference*, number AIAA 2013-1552, Boston, Massachusetts, USA, April 2013. AIAA.
- [54] Panos Y. Papalambros. *Principles of Optimal Design Modeling and Computation*. Cambridge University Press, 2000.
- [55] Ion Paraschivoiu. Double-multiple stream tube model for studying vertical-axis wind turbines. *Journal of Propulsion and Power*, 4, 1988.
- [56] Niels Leergaard Pedersen. *Lecture Notes of Computational Multibody Dynamics (41515)*. Denmark Technical University, September 2013.
- [57] Serge Piperno. Explicit/implicit fluid structure staggered procedures with a structural predictor and fluid subcycling for 2d inviscid aeroelastic simulation. *International Journal For Numerical Methods in Fluids*, 25:1207–1226, 1997.
- [58] Elijah Polak. *Optimization : Algorithms and Consistent Approximations*. Springer, 1997.
- [59] Andrey Popov. *Genetic Algorithms For Optimization*. TU-Sofia, 1.0 edition, 2005.
- [60] A. Poursartip and P. W. R. Beaumont. The fatigue damage mechanics of a carbon fibre composite laminate: li life prediction. *Composites Science and Technology*, 25: 289–299, 1986.

- [61] Björn Roscher. Current aerodynamic models for vawt and numerical comparison between hawc2 and u2div. Special Project - EWEM Rotor Design, January 2014.
- [62] Mark Schelbergen. Structural optimization of multi-megawatt, offshore vertical axis wind turbine rotors. Master's thesis, Technical University, 2013.
- [63] James H. Strickland. The darrieus turbine: A performance prediction model using multiple steam tube model. Technical report, Sandia National Laboratories, 1975.
- [64] R. J. Templin. Aerodynamic performance theory for the nrc vertical-axis wind turbine. Technical Report LTR-LA-190,, NRC Laboratories, June 1974.
- [65] Giuseppe Tescione. Vertical axis wind turbine. Lecture Notes 'AE4W12 Rotor Aerodynamics (2012-2013 Q3)', March 2013.
- [66] William Thomson. *Theory of Vibration with Applications*. Taylor & Francis, 1996.
- [67] Robert W. Thresher. *Wind Turbine Technology*, volume 2nd Edition. ASME Press, 2009.
- [68] Nick Jenkins Tony Burton, David Sharpe. *Wind Energy - Handbook*. John Wiley and Sons Ltd., first edition, 2001.
- [69] A. van Zuijlen. *An introduction to numerical coupled simulation*. TU Delft, March 2013.
- [70] A. van Zuijlen. *Lecture Notes of Fluid-structure interaction (WB1417)*. TU Delft, May 2013.
- [71] Vestas. The v164-8.0 mw iec s. Website (10th Januray 2014), January 2014. URL http://www.vestas.com/en/products_and_services/turbines/v164-8_0-mw#!about.
- [72] Jan R. Wright. *Introduction to Aircraft Aeroelasticity and Loads*. John Wiley & Sons Ltd, 2007.
- [73] M.A. Scott Y. Bazilves, M.C. Hsu. Isogeometric fluidstructure interaction analysis with emphasis on non-matching discretizations, and with application to wind turbines. *Computer Methods in Applied Mechanics and Engineering*, 249:28–41, 2012.

